Doctoral Dissertations

Graduate School

Spring 2004

Novel sensors for neural glucose concentration based on enzyme fluorescent thin films fabricated on nanoparticle carriers using electrostatic layer -by -layer assembly

Patrick Scott Grant

Follow this and additional works at: https://digitalcommons.latech.edu/dissertations

NOVEL SENSORS FOR NEURAL GLUCOSE CONCENTRATION BASED ON

ENZYME FLUORESCENT THIN FILMS FABRICATED ON NANOPARTICLE

CARRIERS USING ELECTROSTATIC LAYER-BY-LAYER ASSEMBLY

by

Patrick Scott Grant, B.S. Biomedical Engineering

A Dissertation Presented in Partial Fulfillment
of the Requirements for the Degree
Doctor of Philosophy

COLLEGE OF ENGINEERING AND SCIENCE
LOUISIANA TECH UNIVERSITY

May 2004

UMI Number: 3126524

INFORMATION TO USERS

The quality of this reproduction is dependent upon the quality of the copy submitted. Broken or indistinct print, colored or poor quality illustrations and photographs, print bleed-through, substandard margins, and improper alignment can adversely affect reproduction.

In the unlikely event that the author did not send a complete manuscript and there are missing pages, these will be noted. Also, if unauthorized copyright material had to be removed, a note will indicate the deletion.

UMI®

LOUISIANA TECH UNIVERSITY

THE GRADUATE SCHOOL
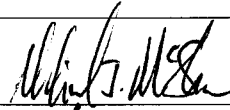
May 13, 2004
                                                                    Date

We hereby recommend that the dissertation prepared under our supervision

by Patrick Scott Grant

entitled NOVEL SENSORS FOR NEURAL GLUCOSE CONCENTRATION BASED ON

ENZYME FLUORESCENT THIN FILMS FABRICATED ON NANOPARTICLE CARRIERS

USING ELECTROSTATIC LAYER-BY-LAYER ASSEMBLY

be accepted in partial fulfillment of the requirements for the Degree of

Doctor of Philosophy in Biomedical Engineering

_____
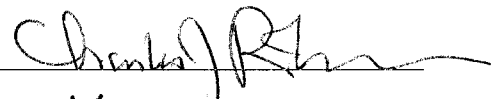   Supervisor of Dissertation Research

_____
                    Head of Department
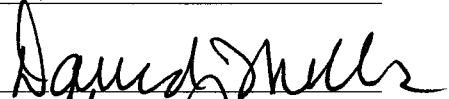
_____
                    Department

Recommendation concurred in:

_____

_____
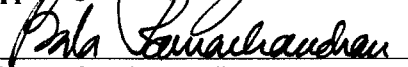
_____   Advisory Committee

_____
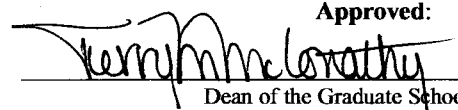
Approved:
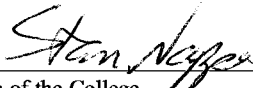
_____
Director of Graduate Studies

_____
Dean of the College

Approved:

_____
          Dean of the Graduate School

ABSTRACT

Currently, there is no means by which rapidly fluctuating glucose and lactate levels can be monitored simultaneously. This dissertation demonstrates that by combining the broad-band versatility of fluorescence spectroscopy with nanoassembly methods, it is possible to construct micro- and nanoscale sensors with precise composition and short diffusion length constant. The work is significant because of its potential as a platform for discovery of basic normal physiological processes that have previously been hidden from researchers' views, more detailed studies of responses to drugs or other stimuli, and even clinical monitoring. The main goal of this work was to develop novel methods that enable the simultaneous study of glucose and lactate transients in the brain extracellular fluid. It is shown that on-line monitoring of glucose concentration can be accomplished using optical probes with nanoassembled analyte specific enzymes combined with fluorescent indicators. A model for fabrication was developed to predict the fluorescence spectrum for a given film architecture. A model for the coupled reaction-diffusion was developed to predict the oxygen concentration in the sensing region of the films as a function of glucose concentration. A model was developed to predict the resulting fluorescence spectrum for the infusion of nanoparticles of a given film architecture. Oxygen sensors were fabricated on quartz slides, optical fibers and nanoparticles. A protocol *in vitro* and *in vivo* sensor delivery was developed

and the delivery are nanoparticle sensors to the dentate gyrus of the hippocampus was confirmed by real-time fluorescence monitoring of the infusion and fluorescence confocal imaging of sectioned rat brain tissue. The accuracy of the fiber probes was shown to be 0.5% for 0 to 100% oxygen. The fiber probes were further developed in to a glucose probe with the addition of GOx films and a coating of 100 μm PDMS coating, which served as a transport barrier to oxygen. The accuracy of the glucose probe was approximately 21% for 0 to 60 mg/dL glucose.

APPROVAL FOR SCHOLARLY DISSEMINATION

The author grants to the Prescott Memorial Library of Louisiana Tech University the right to reproduce, by appropriate methods, upon request, any or all portions of this Dissertation. It is understood that "proper request" consists of the agreement, on the part of the requesting party, that said reproduction is for his personal use and that subsequent reproduction will not occur without written approval of the author of this Dissertation. Further, any portions of the Dissertation used in books, papers, and other works must be appropriately referenced to this Dissertation.

Finally, the author of this Dissertation reserves the right to publish freely, in the literature, at any time, any or all portions of this Dissertation.

Author _____

Date _____

DEDICATION

I would like to thank my father, mother, brothers, and grandmother for their comfort, support, guidance and wisdom during my academic career. I dedicate this work to my grandparents, who are no longer with us.

vi

TABLE OF CONTENTS

TABLE OF FIGURES

CHAPTER 1

INTRODUCTION

Glucose and lactate are essential metabolic substrates for neural cells. Recent studies support the compartmentalization of glucose into metabolically distinct regions of the brain, such as the extracellular fluid and the astrocyte intracellular space. These studies suggest that the previous school of thought which held that glucose levels are relatively constant throughout the brain extracellular fluid (ECF) is incorrect. In addition to steady-state glucose differentials, transient local changes in both glucose and lactate are caused by neuronal activity. Because these events occur rapidly, steady-state assumptions do not hold, and information about short-duration fluctuations is required. Unfortunately, however, there is little knowledge about short-term changes in glucose and lactate levels in the brain ECF, and there is certainly a shortage of information regarding these variations in different parts of the brain.

Currently, there is no means by which rapidly fluctuating glucose and lactate levels can be monitored simultaneously. This dissertation demonstrates that by combining the broad-band versatility of fluorescence spectroscopy with nanoassembly methods, it is possible to construct micro- and nanoscale sensors with precise

1

composition and short diffusion length constant. The work is significant because of its potential as a platform for discovery of basic normal physiological processes that have previously been hidden from researchers' views, more detailed studies of responses to drugs or other stimuli, and even clinical monitoring. The main goal of this work is to develop novel methods that enable the simultaneous study of glucose and lactate transients in the brain extracellular fluid. Figure 1 is a conceptual illustration of the sensor architecture and desired optical response. As part of this work, it will be shown that on-line monitoring of neurochemical dynamics can be accomplished using optical probes with nanoassembled analyte specific enzymes combined with fluorescent indicators.
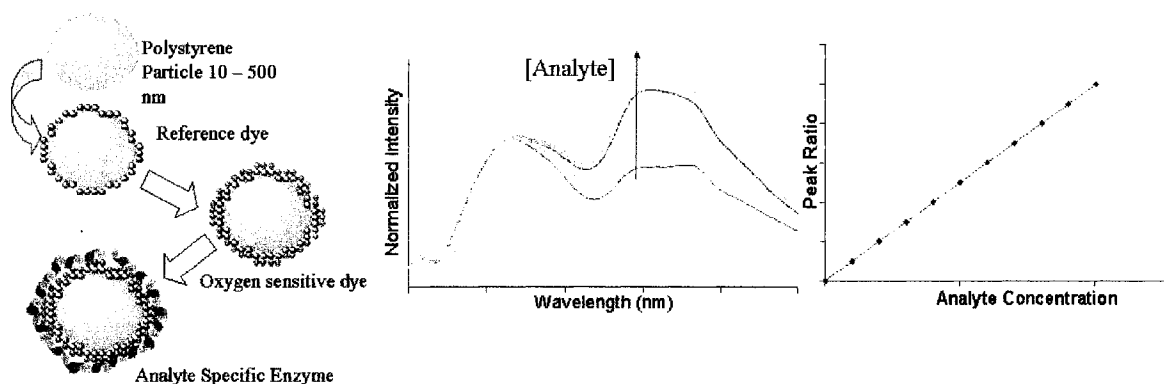
Figure 1. Illustration of sensor architecture and desired optical response.

While fluorescence spectroscopy with molecular probes is an attractive method for monitoring biochemicals due to high sensitivity and specificity, the need to introduce liquid indicators makes it difficult to control and stabilize the location of fluorescent molecules. Furthermore, many of the indicators are cytotoxic and therefore may only be used in acute *in vitro* experiments. Fiber-optic chemical sensors, in which assay

chemistry is immobilized at the end of the fiber and protected by various polymer matrices, have been developed to address the issue of indicator location and cytotoxicity. Fiber-optic sensors have been developed for many analytes such as oxygen,[1] carbon dioxide,[2] pH,[3] glucose,[4] and NADH,[5] but these sensors still require an invasive measurement. Decoupling the assay from fibers through the use of micro/nanoscale carriers, fluorescence-based sensors has been proposed to overcome these problems and enable chronic *in vivo* or *in vitro* sensor deployment. Previous work in this area has involved assays trapped in a hydrogel matrix[6-11] or encapsulated within microdialysis membranes.[12]

A promising technique for fabrication of fluorescent sensors that might provide advantages over current systems is the process of thin film deposition known as electrostatic Layer-by-Layer (LbL) self-assembly. Ultrathin polyelectrolyte films prepared using this technique were first described in 1991.[13] The assembly process is simple and allows precise formation of films with total thickness of 5 to 500 nm, composed of many layers containing alternately charged molecules, on any charged substrate. The thickness of individual layers is on the order of 1 nm.[14] It was also shown that these polyelectrolyte multilayers might be applied to highly curved substrates, such as micro- and nanoparticles.[15] Thus, the technique allows one to select from a wide variety of materials, both substrates and adsorbate molecules, to produce structures with the desired properties for different applications.

In particular, LbL may be an extremely powerful approach to fabricating fluorescent sensors for biomedical application. The employment of LbL-assembled films for fluorescent sensing has been heretofore limited to two examples, and has been

considered only for planar substrates. Very recent work has demonstrated pH-sensitive films on planar templates using direct assembly of dyes.[16] A ferric ion sensor based on acridine-containing polymer assembled in multilayer films has also been proposed, but no experimental validation of function in multilayer assemblies has been given.[17] In attempts to extend the applicability, versatility, stability, and sensitivity of fluorescence sensing ultrathin films, our work has emphasized LbL assembly of internally-referenced sensors containing indicators, reference fluorophores, and active biomolecules such as enzymes. As part of this effort, assembly of sensing films and enzymes on polystyrene particles has been introduced as a general concept for fabrication of fluorescent sensors tailored for specific biochemical measurements[18,19]. To develop stable calibrated sensors, a detailed investigation on fabrication properties is necessary.

Electrostatic Layer-by-Layer self-assembly (LbL) is an attractive method for depositing films composed of charged molecules on a wide variety of charged substrates. This dissertation describes progress toward development of LbL as a platform for fabrication of fluorescent sensors for glucose and lactate sensing based on nanocomposite multilayer ultrathin films. To accomplish this goal, several methods for stable assembly of sensing films were considered, including direct electrostatic assembly of charged fluorescent indicators, fluorophore: and polyion premixing, conjugation of indicator to polyelectrolyte and post-loading of fluorophores into polyion films. Additional layers of fluorescein 5(6)-isothiocyanate (FITC) or Alexa Fluor 488® (488) conjugated to PAH were deposited on the same templates to serve as an internal reference and allow ratiometric measurements. Films were deposited onto glass slides, fiber-optics and polymer microspheres. The fluorescence properties of films on the different substrates

were then compared to determine whether the deposition process is versatile and generally portable between templates. This versatile property is important because the use of LbL as a platform for fabrication of fluorescent chemical sensors allows new sensing schemes to be developed and tested using macro scale templates, which are often cheaper and generally easier to investigate with analytical instruments. This work provides a basis for developing sensors for numerous biomedical applications, including fiber-optic probes designed for research and clinical measurements, sensing films on tissue culture substrates, and implantable micro/nanoparticle based sensors for *in vitro* or *in vivo* monitoring.

The versatility of this sensor development is two-dimensional. First, there are many methods for depositing fluorescent indicators on macro templates (sol-gel, silicone, thiol conjugation), but these suffer from poor repeatability, complex chemistry, and most often a single-layer limatation. In contrast, the LbL assembly method can be applied with extreme precision to virtually any substrate, most importantly nano-/micro-colloids. A key point is that any assembly process that can be developed and tested on macrotemplates can be directly ported to micro/nanotemplates. The second area of flexibility afforded by the fabrication method is in the choice of fluorophores employed.

In this work, we present a study of practical approaches to fluorescent film deposition to "buildup" thin films with sensing function on various templates, then assess the physical stability, intensity, and sensitivity of the resulting films. Specifically, we demonstrate the precise construction of an internally referenced (two-dye) oxygen sensor based on quenching of ruthenium that can be coupled to the enzyme, glucose oxidase, for the sensing of glucose. The key to this technology is the precise deposition of

nanocomposite ultrathin films with potentially complex composition, structure, and chemical function, which can be engineered to define sensing devices. Figure 1 is an illustration of the sensor architecture and desired optical response.

The adsorption methods assessed include direct assembly,[20,21] premixing of dyes with polyions,[22] covalent linkage of dyes to polyions,[23] and loading of dye into polyion LbL films. Figure 2 is a cartoon depicting the templates used for LbL assembly: a) planar templates, b) optical fibers, and c) micro/nanoparticles.

(a)   (b)   (c)
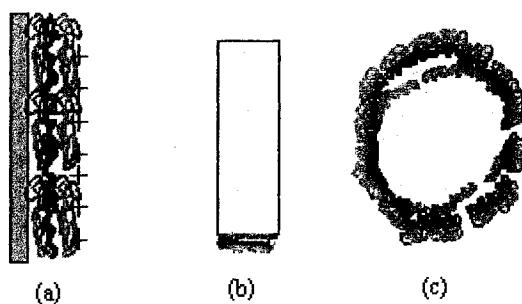
Figure 2. Templates used for LbL assembly of fluorescent sensing films: a) glass slides, b) optical fibers, and c) latex microspheres.

Depending on the template, various biomedical applications are envisioned, including planar sensing substrates for tissue cultures, fiber-optics probe for acute clinical measurements, and microspheres for implantable/injectable sensors. A host of non-biomedical possibilities also exist, such as environmental monitoring, process control, and defuse applications.

Five specific aims were developed to guide the theoretical and experimental exploration into this research: first, to determine the effect of nanoassembly of glucose oxidase, lactate oxidase, and oxygen sensitive fluorescent dyes on chemical sensitivity

and optical response; second, to determine the effect of sensor size, coating thickness, and composition on sensor response; third, to apply biocompatible coatings and determine their influence on sensor characteristics; fourth, to identify a protocol for introducing sensors and monitoring fibers into brain with minimal trauma, and lastly, to validate in vivo sensor operation with microdialysis measurements.

This dissertation describes the outcome of work completed in pursuit of these aims over the past three years. Chapter Two is a thorough review of the relevant literature on neurochemistry, glucose sensing, and nanofabrication using the LbL assembly technique. Chapter Three discusses on the basic architecture of the sensor, the optical properties of the sensors and tissue, the chemical properties of the sensor components, and modeling and prediction of the sensor fabrication, delivery and function. Chapter Four is an overview of the materials and methods used in addressing the specific aims. Chapter Five presents of the experimental results with a detailed discussion regarding how the objectives set forth in the advent of the work were achieved. Chapter Six gives the conclusions drawn from this work.

CHAPTER 2

LITERATURE REVIEW

The following chapter provides the background information relevant to the development of the glucose sensors outlined in the objectives of this project. Section 1 and Section 2 is an overview of neural anatomy and physiology. Section 2 discusses the fundamentals of energy metabolism in the brain. Section 3 provides the background of the current methods for making neurochemical measurements, as well as sensor technology in development. Section 4 reviews optical sensing technologies being developed that could possibly be adapted for neurochemical measurements. Section 5 is a thourough discussion of layer-by-layer nanoassembly process. Last, Section 6 is a brief review of the materials suitable for a brain phantom.

8

2.1 Neural Anatomy and Physiology

2.11 Choroid Plexus

The choroid plexus lining the third ventricle secretes cerebrospinal fluid (CSF)

that fills the ventricles in the brain. The cells of the choroid plexus are specialized for

secretory processes and develop into a series of folded ependymal cells found on the

luminal surface of the ventricle (Figure 3). The folds are called villi and form a series of

dome-like structures each with microvilli (Figure 4). One dome equals one choroidal

epithelial cell. Grooves between domes are points of contact between individual

choroidal cells. Each is attached to its neighboring cell by tight junctions, which forms

the blood-brain barrier. These junctions seal off the extracellular space from the

ventricular space.[24] Solutes reach neural tissue by passing through endothelial cells.

Water, gases, lipid-soluble and small molecules can diffuse across the endothelial cells.

Other substances must be carried across by transport systems. This exchange is highly

selective.[25]
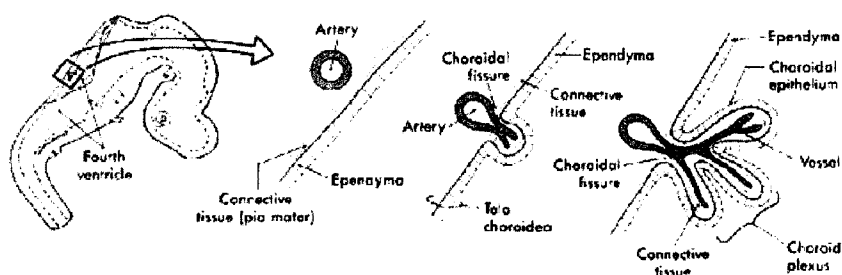
Figure 3. Development of choroid plexus (Haines, 1997).

Choroidal epithelial cells contain one nucleus, numerous mitochondria, rough

endoplasmic reticulum and small Golgi apparatus. They are specialized to control the

flow of ions and metabolites into CSF. Choroidal epithelial cells secrete CSF by selective transport of materials from connective tissue extracellular space. NaCl is actively transported into ventricles and water follows the concentration gradient established. Other materials are transported in pinocytotic vesicles from the basal to the apical surface of the epithelium and exocytosed into the CSF. Compared with blood plasma, CSF has high concentrations of chloride, magnesium, and sodium and lower concentrations of potassium, calcium, glucose, and protein.[24]

2.12 Cerebrospinal Fluid System

The entire cavity that houses the brain and spinal cord has a volume of about 1700 ml. About 150 ml of this space is cerebrospinal fluid. CSF accounts for the fluid found in the ventricles of the brain, cisterns around the brain, and the subarachnoid space around both brain and spinal cord. All of these connect to one another; and pressure is regulated at a constant level. Secretion of CSF by the choroid plexus depends mostly on active transport of sodium ions through epithelial cells that line outside of plexus. Sodium ions pull in large amounts of chloride ions because the negative charge of the chloride ion is attracted to the positive sodium ion. Both of these ions increase amounts of osmotically active substances in cerebrospinal fluid, causing osmosis of water through the membrane, providing fluid for the secretion. Small amounts of glucose are transported into the cerebrospinal fluid and move potassium and bicarbonate ions out of CSF into capillaries.
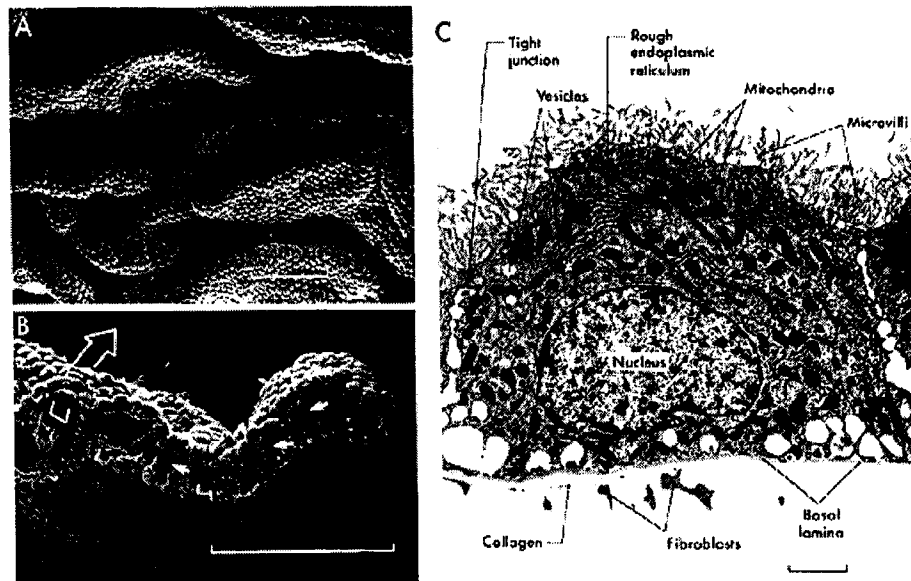
Figure 4. Elements of the choroid plexus (Haines, 1997).

The CSF has several notable characteristics: (1) The osmotic pressure is equal to that of plasma; (2) the concentration of sodium is about equal to that of plasma; (3) the concentration of chloride is about 15% greater than plasma; (4) the concentration of potassium is about 40% less than in plasma; and (5) glucose is about 30% lower than plasma.[25]

2.13 Glial Cells

As with most tissues in the body, blood capillary bed density is greatest where metabolic needs are greatest. The neuronal cell bodies are found in the gray matter of the brain. Here the metabolic rate is about four times that found in the white matter. The capillary bed blood flow rate is correspondingly about four times greater in gray matter than in white matter. The capillaries of the brain are much less leaky than capillaries found in any other tissue in the body. Most importantly, brain capillaries are supported

on all sides by "glial feet." These "feet" are small projections from surrounding glia that wrap around all surfaces of the capillaries. They provide physical support and also prevent over-stretching due to high blood pressure.[25] Glial cells do not transmit action potentials and they are not specialized to receive and transmit electrical signals. Instead, they provide structural support for neurons and maintain the local physical and chemical environment for proper neuronal function. Glial cells account for the majority of cells in the nervous system, and normal brain function depends critically on them. Glia in the central nervous system (CNS) are known as "astrocytes" and "oligodendrocytes," both derived from mesoderm. The analogous cell types in the peripheral nervous system (PNS) are satellite cells, Schwann cells, and macrophages.[24]

2.2 Neural Energy Metabolism

For many years, neuroanatomists have suggested that astrocytes play a nutritional role in the central nervous system (CNS)[26]. Glucose crossing from the bloodstream into the CNS is believed to enter astrocytes before entering the extracellular fluid (ECF). Functional coupling between astrocytes and neurons is hypothesized, though the contribution of astrocytic lactate to the downstream neuron is still unclear.[26] What is clear, however, is that astrocytic modulation of glucose delivery to neurons would require glucose compartmentation between metabolically distinct regions in the brain (neuronal and astrocytic intracellular space, ECF). Recent studies support this compartmentalization, despite the previous hypothesis that glucose levels are relatively constant throughout the brain ECF.

In addition to steady-state glucose differentials, it is likely that transient local changes in both glucose and lactate are caused by neuronal activity.[27] Because these events occur rapidly, steady-state assumptions do not hold and information about short-duration fluctuations is required. Unfortunately, however, there is little knowledge about short-term changes in glucose and lactate levels in the brain ECF. There is certainly a shortage of information regarding these variations in different parts of the brain. Some recent work has outlined the need to monitor transient events. Hu and Wilson, using a fast glucose electrode with a rapid response time, showed significant fluctuations in hippocampal glucose due to application of KCl and direct electrical stimulation[28]. Boutelle, Fellows, and Cook monitored glucose, lactate, and glutamate following mild behavioral stimulation (tail pinch) and observed transient changes in striatal glucose and lactate[29].

2.21 Astrocytes

Astrocytes exist throughout the CNS. They are highly branched and their processes end in expansions called end feet. Free surfaces, neuronal dendrites, and cell bodies as well as some axonal surfaces are covered with opposed astrocyte end feet. The astrocyte end feet join together to completely line the interfaces between CNS and other tissues (Figure 3). Blood vessels in the CNS are separated from neuronal tissue by a layer of end feet. Astrocytes in the gray matter of the brain are called protoplasmic astrocytes, which differ in shape from astrocytes in white matter, called fibrous astrocytes. White matter astrocytes and gray matter astrocytes differ in regard to their ion channels, neurotransmitter receptors, and uptake systems.
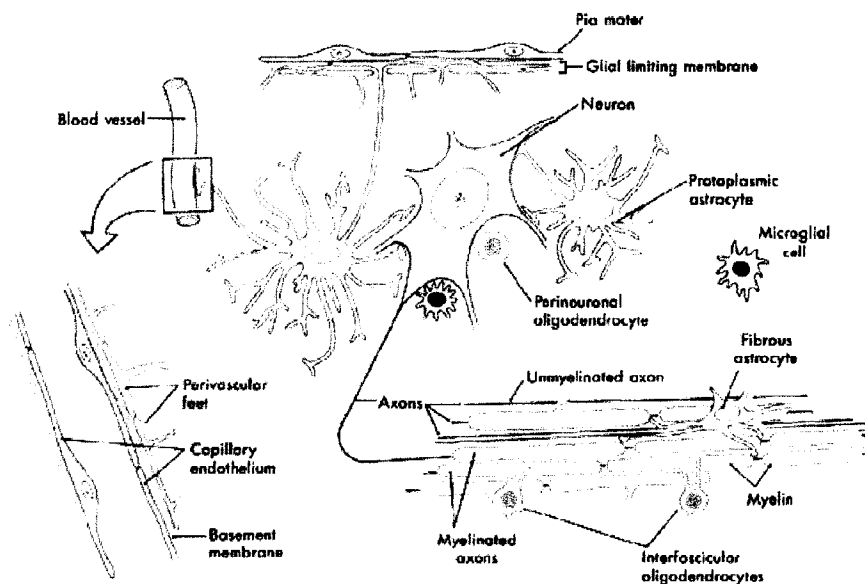
Figure 5. Relationship of astrocytes to neuronal cell bodies, axons, blood vessels and pia mater (Haines, 1997).

During development, astrocytes form the framework for neuronal migration. In the adult, brain astrocytes frame certain clusters of neurons, and they also enclose bundles of unmyelinated axons. Current research indicates that astrocytes secrete growth factors vital to support of some neurons.[24] Due to their location and metabolic versatility, astrocytes serve as fuel processing plants within CNS tissue. Lactate is considered a major astroglial metabolic product.[30] In disease processes, they may secrete cytokines, which regulate the function of immune cells invading CNS tissues. Injury to CNS tissue that causes cell loss stimulates a proliferation of astrocytes, resulting in astrocytic scar. The ionic environment and pH of the extracellular space are buffered by astrocytes. Ion channels found in astrocytes are different from those found in neurons. For example, potassium ions released from neurons during an action potential are removed from extracellular space by astrocytes via plasma membrane ion channels.[24]

Astrocytes are connected to each other by gap junctions and may act electrically as a syncytium. They participate in neurotransmitter metabolism. Their membranes have receptors for some neuroactive substances and uptake systems for others. Uptake systems terminate the postsynaptic effect of some neurotransmitters by removing them from the synaptic cleft. For example, the amino acid neurotransmitter glutamate is taken up by astrocytes and is inactivated within the astrocytes by the enzymatic addition of ammonia to produce glutamine.[24] Results of Forsyth et al. imply compartmentalization of brain glucose, and are consistent with the model describing glucose reaching the neuron by way of astrocytic intracellular space and the extracellular fluid (ECF).[31] Glucose is most likely to initially enter the astrocytic intracellular space, rather than the ECF. The neuron may be described as being "downstream" from the astrocytes and receive metabolic substrates from the blood via the astrocytes.[31]
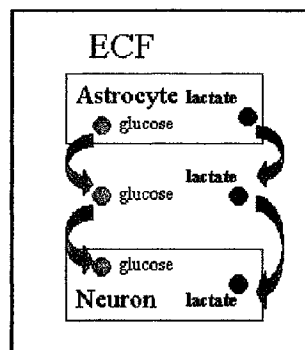
Figure 6. Cartoon describing the pathway a neuron receives glucose via an astrocyte.

Stores of glycogen in the brain are relatively small and confined to the astrocytes. Glucose is transported rapidly across the blood-brain barrier and plasma membranes. It is generally accepted that its metabolism is phosphorylation-limited and not transport-limited. Consequently, intracellular glucose metabolism can remain constant in spite of a

decrease in blood sugar concentration until transport becomes limiting. Increased neural firing, such as occurs during electrical stimulation, causes a reduction in glucose level in the external environment. This result is most likely due to enhanced utilization by the cells. Aerobic spreading depression also decreases extracellular sugar concentration because of increased consumption from elevated ion pumping. However, a drop in brain glucose level must activate homeostatic mechanisms, such as increasing in blood flow and/or increasing transport rates because the reduction is followed by a transient overshoot before returning to its original value. In engineering terms, this mechanism would be described as an underdamped system. Interestingly, the pattern of changes in glucose under these conditions closely follows changes in brain oxygen level. This pattern suggests that increase in blood flow and resulting hyperemia may be responsible for this transient increase in extracellular glucose and decrease in blood glucose. It is possible that in the early stages of reperfusion, lactate that has accumulated during ischemia/hypoxia is metabolized by cells in addition to glucose. Another observation is that in hypoglycemia, when external glucose levels in the brain begin to fall, oxygen levels rise. This observation suggests that cerebral oxygen consumption during hypoglycemia is lower than in normoglycemia, while oxygen supply is simultaneously elevated through an increase in blood flow.[32]

2.22 Blood Glucose Regulation

Normal blood glucose concentration is typically between 80-90 mg/dl in a fasting person before breakfast. Concentration increases to 120-140 mg/dl during the first hour

after a meal and returns to the control level about two hours after last absorption of carbohydrates. The physiological control systems in the normal individual tightly regulate blood glucose levels to remain in the 80-120 mg/dl range. During hypoglycemia, the liver produces glucose to maintain control level concentration; therefore, the liver acts as a glucose buffer system. As glucose levels rise, and the rate of pancreatic insulin secretion rises, two-thirds of glucose absorbed is stored in liver. When glucose levels begin to fall and insulin secretion decreases, the liver releases glucose back into blood. The control mechanisms of the liver limit fluctuations in glucose levels to about one-third of what they would be without control. Glucagon and insulin serve as feedback mechanisms for the body. As blood glucose concentration rises, insulin secretion also rises to bring glucose concentration back to normal. As blood glucose levels fall, glucagon secretion increases to raise glucose levels back to normal.

In severe hypoglycemia, the sympathetic nervous system is stimulated, causing a release of epinephrine from the adrenal glands. This stimulation causes more glucose to be released by the liver. After a period of days, growth hormone and cortisol are secreted due to prolonged hypoglycemia; they cause a decrease in the rate of glucose utilization by most cells by converting to utilization of fats. The importance of glucose regulation is due to the fact that glucose is the only source of metabolic energy easily used by the brain for optimal required energy. Most glucose formed during the inter-digestive period is used for metabolism in the brain. The pancreas must not release too much insulin during this time; otherwise, the short supplies of glucose available would all go to the muscles and other peripheral tissues, leaving the brain with a source of energy. Glucose concentration must not rise too high; this increase will cause cellular dehydration,

excessive loss of glucose in urine, and corresponding depletion of fluids and electrolytes from body. Although, as stated previously, insulin is not needed by brain for glucose metabolism, if insulin levels cause blood glucose to fall to low levels, the metabolism of the CNS is depressed. This state is called *insulin shock* and can result in hallucinations, nervousness, excessive sweat, seizures, and coma. If prolonged shock occurs, there is potential for permanent damage to neuronal cells of the CNS.[25]

2.23 Glucose Uptake by Brain

Insulin has little, if any, effect on use of glucose or uptake by brain tissue. Brain cells are normally permeable to glucose and can process it without the aid of insulin. The ability of a compound to serve as a metabolic source for nervous cells is not limited by the cell's ability to direct the compound into certain metabolic routes, but it is limited by the compound's ability to cross the blood-brain barrier.[30] It is essential that glucose level is always maintained above a critical level and this homeostatic regulation is one of the most important functions of blood glucose control systems. When the blood glucose level falls to 20 to 40 mg/dl, hypoglycemic shock develops, and symptoms include progressive nervous irritability, fainting, seizures, and coma.[25] It has been hypothesized[33] that under normoglycemia, four independent pathways may exist: a high affinity pathway, facilitated diffusion pathway, a specific non-saturable diffusion pathway, and nonspecific passive diffusion pathway. For facilitated diffusion to take place, glucose must bind with a carrier protein and be transported across the membrane. This process requires time, which accounts for the increase in brain glucose level being slower than increases in

blood glucose level during rapid blood glucose infusions. Thus, measurement of blood glucose will overestimate brain glucose level. The period of time following glucose infusions, both blood and brain glucose level decrease and measurement of blood glucose will tend to underestimate glucose concentration in the brain.[34]

In the normal mammalian adult, brain glycogen is found predominantly in astrocytes. Minor amounts are found in neurons, cells of the choroid plexus, epithelial cells, meningeal cells, capillary cells, and pericytes.[35][36] The pathways for glycogen generation in astroglial cells are the same for other cell types and tissues. Glycogen is synthesized from glycogenin via proglycogen. Astroglial cells have a constant steady-state level of glycogen and there appears to be a connection between astroglial glycogen mobilization and neuronal activity.[37] In co-culture experiments, the presence of glycogen in astrocytes improved the survival of neurons.[38] After depletion in extracellular glucose or after a hormonal stimulation, glycogen may be broken down locally in the astrocytes. The results of the breakdown would be the free energy passed on to neighboring cells via the lactic acid generated.[30] Several groups have suggested that lactate resulting from astrocytic glycogenolysis or glycolysis may serve as an additional energy substrate for activated neurons.[31] Thus, two lactic acid molecules are almost as beneficial as fuel material as the glucose from which they derive. Astrocytes appear to be the gluconeogenic cell type of the central nervous system. In a situation of high rates of generation and release of lactic acid for neighboring cells, astrocytes could dispose of the acid by using it up in the gluconeogenic process. This process would serve three roles: buffering, controlling osmolarity of the extracellular fluid, and recycling of the lactate generated by a neighboring cell.[30]

2.24 Hyperglycemia and Hypoglycemia Effects

Two main centers control feeding behavior in animals. Located in the basal hypothalamus, the lateral hypothalamic area (LHA) plays a strong role in stimulation of appetite and food intake and the ventromedial hypothalamic nucleus (VMH) havs an opposite effect. A major endogenous regulatory factor that modulates these two areas is the concentration of glucose. Most CNS neurons are remarkably insensitive to alterations in extracellular concentrations of glucose. Thus the sensitivity of the hypothalamic cells to small glucose changes is in sharp contrast to the general response of CNS cells.

In vivo rat studies by Silver et al. have shown that in hypothalamic areas, 30-40% of neurons, LHA and VMH, have selective sensitivity to increases and decreases in glucose concentration. This behavior indicates that these cells can respond to physiological shifts in sugar concentrations and therefore have the capacity to be an important mechanism in homeostasis. Transport of glucose from extracellular space into neurons is suggested to occur via facilitated diffusion, which does not require sodium. In LHA neurons, a reduction in $[Na^+]$ and rise in $[K^+]$ accompanied hyperglycemia, whereas an opposite event took place during hypoglycemia. Their findings show that, in the LHA, neuronal changes in glucose concentration continuously modify the intracellular concentration of ATP, which means there will be an increase above the basal level in hyperglycemia and a decrease in hypoglycemia. It has been suggested that the reason for this increase is that the LHA neurons, like liver and pancreatic beta cells that contain glucokinase (which amplifies metabolic changes in response to increase or decrease in substrate concentration), contain an analogous sensor mechanism. This mechanism is

supported by recent findings of an expressed glucokinase gene, glucokinase mRNA, and glucokinase activity in medial hypothalamic cells.[39]

Glucose sensitive VMH cells depolarize and increase discharge frequency when glucose level is raised and, correspondingly, hyperpolarize and decrease firing rate when glucose concentration is reduced. Small changes in energy level could alter potassium permeability, which would alter membrane potential. The existence of this glucokinase-like enzyme in VMH cells would allow for a continuous spectrum of changes in ATP concentration. Changes in intercellular calcium concentrations also accompanied, sodium and potassium concentration alterations.[39]

It has been shown that calcium concentration controls the number of sodium channels available for activation. A rise in calcium increases active sodium channels and a decrease reduces the number of active channels. Therefore, not only is the state of polarization of the membrane responsible for neuronal activity but also calcium concentration. These findings have led to a formulation of a mechanism, where alteration of glucose concentration can be translated into an increase or decrease in neuronal activity.[39]

2.25 Summary of Brain Neurochemistry

Brain glucose utilization may become transport limited whenever the rate of transport becomes diminished, for instance during ischemia. Studies support the hypothesis that excitatory neurotransmission is directly coupled to glycolysis. Thus, excitatory stimuli may selectively facilitate the anaerobic rather than glycolytic pathway,

and lactate formation may be the product of such selectivity.[40] It has also been shown that a rapid decrease of local cerebral extracellular glucose concentration occurs on the same time scale of local rapid neurotransmitter release. This observation is interesting because, in contrast to a dramatic decrease in extracellular glucose concentration, there is relatively no decrease in oxygen. This observation suggests, that following a transient increase in neuronal activity, non-oxidative glucose utilization may occur and evidence of this is a much higher increase in the local cerebral glucose metabolic rate relative to the cerebral metabolic rate for oxygen.[28] The neurochemical signs of anaerobic cerebral metabolism are elevated extracellular lactate and diminished extracellular glucose. As stated previously the brain depends almost exclusively on glucose for energy metabolism. It has been assumed that neurons and glia both use glucose as the sole energy substrate and there is evidence of cellular compartmentalization of glucose in astrocytes. Glucose is consumed anaerobically in astrocytes, producing lactate released into extracellular space and then used aerobically by neurons. Increased neuronal activity leads to increased astrocytic glycolysis, which is measured to estimate cerebral metabolic rate of glucose. This compensatory glycolysis is not associated with depletion of glucose from extracellular space. Severe cerebral ischemia causes glucose and lactate metabolism in the cerebral cortex to range from the normal state of coupled glycolytic astrocytic and aerobic neuronal energy production to a state of extreme astrocytic and neuronal anaerobic energy production.[41]

2.3 Neural Glucose and Lactate Sensing

2.31 Microdialysis

Microdialysis sampling has been the main procedure for *in vivo* measurement of ECF neurochemical levels in the animal brain since its development almost thirty years ago.[29,42] The procedure requires the implantation of a probe comprising a dialysis membrane, which is permeable to low molecular weight substances, formed into a loop of tubing through which an artificial fluid is slowly perfused. A concentration gradient drives substances from the ECF in to the perfusate across the membrane. The resulting dialysate is then collected and assayed, usually by HPLC with oxidative electrochemical detection. The molecular weight cutoff of the membrane is chosen to select for smaller analyte molecules to prevent any larger molecules from interfering with both the measurements and normal function. This is particularly important in the brain, where neurotransmitter molecules released by neurons close to the membrane can be removed from the degradative enzymes and reuptake processes.[29]

Typically, these measurements are limited in time resolution to 5-10 minutes because of the removal of substrate from the brain into the dialysate and low recovery.[29] Pyruvate and lactate have been detected with a 5 min sampling interval using absorbance following separation on an HPLC column. The sampling time was achieved by the large extracellular concentration of the analytes rather than a high molar extinction and was limited to 5 min because of the elution time from the column. Enzymes can be incorporated with the microdialysate stream to react with the target analyte, which causes

the formation of a product that can be detected electrochemically or fluorometrically. Using this method, sampling of lactate has been done in real time, while the sampling time for glucose has been reduced to 2 min.[43] More recently, using a enzyme coated electrode, the sampling of glucose has been done in real time,[44] yet the sensitivity of the device was reduced by 3% each hour of use and was usable for only 4-5 days. In addition, microdialysis may actually buffer transient changes.[45] Spreading depression is a propagating transient suppression of electrical activity associated with cellular depolarization that may contribute to neural damage. Microdialysis inhibits spreading depression by buffering the transient increase in extracellular K^+ associated with this phenomenon. Imposing low K^+ levels in the brain cell microenvironment may be particularly deleterious because extracellular K^+ content is the main determinant of the cellular membrane potential and it influences both neuronal interactions and excitability.

Often, the *in vivo* recovery of glucose, defined as the dialysate glucose concentration expressed as a percentage of the brain glucose concentration, never reaches 100%. This ratio depends first on instrumental variables such as perfusion rate, surface area and molecular weight cutoff of the membrane and secondly on the physiological properties of the external environment such as temperature, analyte species, matrix properties of the external media and the microvascular transport and analyte metabolism. Thus, dialysate values cannot be calibrated to brain values by *in vitro* experiments.[40] Stated drawback of microdialysis technique is that the calculation of the recovery *in vivo* is difficult, labor intensive, and often imprecise. Also, sampling can often lead to the depletion of the analytes, because of the removal of the analytes near the probe, which leads to underestimation of the concentrations.

Microdialysis has been coupled online with capillary electrophoresis (CE) and laser-induced fluorescence (LIF) detection, improving the temporal resolution to tens of seconds. The temporal resolution is still ultimately limited by the sampling process or tissue properties *in vivo*.[46] Microfabricated microdialysis devices have been suggested to improve temporal resolution by decreasing sample volume and sampling distance, but are not commercially available and have not been tested *in vivo*.[47] In summary, microdialysis is suitable for integrated monitoring of brain chemistry, it is not able to measure rapid changes.

2.32 Electrochemical Devices

Due to the limitations of microdialysis, other methods for *in vivo* chemical analysis have been explored. Substrate-specific enzyme-electrochemical biosensors have been used for decades as *in vivo* analysis tools.[48] These devices, which typically use glucose oxidase (GOx) as the enzyme, have been developed with extremely fast response times and high selectivity, though endogenous electroactive agents such as uric acid and ascorbic acid can potentially interfere with the signal by oxidizing on the electrodes. The active site for this enzyme is a flavin adenine dinucleotide (FAD), which exist in two forms, oxidized (FAD) or the reduced ($FADH_2$). FAD oxidizes to gluconic acid, and the $FADH_2$ generated can be oxidized to FAD by oxygen, resulting in formation of hydrogen peroxide. The enzyme is typically immobilized on the surface of the electrode, and then the immobilized layer is covered with a protective membrane, often a polymer. The protective membrane stabilizes the enzyme and prevents potential interferants from

reacting with the enzyme. The electrode can then be placed in a solution containing the analyte, which can diffuse through the protective membrane and into the immobilized enzyme layer.

The glucose oxidase activity must be converted to an electrical signal to be used as sensor. The earliest use of enzymatic glucose sensors was based on the decrease in oxygen or the production of hydrogen peroxide.[49] The accuracy of oxygen concentration is limited by the natural variations in oxygen concentration at the electrode interface. The detection of the hydrogen peroxide is limited by possible interferants such as ascorbic acid and uric acid because the platinum electrode requires a potential of +0.5 - +0.6 V vs. silver/silver chloride. An alternative is to use oxidants other than oxygen to regenerate the oxidized form of (FAD). An ideal case would be the direct electron transfer between the active site on the enzyme and the electrode surface, but this is not possible because the active site is buried inside the protein. Therefore, the use of a mediator is used to achieve electron transfer.[50-52] Common mediators are ferrocene, potassium ferricyanide, ruthenium, and osmium. Problems associated with the use of mediator are that they are usually small molecules that can diffuse out of the membrane, causing loss of activity, and the oxidized mediator and oxygen compete for oxidation of the active site.

Another method for the determination of glucose concentration is the measure of the concentration of hydrogen peroxide produced by the reoxidation of the active site of the enzyme. Oxidation of hydrogen peroxide at the electrode surface is prone to interference, however; hence, other methods have been developed to measure hydrogen peroxide concentration.[53] One method is to use the enzyme horseradish peroxidase to

reduce hydrogen peroxide. This enzyme, unlike glucose oxidase, can achieve direct electron transfer between the active site and the electrode surface. Researchers have also attempted to use a selective membrane such as cellulose acetate[54] or chitosan[55], which is permeable to hydrogen peroxide but impermeable to common interferants such as ascorbic acid. Another approach to avoid interference is selective electrocatalysis. When an electrocatalyst is placed on the electrode surface, it is able to diminish the overpotential of the anodic oxidation of hydrogen peroxide, allowing the concentration of hydrogen peroxide to be determined at a much lower electrode potential. Therefore, the current caused by interferants can almost be eliminated.

Despite the abundance of work on these devices, only a handful of studies have attempted to apply this technology to neural monitoring. A recent study presented results using a glucose electrode for *in vivo* measurement of glucose in the rat brain.[28] These results are encouraging, demonstrating rapid measurements, but were limited to glucose only. Both lactate and glucose levels in brain microdialysate have been measured simultaneously in an enzyme packed bed system using GOx and lactate oxidase (LOx).[29] However, the time resolution of these methods is still limited by the microdialysis setup used for obtaining samples. Electrochemical sensors for multi-analyte sensing systems for neural measurements are not common and while, the electrochemical glucose sensors that are available are limited by response time and fouling.

2.33 Optical Devices

Fluorescence spectroscopy offers a potential solution to the problem because it possesses the desirable characteristics of specificity and sensitivity. Fluorescence-based optical sensors for glucose have been developed,[56-76] but have yet to be specifically developed for neurochemical monitoring. Some of these are still being investigated; the most successful are based on GOx as a catalyst for the oxidation of glucose and an oxygen-sensitive fluorescent indicator.[56,63] In these systems, the variation in fluorescence intensity as a function of the dissolved oxygen concentration is given by the Stern-Volmer equation:

$$I_0/I_c = 1 + K_{SV}[O_2], \tag{1}$$

where I_0 is the fluorescence intensity of the sensor in absence of oxygen, I_c is the fluorescence in a given dissolved oxygen concentration $[O_2]$, and K_{SV} is the Stern-Volmer quenching constant.

Optical sensing has some distinct advantages over electrochemical sensing schemes such as there is no electrical connection to the sample of interest, potential for simultaneous multi-analyte sensing via spectroscopy, and the proliferation of optical communication systems has led to the production of cheap and reliable optical sources and detectors. Biologically samples present possible disadvantages of optical sensing, including, limited penetration depth due to the scattering and absorbing properties of the sample, limited commercially available fluorescent indicators, and difficulties in calibrating changes in optical signals due to changes in analyte of interest.

2.4 Micro/Nanoscale Optical Probes

Fluorescence spectroscopy methods have become widespread tools, for analysing biologically important chemicals, analytes, and processes. Early use of fluorescent probes simply entailed injecting the liquid form of the fluorescent indicator into the biological sample. The sample would then be analyzed using an appropriate instrumentation, such as a spectrometer or a microscope. Often, however the indicator in its liquid form is toxic to biological samples or compartmentalizes into undesired regions of the sample. Realizing these problems, but desiring to take advantage of the benefits of fluorescence spectroscopy and fluorescent probes, researchers have developed methods of immobilizing the indicators while allowing interaction with the biological sample. When making a measurement, it is often important to be the least invasive as possible to the system one is studying. Biological samples are no exception, and the target sample is often in the milli- to microliter scale, so it is not surprising that the optical probes development are on the microscale and, with the advancement of nanotechnology, even the nanoscale.[77]

2.41 PEBBLEs

Probes encapsulated by biologically localized embedding (PEBBLEs) ranging in sizes from 20 nm to 200 nm in diameter have been developed by the Kopelman group at the University of Michigan. These sensors are fabricated using microemulsion techniques and consist of a polymer matrix containing dyes and/or enzymes. The

intended application of PEBBLEs is for use in intracellular monitoring of pH[9] and other important analytes such as glucose[78], sodium[79], calcium[9], zinc[80], oxygen[11], and potassium[10]. The important characteristics of these sensors are: (1) because the indicator dye is embedded in the polymer matrix, the dye is protected from the environment and the environment is protected from the dye; (2) via immobilization of the chemistry, multiple dyes can be in one PEBBLE, thus allowing ratiometric monitoring; (3) calibration can theoretically be done *in vitro* and still be valid *in vivo*, making analysis much easier; (4) the polymer matrix can provide a biocompatible surface.

Disadvantages associated with PEBBLEs lie in the fabrication process. Depending on the dye or combination of dyes and/or enzymes, unique fabrication protocols have to be established for each new material. Another problem is that the emulsion process does not guarantee uniformity from sensor to sensor within the same fabrication batch or uniformity from batch to batch using the same process. The sensors also suffer from leaching of the dye from the polymer matrix.[78]

The PEBBLEs designed for glucose sensing have an average size of 45 nm in diameter, small enough for intracellular glucose monitoring. Two sensing schemes were used (1) the glucose oxidase coupled oxygen sensitive ruthenium compound with a second dye that is insensitive to the quenching of molecular oxygen using a single excitation for ratiometric emission measurements and (2) the same as above but the second dye is chosen to allow ratiometric excitation measurements[78]. The intended lifetime of the sensors was approximately one hour; over that time the researchers saw no significant leaching of the dye from the polymer matrix. The dynamic range (where 95% of the total change occurs) of the sensors was approximately 0.3 mM to 8 mM glucose,

with a linear range of 0.3 mM to 5 mM with a correlation coefficient of 0.997. For a step

change of 0.26 mM to 3.92 mM the sensors had a response time of approximately 200 sec

and were reversible. The sensors were also placed in increasing concentrations of bovine

serum albumin (BSA), and the change in fluorescence intensity ratios was at most 4%.

The authors claimed that the *in vitro* calibrations remained valid, but the response to

glucose in BSA was not tested. The PEBBLEs sensors have been designed for use as

research tools for laboratory use.

2.42 The "Smart Tattoo"

In initial work by Shultz, immobilized concanavalin A (Con A) was used as a

receptor for competing species of FITC labeled dextran and glucose.[81,82] In the absence

of glucose, the TRITC-Con A binds with the FITC-dextran and, due to fluorescence

energy transfer (FRET), excitation of the FITC results in TRITC emission. As the

glucose concentration increases, the FITC-dextran is displaced by glucose, causing

increased FITC emission. The smart tattoo is a concept for minimally-invasive

monitoring for diabetics, using micron-size hydrogel bead which can be implanted into

the epidermis layer of the skin.[6] The measurement is proposed to be performed by a fiber-

optic probe containing fibers for excitation light delivery and emission collection or other

appropriate optical system that can be held to the skin at the site of implantation. The

competitive-binding assay used for glucose measurement is comprised of TRITC labeled

Con-A and FITC labeled dextran both entrapped in the hydrogel.

In contrast to the PEBBLEs sensing scheme using glucose oxidase, an advantage using the competitive-binding assay is that there is no consumption substrates or production of new chemicals. The fabrication of the hydrogel beads for the smart tattoo suffers from the same disadvantages as the PEBBLEs. Another disadvantage more specific to the Con A-dextran system is that there is debate as to whether the sensing scheme is reversible.[83] Figure 7 is an illustration depicting the two fluorescence sensing methods described above and a generalized comparison of the two.

GOx Scheme	Con A Scheme
Advantages:	Advantages:
Reversible	Non-Consuming
Specific	Specific
Disadvantages:	Disadvantages:
Consumes O_2	May not be reversible
Limited enzyme life	Can not be completely immobilized

Figure 7. Illustration comparing fluorescence sensing schemes: oxygen indicator coupled with GOx and competitive binding assay.

2.43 Fiber and Submicron Fiber Probes

Glucose sensitive fiber probes based on both sensing schemes described above have been developed[57-62,64-67,70,72], but have not been applied to neurochemical monitoring. These fiber probes range in sizes from millimeter to submicron diameters with the

sensing chemistry immobilized at the end of the optical fiber, while the opposite end is connected to a light source and detector. The larger fiber probes are limited in spatial resolution as well as the sensing applications due to the size. The methods of immobilizing the sensing chemistry limit the response time and sensitivity, due to large diffusion lengths. Submicron fiber-optic glucose sensors were developed to address these issues.[76] The response time was reduced to approximately 2 sec. and the detection limit was approximately 1×10^{-15} mol. However, reducing the size of the fiber probe addressed the problems of spatial resolution and response time; these probes had an operating lifetime of only 4-6 days due to the loss of the sensing chemistry from the immobilized polymer matrix.

2.44 Other Optical Glucose Sensing Methods

In addition to the sensing schemes mentioned above, other non-neural glucose sensing techniques based on fluorescence have been developed. One method uses the intrinsic fluorescence of deactivated GOx to estimate glucose concentrations.[84] The main problem with this method is that the intrinsic fluorescence of GOx in excited by UV light, which would also excited proteins found in biological samples. Also, scattering and absorption of excitation and emission wavelengths could be limiting as well. Another method requires GOx labeled with to fluorescein derivative and is immobilized in a sol-gel matrix.[85] The origin of the change in fluorescence signal due to a change in glucose concentration is not clearly understood, but it requires the sol-gel matrix. The size of the sol-gel matrix was approximately 9 x 20 x 1 mm. Similar to the oxygen-based GOx sensing schemes, pyrene has been labeled to GOx, and fluorescence sensing due

quenching of pyrene by molecular oxygen as a result of the enzymatic reaction has been investigated.[86] The previous two examples would not be feasible sensing schemes for neurochemical measurements because of large size of the sol-gel matrix and direct injection of modified GOx into a biological sample would cause cell death.

Significant efforts have been made toward developing optical methods for the detection of glucose. The potential for a fast, non-consuming, and minimally invasive optical sensor seems to be an obvious candidate for neural glucose sensors. Surprisingly there are few known optical sensors developed specifically for neurochemical monitoring. The current glucose sensors available that could possibly be adapted to neural glucose sensing suffer from poor spatial resolution, reversibility, the stability of the immobilization techniques, sensitivity, and the inability to calibrate *in vitro* and use *in vivo*. Improvements in optical technology and instrumentation such as portable spectrometer and light sources and the development of novel fabrication techniques for the immobilization of sensing chemistry provide a basis for new glucose sensor development.

Many of the disadvantages of optical glucose sensing methods are related to the techniques used for fabrication and immobilization of sensing components. Specifically, the methods used can be describes as top-down methods, in which macro-fabrication techniques are used to "build" micron size sensors. In the last decade, micro- and nanotechnologies have been developed to fabricate "bottom-up" methods of fabrication and assembly. The following section is a discussion on the LbL self-assembly method that has been developed over the past ten years.

2.5 Layer-by-Layer Self Assembly

2.51 General

The highly controlled assembly of particles and molecules onto arbitrary surfaces, one aspect of nanotechnology, has advanced rapidly over the last ten years. Various scientists have demonstrated the ability to successively layer nanoscale charged particles onto a variety of substrates using a very general technique. The principle of alternate adsorption for film formation was invented for charged colloidal particles in the pioneering work of Iler.[87] Later, a related method for film assembly by means of alternate adsorption of linear polycations and polyanions, was introduced.[88-91] This assembly scheme is shown in Figure 8.

{Polycation/Polyanion}$_n$
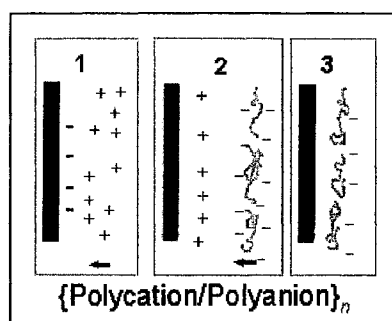
Figure 8. Cartoon of LbL assembly on a planar template.

The main idea of the method consists of resaturation of polyion adsorption, resulting in alternation of the terminal charge after of each concsecutive layer deposition. This idea is extremely general and implies that there is no principle restriction on the choice of polyelectrolytes. There is the possibility to design ultrathin ordered films in the range of 5 to 1000 nm, with precision better than 1nm, and a definite knowledge of their molecular compositions. The technique has been applied successfully to many polyions

and dyes,[88-97] for the assembly of organized protein multilayers,[95] viruses, and charged nanoparticles. [92,94] The protein assembly procedure is very general, and multilayer films containing ordered layers of protein species have been assembled by means of alternate electrostatic adsorption with positively charged polyethyleneimine (PEI), poly(allylamine hydrochloride) (PAH), poly(dimethyldiallylammonium chloride) (PDDA), and chitosan or with negatively charged PSS, DNA, and heparin. The pH of the protein solutions is set apart from the isoelectric point so that proteins are sufficiently charged under the experimental conditions. Water soluble proteins, including cytochrome c and P450, lysozyme, histone type YIII-S, myoglobin (Mb), pepsin, horseradish peroxidase (POD), hemoglobin, glucoamylase (GAM), concanavalin A (Con A), albumin, glucose oxidase (GOx), catalase, invertase, diaphorase, acteriorhodopsin, and immunoglobulin IgG were used successfully in the assemblies. [94,98-100]

2.52 Colloids

The assembly process on solid supports has also been extended to assembly on the surface of charged particles with diameters of 100 to 500nm (such as charged polystyrene latexes).[101,102] In this process, the polycation solution is added to the negatively charged latex. After adsorption, saturation is reached; the latex is separated from the polycation solution by centrifugation and is exposed to the polyanion solution. Figure 9 is a cartoon showing an example of how the assembly proceeds.
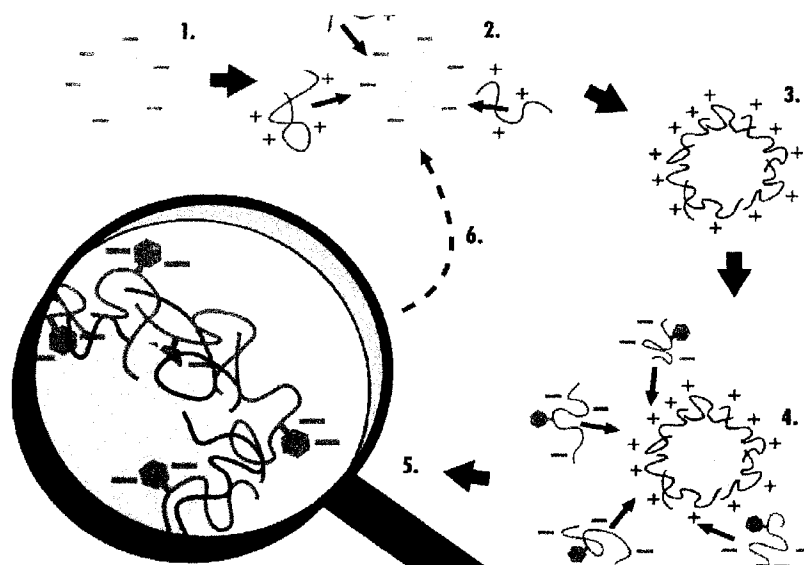
Figure 9. Cartoon of LbL assembly on colloidal template.

It has also been demonstrated that hollow micro- and nanospheres can be fabricated by performing this procedure on a template, such as MF and silica particles that can later be dissolved, thereby leaving a hollow polymeric shell. The hollow spheres can then be loaded with enzymes[103], sensing indicators[77,104], and other materials.[105] Work on these interesting capsule structures has generated great interest over the last five years.[106-109]

2.53 Enzymes

The LbL deposition of multilayered enzyme films on macro, micro and nano-templates is a promising approach for creating organized films of molecular "engines." The LbL process allows tailored enzymatic activity[14], and has applications in bionanoreactors[19,110,111] and sensors[18112-114]. As an example, eighteen layers of PEI/GOx were deposited onto a quartz substrate with a linear increase in mass per step.[115] It has been shown that enzymatic activity of glucose isomerase, glucoamylase, glucose oxidase

and peroxidase was preserved in multilayers with polyions.[116] The LbL process was used

to deposit multilayer enzyme films on microparticles, and it was demonstrated that

enzyme activity increases linearly with number of enzyme layers.[110,111] Furthermore,

capsules fabricated using LbL have been successfully loaded with the enzyme urease and

it was shown that the enzymatic activity was initially reduced by 87% as compared with

free enzyme; although the activity of the enzyme in the film was preserved after 5 days

while the activity of free enzyme had dropped 45%.[103] This observation indicates the

multilayer films, while reducing the initial activity of the enzyme, serve as to protect the

enzyme from degradation.

2.54 Sensing Applications

Before the start of this research project, the employment of LbL-assembled films

for optical sensing was limited to a few examples. Tripathy's group demonstrated

fluorescent pH-sensitive films on planar templates using direct assembly of dye.[16]

Similar work was demonstrated by Rubner's group using an absorbing dye.[21] A ferric

ion sensor based on acridine-containing polymer assembled in multilayer films has also

been proposed, but no experimental validation of function in multilayer assemblies has

been given [17]. Recently, fiber optic based sensors for oxygen using LbL films have been

developed. Moving beyond planar templates, oxygen sensing has been demonstrated

using solid colloidal templates[117] and hollow polymeric shells loaded with sensing

chemistry for oxygen,[104] sodium[118], and potassium[77] has been developed. The use of LbL

films for humidity sensing based on interferometry was developed using fiber optic

probes[119].

The ability to deposit films using LbL self-assembly on such a wide variety of substrates and the availability of diverse range of materials makes this process an attractive method for developing optical sensors. The ease and mildness of fabrication would be very well suited for applications ranging from tissue culture substrates with optical surface sensing films, fiber-optic probes designed for measurements in both research and clinical settings, and fabrication of micro/nanoparticle based sensors for implantation for acute neurochemical measurements. Development of such sensor requires suitable physical models that mimic *in vivo* conditions.

2.6 Brain Phantoms & Particle Delivery

Very little information is available in the literature regarding suitable brain phantoms for nanoparticle infusion protocols. Gillies et al. have used agarose gels to provide a test bed for experiements aimed at validating poroelastic models of infusion with brain tissue.[120] It was found that similarities between volume-of-distribution and pressure profiles in the *in vivo* and *in vitro* cases has affirmed this general approach by the similarity between the porosity of the brain and that of the nanoscale polymeric structure of the gel. The large, fluid-filled void fraction of the brain[121] , about 2%, is mimicked by the equivalent of an overall porosity associated with the gel's cross-linked polymeric strands. In studying the relationship between flows in brain tissue and in gels, nanoparticles (8-12 nm) were infused into a 0.6% agarose gel, a satisfactory material for a brain in terms of macroscopic and microscopic response to the infusion process.[122]

The use of agarose gels as a brain phantom will not only allow protocols for nanoparticle sensor delivery to be developed but will also serve as a test bed for sensor performance testing and design. The ability to immerse the phantom in solutions that mimic conditions found *in vivo* will allow *in vitro* calibration of the sensors for both nanoparticle sensors as well as fiber probe sensors. The results of such testing will be critical, in providing a feedback loop for sensor theoretical sensor modeling and design.

In summary, it has also been shown that there are rapid transient changes in neural glucose concentrations. In addition, glucose is consumed anaerobically in astrocytes, producing lactate released into the extracellular space and then used aerobically by neurons. These events occur at a time scale that hidden from the current neural glucose and lactate sensing method, microdialysis sampling. While electrochemical sensors have been developed, they are not widely available and do not allow mulitanalyte sensing. Fluorescent optical probes sensors in the form of polymer micro- and nanoparticles are being developed as glucose sensors but have not yet been applied to neurochemical monitoring. Thus, there is a need for a fast, multianalyte optical sensor for neurochemical measurements. The development of LbL assembly method, allows deposition of films with precise control and compositional flexibility on a wide variety of substrates. The following chapter will discuss the design and theory of using LbL assembly methods to fabricate glucose sensors comprised oxygen sensing fluorophores, oxygen insensitive fluorophores, glucose oxidase, and polyelectrolytes, as well as the optical and chemical properties of the components.

CHAPTER 3

DESIGN AND THEORY

This chapter describes the use of mathematical models for the proposed sensors. The architecture design discussed below is general, in that it is not specific to the template on which the films are deposited. While the ultimate objective is to create nanoparticle-based sensors, fabrication and characterization of glucose sensors was performed on optical fibers, which are more suitable for rapid fabrication and experimentation. Therefore, the fabrication modeling to predict spectral output of fluorescent LbL films is based an optical fiber template. It is noteworthy that the model can easily be adapted for use with nanoparticles simply by changing the coordinate system and boundary conditions, as should be obvious from the discussion.

The optical properties discussed concern the delivery of excitation light and the collection of fluorescence emission from implanted nanoparticle-based sensors. This description of tissue and light interaction aids in the design of the optical properties of the sensors, such as the SNR, as well as orientation of the implanted sensors relative to the optical fiber(s) used to deliver and collect light.

The sensing chemistry and architecture of the films is addressed to provide insight into the function and structure of the sensor. The function of the oxygen sensitive dye and the enzyme are discussed, as well as how the sensing chemistry might effect the charge distribution and conformation of the polyelectrolyte films.

Last, the remaining sections of this chapter deal with models developed to aid in the fabrication, function, and delivery of the sensors. A fabrication model was developed, which is independent of the template, and was used to predict the spectral output of the sensing chemistry. The result of this model, when applied to nanoparticle templates, was used in a mathematical model that describes the delivery of the sensors and predicts the resulting spectrum based on number of sensors that are infused. Furthermore, the fabrication model results, using an optical fiber template, are presented and compared to experimental results. This film architecture was used in developing a model that describes the diffusion and reaction of the substrates, glucose and oxygen. The model was used to predict the change in oxygen concentration in the sensing regions of the film architecture. The change is oxygen concentration was then related to changes in florescence peak ratio described by the Stern-Volmer equation, which was determined from experimental results.

3.1 Ultrathin Film Architecture

The generic architecture for the sensor films is illustrated in Figure 10. The illustration is a simplified description, in that polyelectrolyte films are interpenetrating and do not have discrete boundaries. The order of films was chosen to allow for an

oxygen-sensing zone to be separated from the bulk solutions by a reaction zone. This configuration allows the substrates to diffuse into the films, where they then are consumed, thereby reducing the concentration at the boundary between the sensing and reaction zone. To model the reaction and diffusion of enzymatic substrates, boundary conditions (BCs) are needed to solve the partial differential equations (PDEs). These BCs relate to physical description of the film components on the template and the restrictions placed on the diffusion of the substrates, as given below.
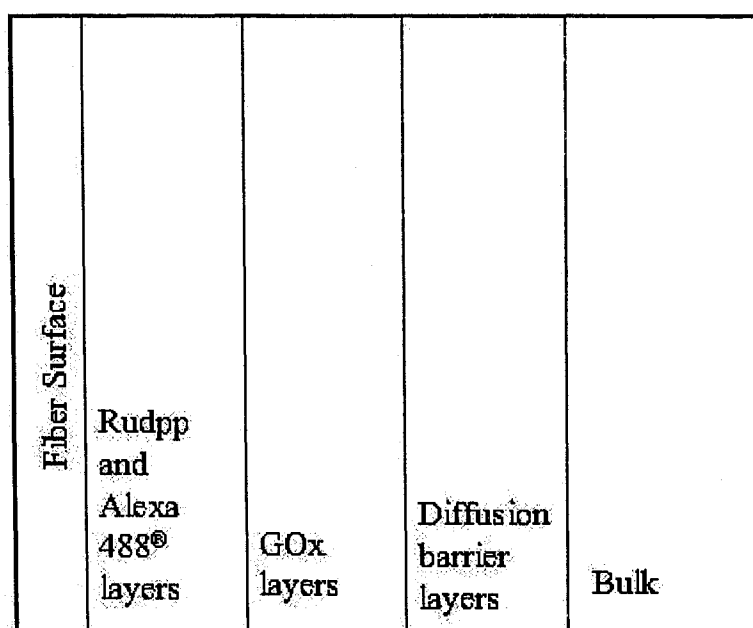
Figure 10. The architecture of the film on an optical fiber template.

Starting from the fiber surface, the first region contains multilayers comprising (PAH-488/PSS). These are loaded with Tris(4,7-diphenyl-1,10-phenanthrolin)ruthen-ium(II) dichloride (Ru(dpp)) and therefore serve as the sensing layers, including the internal reference. The second group of film layers is composed of (PEI/GOx), which serves as the reaction zone. The third layer serves to effectively reduce the diffusion rate

of the substrates. The need for this film will be discussed below in the section on

functionality modeling.

3.2 Optical Properties

The implantation of optical nanoparticle sensors in rat brain necessitates the

investigation of the light and tissue interactions. Understanding the propagation and the

distribution of light in biological tissue is important for the effective development of

optical chemical sensors. Biological tissue is a turbid medium, in that it has both

scattering and absorbing components. Monte Carlo simulations of photon paths give

accurate prediction of light distribution in tissue, but are generally complex and require

intense computation. To simplify the analysis here, a simplification using Beer's law was

used in conjunction with the properties of optical fibers, to estimate the propagation of

light in the proposed sensing scheme. The equation for Beer's law is,

$$I(z) = I_0 e^{-\mu_{eff} z} \tag{2}$$

where I is the intensity at depth z, I_o is the initial light intensity, μ_{eff} is the effective

absorption coefficient and z is depth. The intensity will drop by e^{-1} or 1/3 after it has

traveled a distance $z = 1/\mu_{eff}$ which is known as the penetration depth. The probability of

transmission of a photon past a pathlength z is the same regardless of whether the photon

path is a straight line or highly scattered in an optically turbid medium. According to

experimentally derived results from Svaasand et al., they approximated $\mu_{effective}$

(scattering and absorption coefficient combined) for human adult brain tissue at the

wavelengths 488 nm, 515 nm and 660 nm to be 19.5 cm^{-1}, 15.4 cm^{-1}, and 9.8 cm^{-1}

respectively.[123] The corresponding penetration depth for each wavelength would be: 513

μm, 651 μm, and 1030 μm, respectively as seen in Figure 11. These wavelengths are the

approximate values of light that will be used in the sensing scheme; 488 nm is the

excitation (blue), 515 nm is the internal reference emission (green) and 660 nm (red) is

the oxygen sensitive fluorophore emission. The intersection of the colored lines with the

1/e (black) line represents the distance at which the intensity loss is approximately 30%.
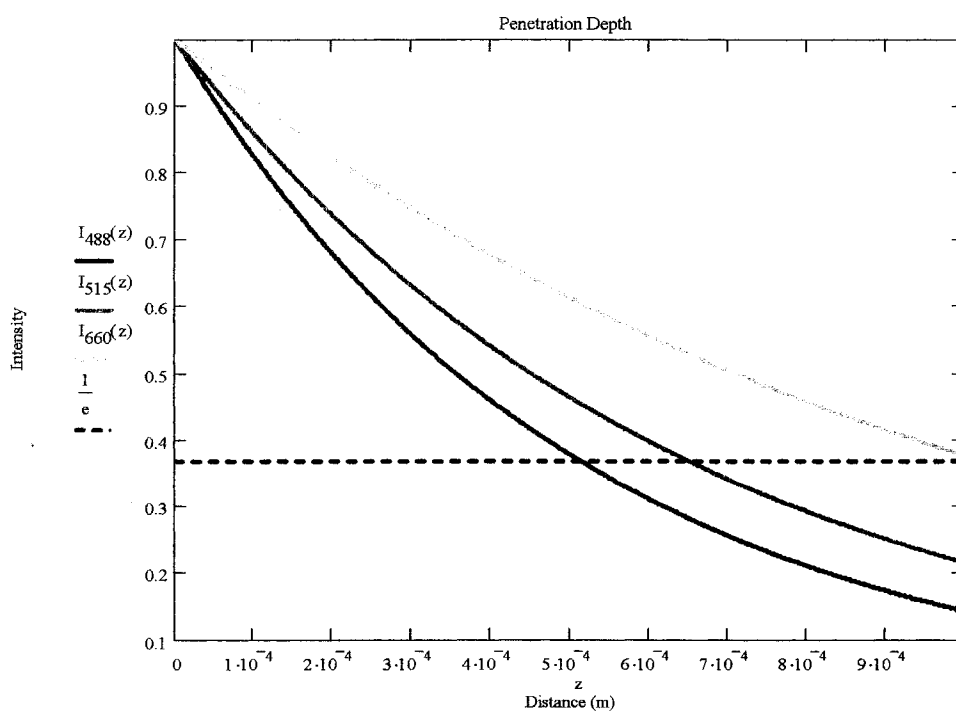
Penetration Depth

Figure 11. Plot of the penetration depth for 488 nm (red), 515nm (blue), and 660 nm
(green) and the 1/e intensity loss (black).

A 200 μm diameter fiber was chosen to deliver excitation light and collect

fluorescence emission light because it was approximately the largest diameter for a single

fiber that can be introduced into the implanted cannula guide (1.2 mm OD, Plastics 1,

C309GA). The factor in determining how much light a fiber collects and emits is its

acceptance angle. The standard measure of acceptance angle, illustrated in Figure 12, is

the numerical aperture (NA), which is defined as

$$NA = n_0 \sin(\theta) \tag{3}$$

where n_0 is the refractive index of the fiber and θ is the half acceptance angle of the fiber.

The 200 μm fiber used in this work has a NA of 0.48 and a n_0 of 1.5. Using these values,

solving for θ, yields a half angle of approximately 18°.
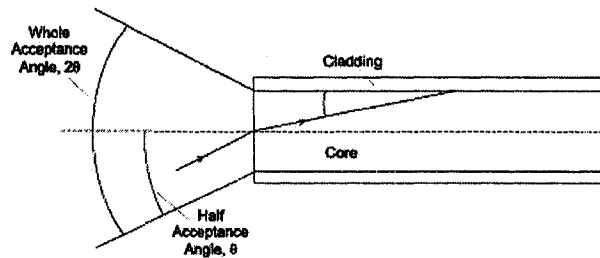
Figure 12. Diagram of the numerical aperture of an optical fiber.

According to the optical properties of the brain, the excitation light will be the

limiting wavelength in skin depth; therefore, the implanted particles must be placed no

further than 513 μm from the fiber end. Figure 13 illustrates that, by using simple

geometry, the lateral length of the beam that is 513 μm from the fiber end with a whole

acceptance angle of 36°, will be approximately 1 mm. The fluorescence emission from

the particles will be isotropic, and being shorter wavelengths, will have longer

penetration depths.
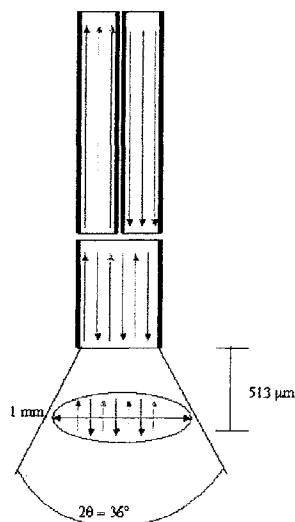
Figure 13. Illustration of the optical fibers used to delivery light and collect fluorescence emission from the sensor, which are connected to a Y adapter.

The geometry of the light propagation defines approximate physical restrictions on the size of the bolus of infused particles that can be efficiently excited by the fiber probe. This information, combined with the fabrication and infusion modeling can be useful in designing the sensor to have appropriate spectrum and SNR.

3.3 Chemical Properties

The components used to fabricate the glucose sensor include GOx (Sigma Aldrich, G7141), Ru(dpp) (Sigma Aldrich, 76886), Alexa Flour 488® (Molecular Probes, A-20000) and polyelectrolytes PAH (Sigma Aldrich, 283215), PSS (Sigma Aldrich, 434574) and PEI (Sigma Aldrich, P3143). The chemical properties of these molecules affect both the function of the sensor, as well as the structure of the structure. The sensing scheme chemistry is discussed in terms the structure and function of GOx, while

Ru(dpp) is discussed in terms of the quenching of fluorescence by molecular oxygen. The chemical properties of the polyelectrolytes will be discussed in terms of their influence on the structure of the films.

Glucose oxidase is a homodimeric enzyme.[124] Each subunit of this protein contains one coenzyme molecule of flavin adenine dinucleotide (FAD).[125] Each GOx monomer has two distinct domains: one that binds non-covalently, but very tightly with the FAD moiety, and another that binds the β-D-glucose substrate. The first area consists mainly of β-sheets, and the second one is primarily 4 α-helices supporting anti-parallel β-sheets.[126] The enzyme catalyzes, in the presence of molecular oxygen, the oxidation of β-D-glucose into gluconic acid and hydrogen peroxide. The conversion of β-D-glucose to gluconic acid involves the transfer of two protons and two electrons from the substrate to the flavin moiety.[127] This reaction is thus used in the fabrication of a glucose sensor by coupling the enzyme to an oxygen sensitive fluorophore. Therefore, changes in glucose concentration can be indirectly measured by measuring changes in oxygen. The measurement of oxygen changes is accomplished by using an oxygen sensitive fluorophore.

As mentioned previously, Ru(dpp) fluorescence emission is quenched by molecular oxygen and follows the Stern-Volmer equation:

$$\frac{I_0}{I_c} = 1 + K_{SV}[O_2] \tag{4}$$

where I_0 is the fluorescence intensity of the sensor in absence of oxygen, I_c is the fluorescence in a given dissolved oxygen concentration $[O_2]$, and K_{SV} is the Stern-Volmer quenching constant.[128] The sensing scheme follows a modified Stern-Volmer equation,

shown in Figure 14, in which the changes in peak ratios are measured instead of changes

in the Ru(dpp) emission intensity. The peak ratio is the ratio of the peak intensity of the

Ru(dpp) emission to the peak intensity of the PAH-488 emission.
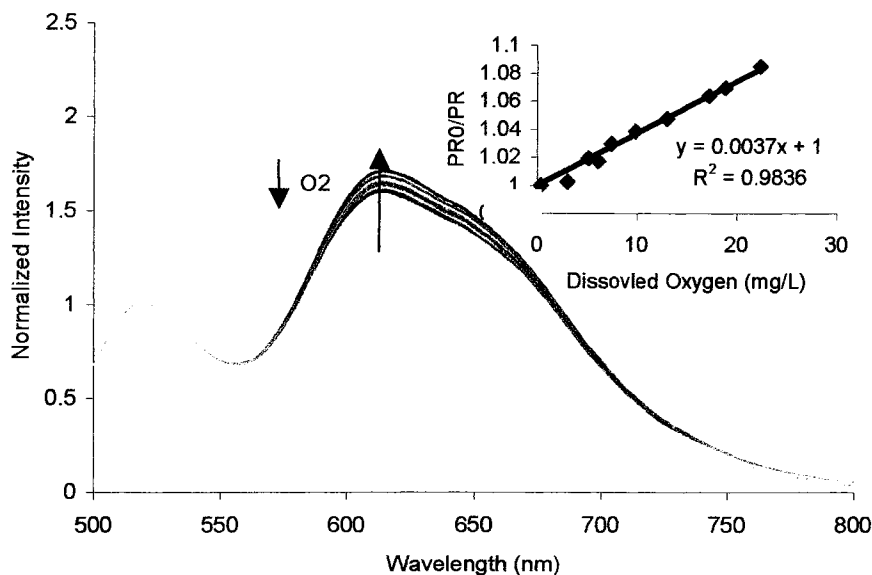
Figure 14. Spectra from films with the architecture $(PAH-488)_{11}$ + Ru(dpp) demonstrating increase in the Ru(dpp) emission with decrease in oxygen concentration. Inset depicts the change in peak ratio in the form of the Stern-Volmer equation.

The general properties of polyelectrolytes and their role in LbL films were

discussed in detail in Chapter 2.5. The chemical properties in regards to structure

dynamics of the polyelectrolytes will be discussed in detail in the results section in

Chapter 5.4.

3.4 Modeling

3.41 Fabrication Modeling

The LbL process lends itself to modeling due to the linear step growth of the film fabrication. If the mass per surface area coverage is known for a given adsorbate; then the number of molecules per layer can be estimated. Polyelectrolyte mass coverage values have been determined using QCM experiments, in which the change in frequency due to the adsorption of the polyion is related directly to the change in mass by the Sauerbrey equation.[129] Furthermore, polyelectrolytes with amine groups, such as PAH and PDDA, can be covalently labeled with fluorophores having succinimidyl ester or isothiocyanate groups, thereby giving a ratio of fluorophore molecules to polyion molecule or labeling ratio, which can be determined from UV-Vis absorption experiments.[130] Given the labeling ratio, mass coverage of labeled polyelectrolyte and the number of layers deposited on a template, the total number of fluorescent molecules can be estimated. This information, combined with the extinction coefficient of the fluorophore, may be used to estimate the resulting fluorescent spectrum expected from a given number of layers. This ability is especially useful when considering fabricating multilayer thin films containing two or more fluorescent dyes, where the desired spectral output can be modeled and then the required number of layers may be determined for a desired template, as given in the following equation

$$F_{rel}(\lambda_{em}) = \sum_{k=1}^{\substack{K=\# \ of \\ luminescent\ components}} I(\lambda_{ex}) \cdot \varepsilon_k(\lambda_{ex}) \cdot QY_k \cdot SC_k \cdot R_k \cdot NL_k \cdot F_k(\lambda_{em})$$

$$\Rightarrow I(\lambda_{ex}) \cdot \left[\begin{array}{l} \varepsilon_{bkg}(\lambda_{ex}) \cdot QY_{bkg} \cdot C \cdot F_{bkg}(\lambda_{em}) + \\ \varepsilon_{ref}(\lambda_{ex}) \cdot QY_{ref} \cdot SC_{ref} \cdot R_{ref} \cdot N_{ref} \cdot F_{ref}(\lambda_{em}) + \\ \varepsilon_{ind}(\lambda_{ex}) \cdot QY_{ind} \cdot SC_{ind} \cdot R_{ind} \cdot N_{ind} \cdot F_{ind}(\lambda_{em}) \end{array} \right]$$

(5)

where F_{rel} is the relative fluorescence at λ_{em} emission wavelength, I is the initial

fluorescence intensity at λ_{ex} excitation wavelength, QY is the quantum yield, SC is the

surface coverage of the PAH-dye, R is the labeling ratio for the PAH-dye, and NL is the

number of layers of the PAH-dye. The subscripts bkg, ref, and ind, refer to the

background, reference, and indicator. The spectra depicted in Figure 15 are

representative of the ability to customize the spectral output by the adsorption of the

desired number of fluorescent bilayers. The model given in equation 5 was used to

predict the spectral output for the exact same film architecture, simply by specifying the

number of layers adsorbed for each fluorophore conjugated to PAH. The results of the

model are depicted in Figure 16.
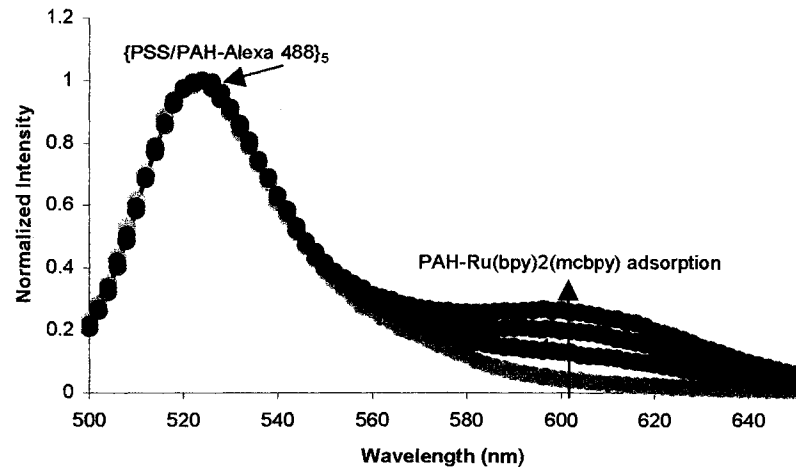
Figure 15. Experimental data demonstrating increasing RU(bpy)2(mcbpy) emission with increasing deposition of (PAH-Ru(bpy)2(mcbpy)/PSS)$_3$ bilayers after initial adsorption of (PAH-488/PSS)$_5$ bilayers.
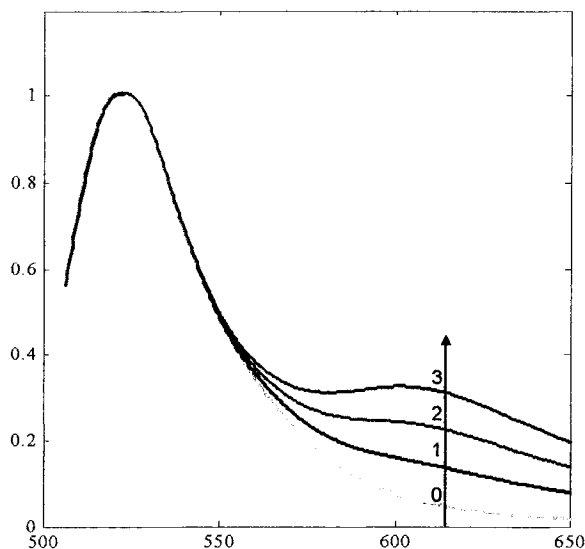
Figure 16. Predicted spectral output for thin films with the architecture (PAH-488/PSS)$_5$ + (PAH-Ru(bpy)2(mcbpy)/PSS)$_3$.

When dealing with a fluorophore that is not (e.g. is adsorbed from solution into pre-deposited films) conjugated to a polyelectrolyte, the number of dye molecules in the films can be estimated from absorbance measurements collected from the fluorophore loading solution before and after exposure to the films. Using the Beer's law, the total concentration can be determined and for a given volume of particles. The total fluorophore concentration can be divided by the estimated number of particles to yield the fluorophore concentration per particle.

3.42 Infusion Modeling

The predicted fluorescent spectrum for a given film architecture containing multiple fluorophores can be extended for predicting the spectrum collected from nanoparticles during an infusion process. It is beneficial to predict the spectral properties

for a given volume of sensors infused into a rat brain because: (1) to increase spatial resolution (e.g. increase confidence that signals are obtained from targeted tissue volume), it is important to minimize the number of infused particle to the measurement site; (2) more particles infused will disturb more tissue, so need to minimize the number of particles infused; (3) the sensing scheme consumes both oxygen and glucose, so it is important to minimize local consumption of the substrate in order to make accurate measurements and not disrupt normal brain function; and (4) scattering and absorption by the tissue will affect the fluorescence signal collection, therefore it is important to design fluorescent films on the nanoparticles with an appropriate SNR. Since LbL assembly allows one to engineer sensors with specific spectral characteristics because one is able to control the number of fluorescent molecules per particle, a model that relates the fluorescence output spectrum as a function of the number of particles has been developed. Beginning with a known concentration of particles (10 % solids), the number of particles infused can be estimated as

$$N_{particles} = \int_0^{t_f} conc(\frac{d}{dt}vol)dt \qquad (6)$$

where $N_{particle}$ is the number of particles, *conc* is the particle concentration of the infusate, $d/dt*vol$ is the flow rate, and t_f is the time of infusion. Once the number of particles infused is known, the concentration of fluorophore for all particles can be estimated by multiplying $N_{particles}$ by the concentration of dye per particle for a given number of layers, which is determined from the fabrication model described earlier.

The fluorescence output may then be approximated by the following equation

$$F(I) = IQ\varepsilon lc \tag{7}$$

where F is the output fluorescence intensity, I is the fluorescence emission spectrum of the fluorophore being modeled (normalized to the maximum emission intensity), Q is the quantum yield of the fluorophore, ε is the extinction coefficient of the fluorophore, l is the path length, and c is the concentration of the fluorophore for all particles. Using separate equations for both dyes and then adding them together, results in the estimated spectrum for an infusion, as seen in Figure 17.
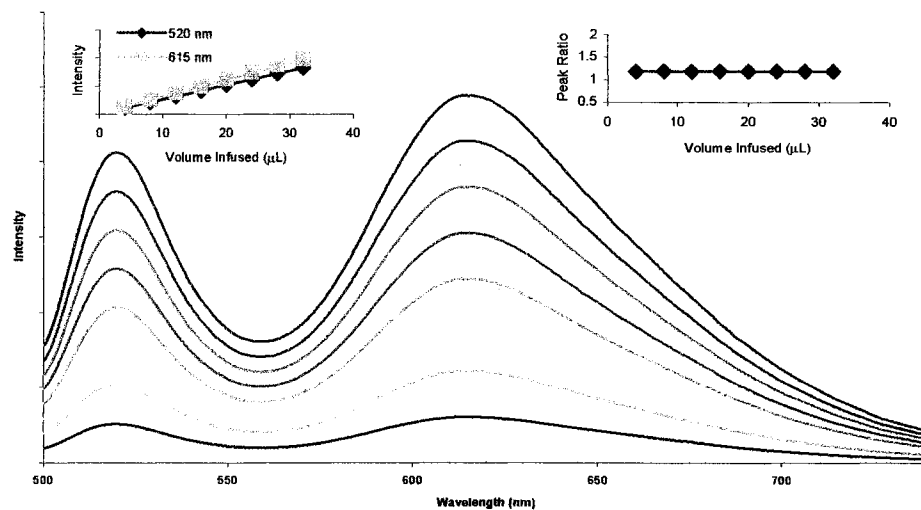
Figure 17. Infusion model output for 301 nm particles with (PAH-488/PSS)$_{11}$ + Ru(dpp), infused at a flow rate of 0.3 μL/min.

It is seen in the graph that the predicted peak intensities increase linearly with the volume infused because the model does not consider the physical properties of the optical fiber, such as the NA, and the absorption and scattering properties of the tissue. Although, by performing a regression on each of the peak intensities, it is possible to use the resulting equation to predict the number of particles infused by an increasing

spectrum. This model will be related to infusion results from both in vitro and in vivo experiments discussed in chapter 5.

3.43 Functionality Modeling

The modeling of the enzymatic reaction and diffusion of substrates was concurrently developed in cooperation a fellow student and is described fully as part of a thesis for a Master of Science in Chemical Engineering.[131] The important parameters of the model are (1) geometry of the template used for LbL film deposition; (2) the diffusion coefficients of the substrates in all regions; (3) the thickness of films; and (4) the concentration of the enzyme in the films. The model was developed using a coupled reaction-diffusion scheme[132] as will be briefly described here.

The mechanism of the reaction of glucose (A) with oxygen (C) in the presence of GOx is given by the following scheme:

$$A + E \underset{k_1,k_{-1}}{\longleftrightarrow} X_1 \xrightarrow{k_2} F + gluconate$$
$$F + C \underset{k_3,k_{-3}}{\longleftrightarrow} X_2 \xrightarrow{k_4} E + H_2O_2 \tag{8}$$
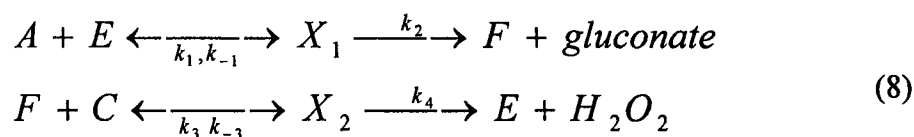
where E is the GOx, F is the enzyme-substrate complex, k_1, k_2, k_3, k_4 are the forward reaction rate constants, and k_{-1} and k_{-3} are the backward reaction rate constants.

Reaction terms were developed based on michaelis-menton and, using, the pseudo steady state hypothesis, six partial differential equations were reduced to two PDEs. The resulting equations with appropriate boundary conditions (BCs) and constants, given below, were then solved using the MATLAB software package.

$$x = 0:$$

$$A(0,t) = C_g$$

$$C(0,t) = C_0$$

$$x = L:$$

$$\frac{\partial A(x,t)}{\partial x} = 0$$

$$\frac{\partial C(x,t)}{\partial x} = 0$$

$$\frac{\partial A}{\partial t} = D_g \frac{\partial^2 A}{\partial t^2} - k_1 AE + k_{-1} X_1 \tag{9}$$

$$\frac{\partial C}{\partial t} = D_o \frac{\partial^2 C}{\partial t^2} - k_3 CF + k_{-3} X_2$$

$$X_2 = \frac{K_3 CF}{K_{-3} + K_4} \tag{10}$$

$$X_1 = \frac{K_1 A[E_t(K_{-3} + K_4) - F(K_{-3} + K_4 + K_3 C)]}{K_1 A + K_{-1} + K_2} \tag{11}$$

$$F = \frac{K_1 K_2 AE_t(K_{-3} + K_4)}{(K_{-3} + K_4 + K_3 C)K_1 K_2 A + \left\{ \frac{[K_3 C(K_1 A + K_{-1} + K_2)][K_{-3} + K_4 - K_3]}{K_{-3} + K_4} \right\}} \tag{11}$$

$L = 30 \mu m$
$k_1 = 10^5 \, M^{-1} sec^{-1}$
$k_{-1} = 3 \times 10^3 \, sec^{-1}$
$k_2 = 300 \, sec^{-1}$
K_m (for glucose) = 33mM
$k_3 = 10^6 \, M^{-1} sec^{-1}$
$k_{-3} = 150 \, sec^{-1}$

$k_4 = 50 \, sec^{-1}$
K_m (for oxygen) = 0.2 mM
C_0 (conc of oxygen) = 2mM
$C_g = 0.2 \, mM \sim 10mM$
$E_t = 0.5 \, mM$
$D_g = 9.87e\text{-}14 \, m^2 \, sec^{-1}$
$D_0 = 1.15e\text{-}9 \, m^2 \, sec^{-1}$

3.5 Predicted Performance

Modeling of sensor function was performed using the *pdepe* function in MATLAB

to solve the PDEs mentioned previously (MATLAB code was provided in the appendix).

The bulk glucose concentrations were varied from 0 to 50 mM and the bulk oxygen

concentration was held constant at 2 mM. The time of the reaction was 20 sec, assumed to be steady-state. The output of the model was designed to yield the oxygen concentration in the sensing region of the films as a function of bulk glucose concentration. The input parameters that were varied were the number of GOx layers, which determines the total mass of enzyme in the films, and the number and composition of the remaining layers. As an initial starting architecture the following parameters were chosen. Cylindrical coordinates were used to simulate a 200 μm optical fiber for the template and the film consisted of $\{PAH/PSS\}_3$ + $\{PAH-488/PSS\}_{11}$ +$\{Ru(dpp)\}$ + $\{PEI/GOx\}_5$, as seen in Figure 18.
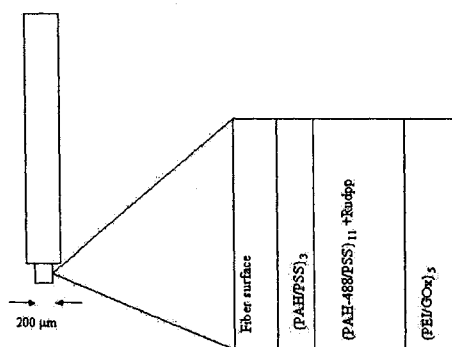
Figure 18. Illustration of the template and film architecture used in the functionality model.

The output of the model is shown in Figure 19. It can be seen from the figure that the oxygen concentration in the layers containing the Ru(dpp) changes by only 0.015% over 0 to 50 mM glucose. This trend indicates that there would be no measurable change in peak ratio because the there would be no change in the intensity of the Ru(dpp) emission peak due to insignificant oxygen consumption.
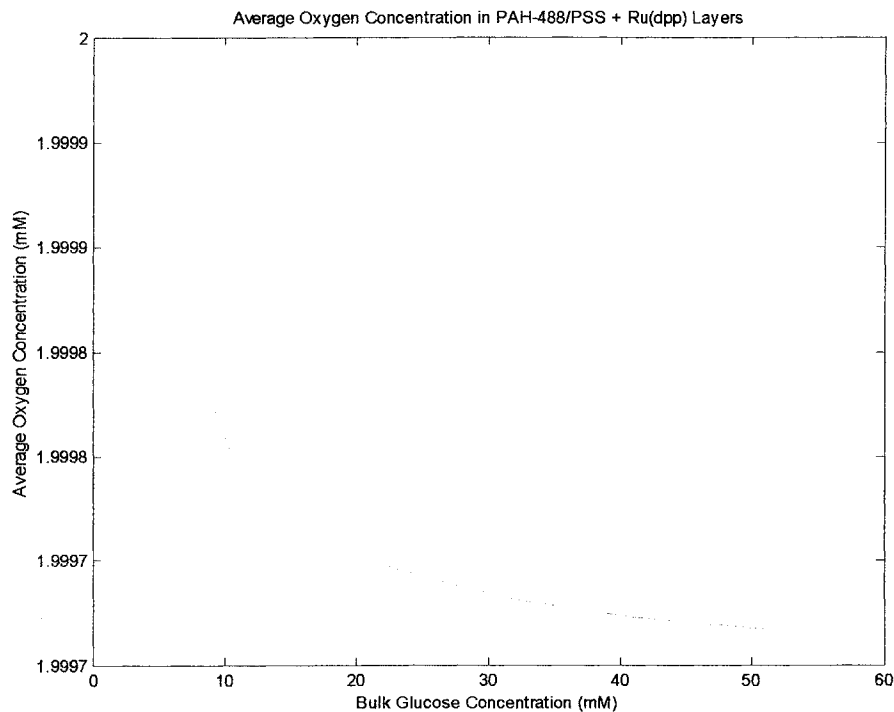
Figure 19. Average oxygen concentration is the sensing region for increasing glucose concentration.

The first varied parameter was the concentration of the enzyme in the film, to ensure the enzyme was not saturated. The enzyme concentration was increased by two orders of magnitude, which is 100-fold greater than the upper glucose concentration. Figure 20 shows, again, only a negligible (0.225%) change in the oxygen concentration with a 0 to 50 mM change in glucose concentration. Therefore, increasing the concentration of enzyme does not appear to have an effect on the sensor performance.
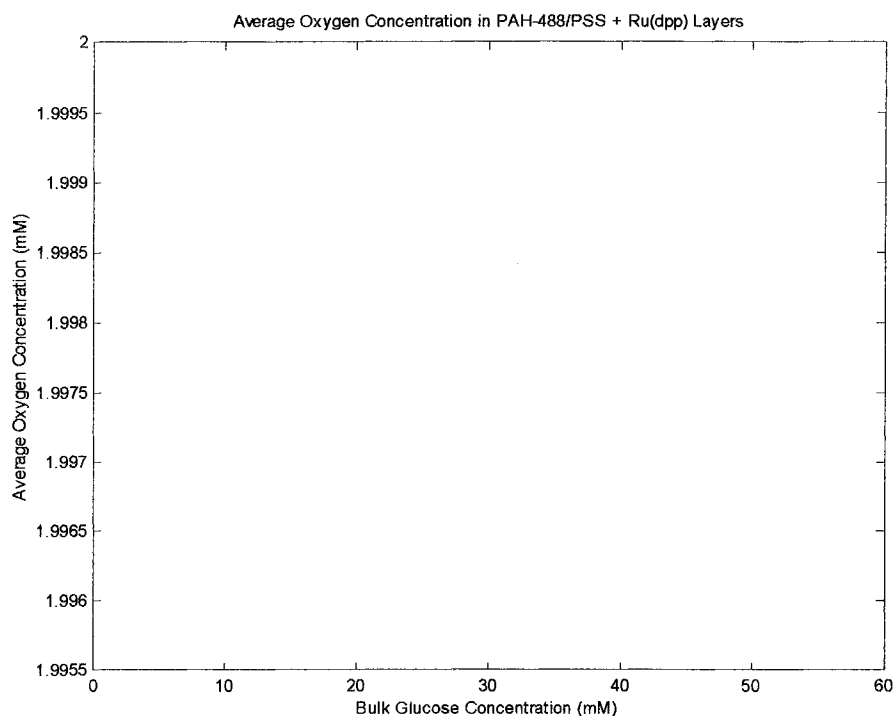
Figure 20. Average oxygen concentration is the sensing region for increasing glucose concentration with 500 mM GOx concentration in the films.

The diffusion coefficients of glucose and oxygen were then varied separately, in order to evaluate which variable had a greater contribution to the change in oxygen concentration in the sensing region. The basis of this variation was that, although ultra-thin films are advantageous in allowing fast diffusion of substrates and thus, fast response times, the diffusion of the substrate may be too fast for the oxygen sensor to transduce the changes in oxygen due to the enzymatic reaction. In Figure 21 and Figure 22, results of simulations where the diffusion of glucose was reduced by one and two orders of magnitude are presented.
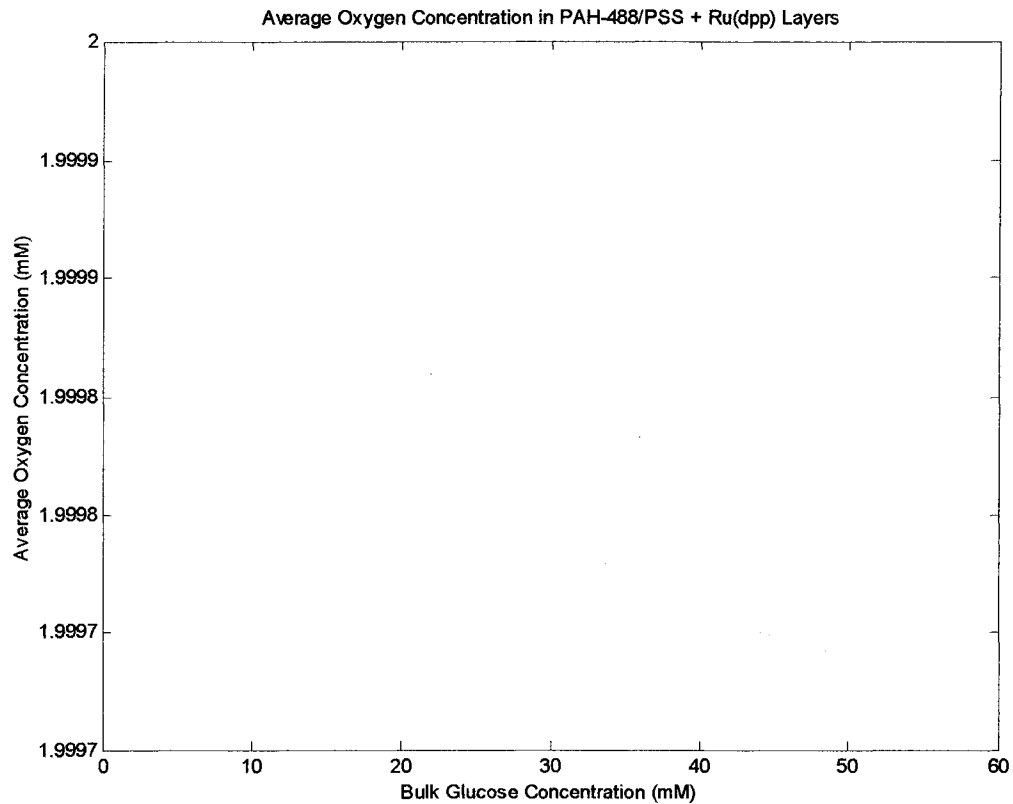
Figure 21. Average oxygen concentration is the sensing region for increasing glucose concentration with the diffusion of glucose reduced by one order of magnitude $(D_g=9.87e-15 \text{ m}^2 \text{ sec}^{-1})$.

Average Oxygen Concentration in PAH-488/PSS + Ru(dpp) Layers

[Plot with y-axis "Average Oxygen Concentration (mM)" (tick labels shown as 2) and x-axis "Bulk Glucose Concentration (mM)" from 0 to 60]
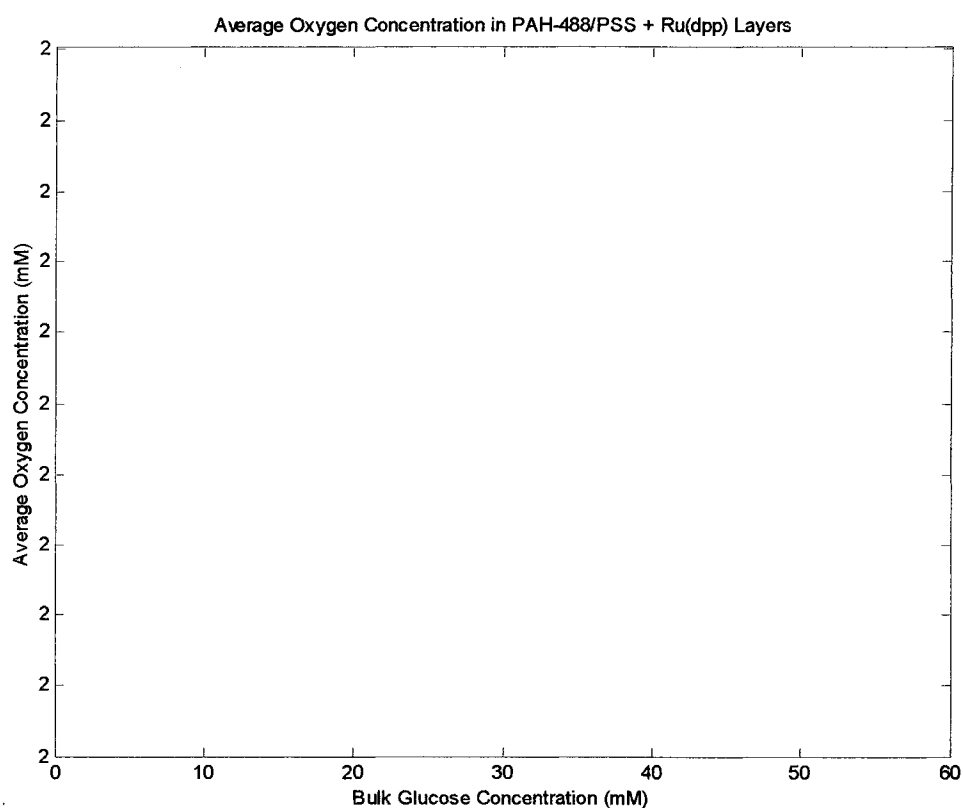
Figure 22. Average oxygen concentration is the sensing region for increasing glucose concentration with the diffusion of glucose reduced by two orders of magnitude $(D_g=9.87e-16 \ m^2 \ sec^{-1})$.

It is seen in the figures that the oxygen concentration in the sensing regions still changes less than 0.125% for one order reduction and no change for the two-order reduction in glucose diffusivity. This trend suggests that the diffusion of glucose is not the critical factor in the lack of change in oxygen concentration within the sensing layers.

The diffusion coefficient of oxygen was then reduced by one, two and three orders of magnitude and the results are seen in Figure 23, Figure 24 and Figure 25.
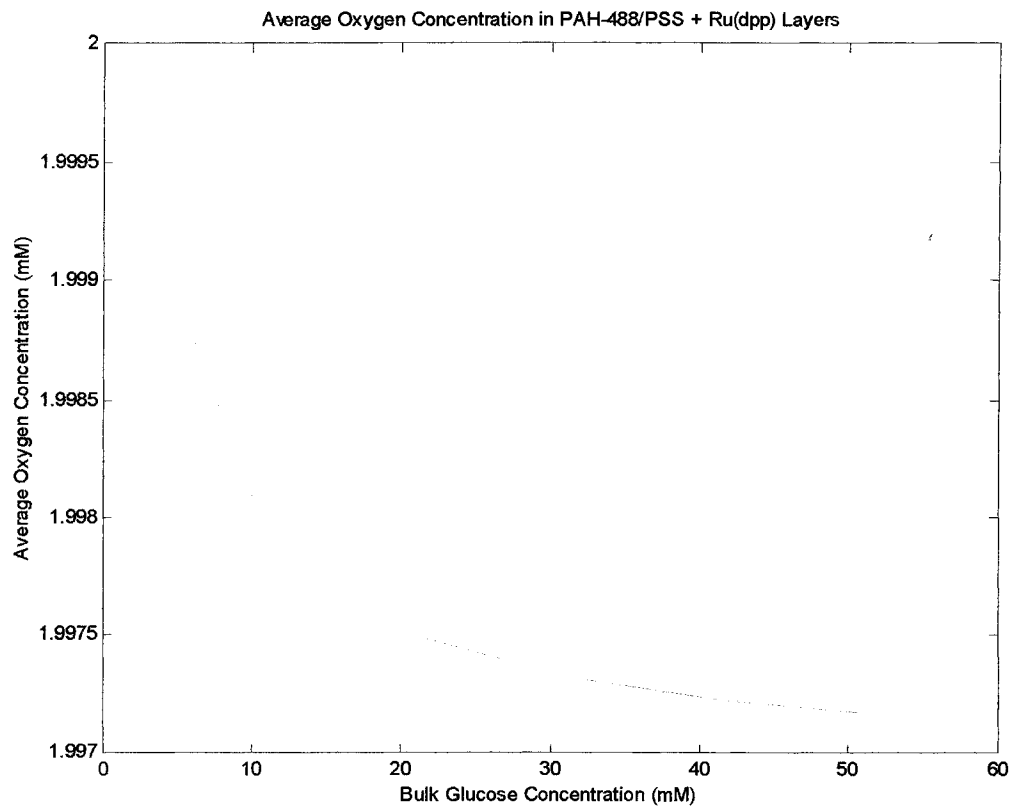
Figure 23. Average oxygen concentration is the sensing region for increasing glucose concentration with the diffusion of oxygen reduced by one order of magnitude $(D_O=9.87e\text{-}10 \text{ m}^2 \text{ sec}^{-1})$.

Average Oxygen Concentration in PAH-488/PSS + Ru(dpp) Layers
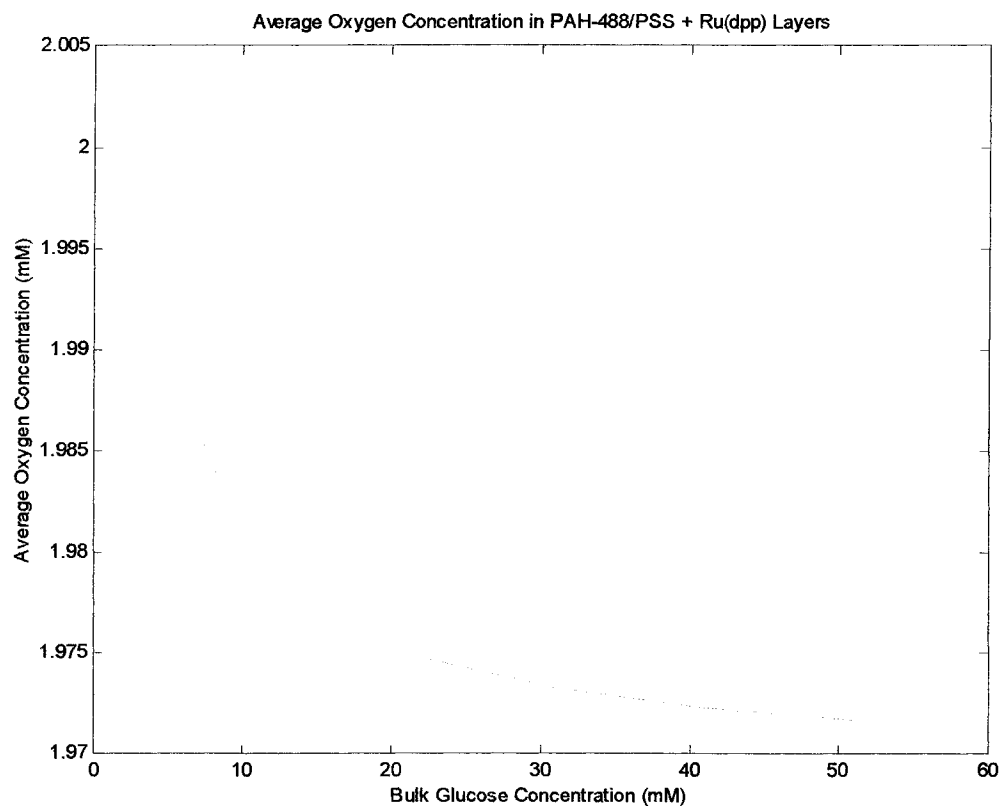
Figure 24. Average oxygen concentration is the sensing region for increasing glucose concentration with the diffusion of oxygen reduced by two orders of magnitude $(D_O=9.87e-11 \ m^2 \ sec^{-1})$.

Average Oxygen Concentration in PAH-488/PSS + Ru(dpp) Layers
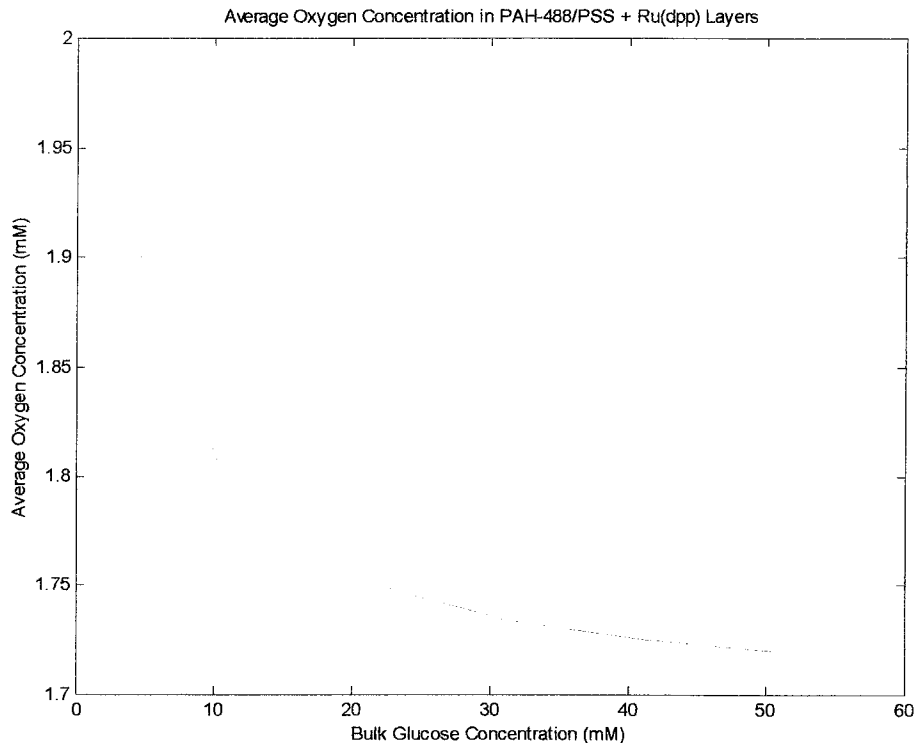
Figure 25. Average oxygen concentration is the sensing region for increasing glucose concentration with the diffusion of oxygen reduced by three orders of magnitude $(D_O=9.87e-12 \text{ m}^2 \text{ sec}^{-1})$.

Reducing the diffusion of oxygen in the film by one, two, and three orders of magnitude causes a 0.4%, 0.45% and 14% depletion of oxygen within the sensing layers. The sensing system is designed to be diffusion limited, not reaction limited, yet if the oxygen concentration in the sensing layers is replaced by diffusing oxygen nearly instantaneously, then the oxygen sensitive Ru(dpp) will be unable to transduce the oxygen concentration. Although it is important to remain in the diffusion-limited regime for accurate measurements, no measure will be accurate if the sensor does not respond to changes in glucose concentrations.

The physical consequence of these results is that the diffusion coefficient of oxygen must be reduced to a maximum of 10^{-12} m^2 cm^{-1} in order to achieve a 10% change in oxygen concentration in the sensing region over 0 to 50 mM glucose. To achieve this reduction in oxygen diffusivity, either a new material must be employed, the diffusion length must be increased, or both. The common polyelectrolytes that are used in LbL assembly are not going to change the diffusion coefficient by the three or more orders of magnitude required to measure a change in oxygen concentration according to the model. There are some polymers used in food packaging that have diffusion coefficients closer to what is required, [133] but they have yet to be characterized for LbL assembly.

Increasing the diffusion length is an option for the future, but because LbL assembly generally is used to form films with thicknesses of 1 to 10 nm per layer, it would not be best suited for the required increase in thickness. Dip-coating the fiber tip with PDMS, to create an architecture illustrated in Figure 10, was chosen as an easy method to verify the model results because it was readily available and simple to prepare. PDMS is not an ideal choice because it has an oxygen diffusion coefficient is on the order of 10^{-9} m^2 cm^{-1}. However, the ability to apply coatings to the fiber probe tip on the order of 10 to 100 μm provides sufficient transport barrier by increases the diffusion length for oxygen. The model was adapted to account for different thicknesses of the PDMS coating, and the results of similarities are given in Figure 26.
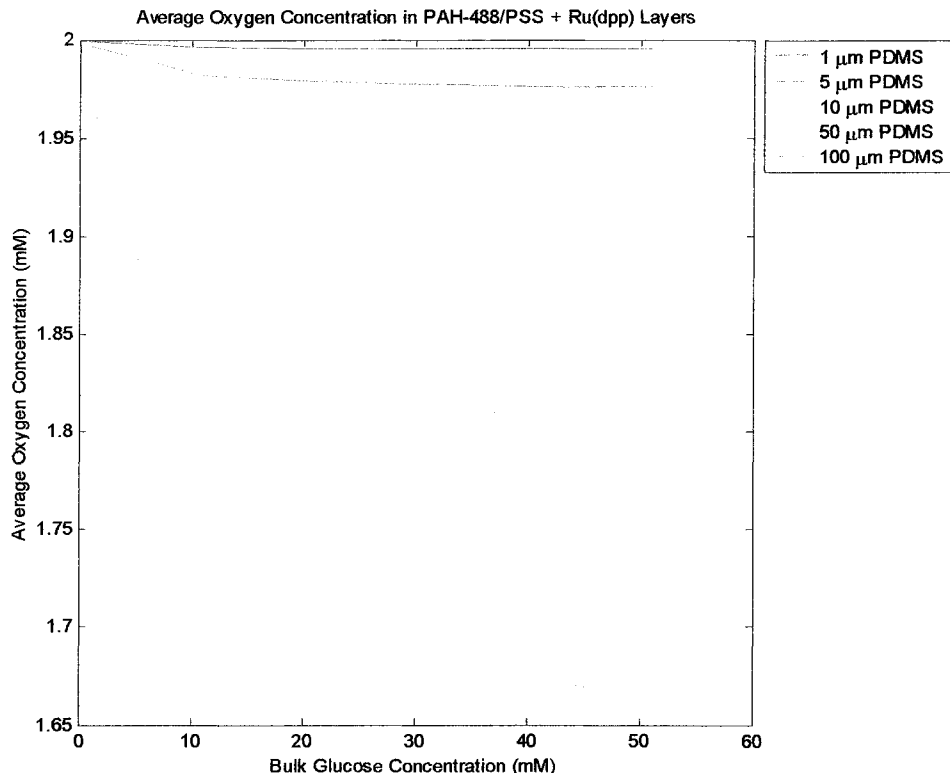
Figure 26. The average oxygen concentration in the sensing region for increasing glucose concentrations for probes with 1μm to 100 μm thick PDMS coatings.

The affect of the PDMS coatings is clearly seen by the predicted reduction in the oxygen concentration as the glucose concentration increases. The results demonstrate the need to reduce the diffusion of oxygen, but PDMS is a poor choice in that a 100 μm thick coating is required to generate a 20% change in oxygen concentration over the 0 to 50 mM glucose concentration range. Still, these results point to a physical situation that could be realized easily using LbL fiber probes modified with PDMS by dip coating.

An understanding of physical, chemical, and optical properties of the sensor components discussed in this chapter serves as a tool that allows the prediction and

comparison of experimental results. In this chapter, the fabrication, infusion, and functionality models provide not only a guide in the design of sensor, but also allow variations in the design parameters that would be time-consuming if one tried to evaluate many combinations experimentally. The optical properties of the tissue-light interaction designated limits on the number of particles that can efficiently be excited with a specific fiber choice. This information, combined with the infusion model, was used to directly determine the optimal time of infusion for a given concentration of sensors. The physical properties of the film architecture provide the necessary boundary conditions necessary to use with the functionality model, which is used to estimate the change in oxygen concentration is the sensing region. The estimated change in oxygen concentration was used with the fabrication model to estimate the number of fluorophore layers necessary to achieve an acceptable SNR. The experimental results given in chapter 5 will be related and compared to the findings in this chapter.

CHAPTER 4

MATERIALS AND METHODS

This chapter covers the materials and methods used to develop and test glucose sensors using the LbL assembly method. The chemicals and reagents are described, as well as the various instrumentation used in analyzing and characterizing the fabrication and testing of the sensor components. The development of glucose sensors was achieved by developing the processes for fabrication for each of the components of the sensing scheme. Specifically, the deposition of three different oxygen sensitive fluorophores, as well as two separate fluorophores for use as internal references, was developed on planar, fiber-optic and colloidal micro- and nano-templates. The response to oxygen was then investigated to evaluate the ability to measure oxygen changes using fluorescence of the ultrathin film components. The procedures of enzyme deposition were confirmed, as established previously in the literature and discussed in Chapter 2. The delivery of particles to the targeted region of the rat brain was developed using an agarose gel as a brain phantom. Last, the process of fabricating and testing of the glucose fiber probe is described, followed by a description of the data analysis employed.

68

4.1 General Chemicals and Reagents

All chemicals were purchased from Sigma Aldrich and Molecular Probes.

Specific details such as chemical name, product numbers, concentrations, and usage are

given in the following sections when explicitly describing experimental procedures.

4.2 Instrumentation

Absorption measurements were performed on a Hewlett-Packard 8453 UV-Vis

spectrometer. Fluorescence measurements were collected on a Photon Technology

International (PTI) QM-1 scanning fluorescence spectrometer and an Ocean Optics fiber-

coupled mini-spectrometer (USB2000). When using the fiber-optic spectrometer,

excitation of the fluorophores was achieved using an Oriel 68811 power supply running

an Oriel 66011 Arc Lamp with a 460 nm bandpass filter or by an Ocean Optics 450 nm

LED (USB-450-LS). The LED source was used in conjunction with optical fiber

templates while the are lamp was used in conjunction with nanoparticle templates.

Optical fibers (200, FT-200-URT, 400 μm, FT-400-URT and 100 μm) were purchased

from Thorlabs to fabricate a six around one fiber, all 400 μm, a two (200 μm) to one (400

μm) "Y" type fiber and a similar fiber using two (100 μm) and one (400 μm) fiber. The

six-around-one fiber probe was used to deliver excitation light from the Ocean Optics

USB-450-LS via the single fiber, while the remaining six were connected to the Ocean

Optics USB2000 spectrometer.[134] Sonication was performed with a Branson 1510

ultrasonic cleaner. Quartz crystal microbalance (QCM) studies were performed with USI

SC-7201 frequency counter. Resonators (gold, 0.16 cm^2/side) were purchased from

Sanwa Tsusho. Custom quartz slides (9.0 x 25.1 x 1 mm) were purchased from Quartz

Plus, Inc. Quartz spectrophotometer cells were purchased from NSG Precision, Inc.

Oxygen measurements were collected on a PC running LABVIEW using a DAQ card

connected to a Unisense PA2000 picoammeter with an OX500 micro-oxygen electrode.

Tissue sectioning was performed using a Tissue-Tek® Cyro$_3$® cryostat. Fluorescent

confocal images of tissue sections were captured using a Leica TCS SP2 laser scanning

fluorescence confocal microscope. Histological analysis was performed using a Nikon

fluorescence microscope.

4.3 Experimental Procedures

4.3.1 Nanoassembly to Produce Oxygen Sensors

QCM measurements were used to monitor the layer growth of Ru(bpy)$_3{}^{2+}$

(tris(2,2'-bipyridyl)dichloro-ruthenium(II) hexahydrate (Ru(bpy)$_3$Cl$_2$), 1.2 mg/mL in pH

7.6 buffer). Ru(bpy)$_3{}^{2+}$ was alternated with poly(sodium styrenesulfonate) (PSS 2

mg/mL; MW 1,000,000) and frequency measurement was performed after each layer. A

total of 5 bilayers, {Ru(bpy)$_3{}^{2+}$/PSS}$_5$, were deposited on both the QCM resonator and

quartz slide. Quartz slides were prepared for layering by sonicating for 20 minutes at

50°C in a solution of 1% KOH, 60% ethanol, and 39% water. Slide layering was

performed by alternately dipping in solutions of Ru(bpy)$_3^{2+}$ and PSS, and absorption spectra were collected after each layer.

The assembly of Ru(bpy)$_3^{2+}$ was also investigated by premixing the dye with a polyanion, PSS (2 mg/mL) at pH 7.6. Three different concentrations were used in the assembly process, 0.29 mg/mL, 0.57 mg/mL and 1.14 mg/mL Ru(bpy)$_3^{2+}$. For each concentration a total of 5 bilayers, {Ru(bpy)$_3^{2+}$:PSS/PAH}$_5$ were deposited on both the QCM resonator and quartz slide. In each case the premixed complex Ru(bpy)$_3^{2+}$:PSS was alternated with PAH, (2 mg/mL; MW 15,000.) Film growth was monitored by both QCM and UV-Vis, as noted above.

PAH was conjugated with the following fluorophores; Ru(bpy)2(mcbpy) (MW 1014.67), FITC (MW 389.4). The layer growth was monitored by QCM measurements, as well as absorbance and fluorescence spectra collected from quartz slides. For each labeled PAH-dye complex a total of 5 bilayers, {PAH-dye/PSS}$_5$ were deposited on both the QCM resonator and quartz slide.

Labeled polyelectrolytes were then assembled on optical fibers and polymer colloids. First an optical fiber (400 μm) was prepared for layering by removing the buffer coating, cleaving the bare end, then soaking the exposed end in acetone for 1 min to remove a small length of cladding. Finally, the same assembly procedure used for the quartz slides was applied to the fiber, with a final architecture of {PAH-Ru(bpy)2(mcbpy)/PSS}$_{10}$ + {PAH-FITC/PSS}$_5$. Fluorescence measurements using a Y patch cable to collect spectra from the illuminated tip were made after each bilayer to track the growth of the films.

Polystyrene microparticles, 520 nm and 301 nm diameter, were chosen as templates for fabrication because they provide a negatively charged surface without further modification and are inexpensive. The assembly process on particles was carried out in the following manner: (1) PS particles having a negative surface were suspended in a solution of PAH-FITC or PAH-488 solution for 10 min to allow adsorption to occur; (2) the particles were centrifuged at 12,000 rpm for 10 min, after which the supernatant is removed by pipette; (3) the particles were then re-suspended by vortex and ultra-sonication in a pH 7.6 buffer solution. This process was repeated two times to allow complete removal of any residual PAH-FITC or PAH-488. These three steps were then repeated, using PSS and PAH-Ru(bpy)2(mcbpy) as adsorbate. Assembly was monitored using measurements of zeta potential and fluorescence. Zeta potential, an average of ten measurements, was measured to monitor the reversal of the surface charge. Secondly, a fluorescence spectrum was collected after each layer to monitor the relative increase of the peak wavelengths for the sensor dyes.

A method for loading Ru(dpp) into polyelectrolyte films has been developed[135] and was utilized to fabricate oxygen sensors on both fiber probes and polystyrene particles. This ruthenium compound has a larger Stern-Volmer constant and, thus, is more sensitive to oxygen.[128] The water-insoluble Ru(dpp), was prepared in solution by dissolving 1 mg Ru(dpp) in 4.55 mL of DI water, 0.2 mL of NaOH(10 mg/mL in DI), and 2.75 mL MeOH. This procedure was developed by tritration to find the minimum MeOH concentration needed to dissolve the Ru(dpp). Particles with 1 bilayer {PAH/PSS}$_1$ and 10 bilayers {PAH-488/PSS}$_{10}$ are then suspended in the Ru(dpp) (0.133 mg/mL) solution

and left for 1 hour to allow the Ru(dpp) molecules to penetrate the polyelectrolyte films.

The Ru(dpp) molecules are "loaded" into the films by pairing with uncompensated

charge sites of the polyelectrolytes and via partitioning of the poorly water-soluble

molecules into the film. The particle suspension is then centrifuged and the supernatant

are removed and the particles are then subjected to three rinse cycles. Figure 27

illustrates the assembly and loading procedure. Films were assembled on 301 nm

particles as described above and the loading method was used to immobilize Ru(dpp).

The fiber probes were assembled using the same method, except the fiber tip was

immersed in the dye solution and subsequently immersed in DI water for rinsing. The

illustration in Figure 27 is still valid in describing the fiber probe fabrication, if one

considers the orange circles to be a cross-section of an optical fiber.

Figure 27. Illustration of the assembly and loading of films with the architecture {PAH-488/PSS} + Ru(dpp).

4.3.2 Testing of Oxygen Sensors

Experiments to characterize the oxygen response of the fluorescent thin films

were carried out to verify that the films did not hinder the ability of the ruthenium

compounds to be quenched by molecular oxygen, as well as to determine the Stern-Volmer constant. The ultra-thin films were not expected to present a transport barrier to oxygen and this was verified in Figure 19 in Chapter 3. The determination of the Stern-Volmer quenching constant was needed to predict the change in peak ratio due to the predicted oxygen concentration in sensing regions, which was determined from the coupled reaction-diffusion model discussed in chapter 3.

A quartz slide was placed in a cuvette holder where fluorescence intensities at 605 nm and 525 nm, were monitored over time while a stream of oxygen was applied at approximately 0.5, 1, and 2 min. The layered fiber-optic probe was tested for oxygen sensitivity following deposition of {PAH-Ru(bpy)2(mcbpy)/PSS}$_{10}$ + {PAH-FITC/PSS)$_5$, by placing the tip of the fiber in a cuvette containing 3 ml of buffered solution along with a micro-oxygen electrode. The opposite fiber end was coupled through the "Y" type connector to the light source and spectrometer. During data collection, nitrogen and oxygen were alternately bubbled into the cuvette via 1/16th inch tubing. A time-based scan, monitoring the intensities at 524 nm and 630 nm, was performed while simultaneously recording oxygen content values.

For the particle-based sensors, excitation light from the Oriel 66011 Arc Lamp fitted with a 460 nm bandpass filter was delivered 90° to the collection probe containing six fibers connected to the Ocean Optics USB2000 spectrometer. A 1/16th inch tube was placed in the top of the cuvette penetrating the surface of the suspension, but above the path of the excitation beam, from which nitrogen and oxygen were bubbled in separately at times as indicated. The particles with {PAH-FITC/PSS}$_1$+{PAH-Ru(bpy)2(mcbpy)/-

PSS}$_2$ architecture were placed in a cuvette, suspended in a buffered solution and time-based fluorescence measurements of the intensities at 617 and 516 nm were collected.

Fiber probes with the architecture {PEI/PSS}$_3$ + {PAH-488/PSS}$_{11}$ + Ru(dpp) were fabricated and sensitivity was evaluated using a Y patch cable to collect spectra from the illuminated tip.

4.3.5 Nanoparticle Delivery

Successful application of the nanoparticle sensors for neural glucose sensing requires successful delivery of the nanoparticles to the targeted area of the rat brain. Development of a protocol was needed due to the lack of information in the literature are such techniques. The delivery of the sensors to the rat brain was investigated by developing a brain phantom that simulates the rat brain mechanically and structurally. Previous research[120] had determined that 0.2% agarose gel is a sufficient phantom. The brain phantoms were made as follows; measure 50mL of Tris Buffer with a pH of 7.6. Heat and stir the buffer until a temperature of 50°C is reached. Add 0.1g of agarose powder and continue to stir and heat mixture until a temperature of 85°C is achieved. Remove the mixture from the heat source and let it cool to 60°C. The mixture can then be poured into the desired mold, such as a 2-inch diameter Petri dish.

The following setup was used to infuse 301 nm polystyrene particles into the phantom and collect spectra from the particles. The basic setup consists of a syringe pump, a stage for the phantom, and a spectrometer. A microdialysis infusion pump (CMA/102) was used to pump the particles into the phantom.
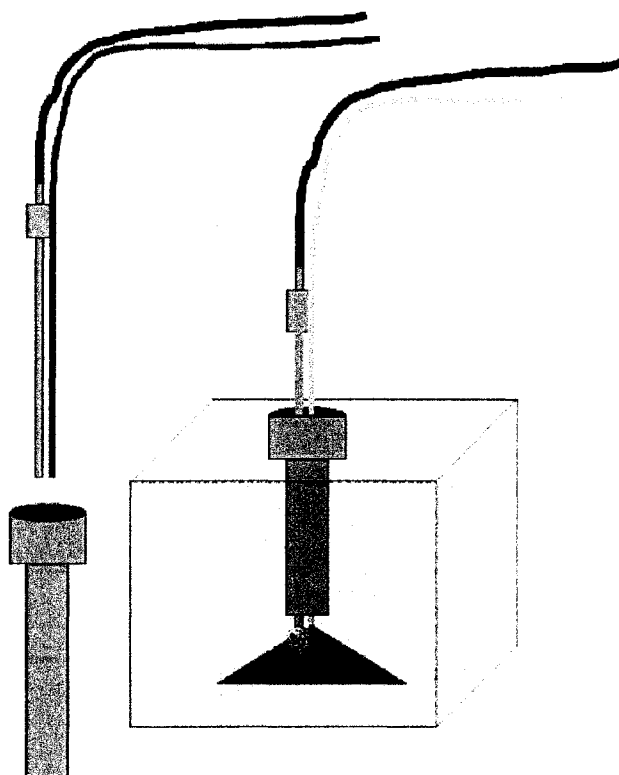
Figure 28. Illustration of the experimental setup used for both the *in vitro* and *in vivo* delivery of particles.

This infusion pump has a range of flow rates between $0.1\mu L/min$ and $20\mu L/min$.

The pump holds a syringe with a volume of 1mL. The syringe was connected to a 26

gauge infusion cannula guide by a tube with a diameter of 0.58 mm. A 200 μm optical

fiber probe connected to a "Y" type connector containing two 200 μm fibers was used in

conjunction with the USB2000 spectrometer in order to collect spectra from the particles

in the phantom during the infusion process. The infusion cannula and fiber probe were

placed into a 1.2 mm cannula guide that was placed in the 0.2% agarose brain phantom,

as seen in Figure 28, or implanted in the rat brain. The protocol, described below, for

animal experiments was approved by the IRB and performed at the University of

Louisiana at Monroe, under the guidance of Dr. Karen Briski.

Adult male Sprague Dawley rats (220-240g) were purchased from Charles River, Inc., (Wilmington, DE), and maintained in the College of Pharmacy Vivarium located on the fourth floor of Sugar Hall at ULM. The animals were housed in group cages (3-4 rats/cage) under a 14 hr light:10 hr dark schedule (lights on at 0500), and allowed free access to standard rat chow and water. The rats were handled and weighed daily to facilitate acclimation. A solution containing 1:9 (vol) ketamine: xylazine was prepared prior to surgery and sterilized in a disposable filtration unit. The anesthetic was administered intraperitoneally at a dose of 1 mL/kg. The anesthetized animal was placed on a plastic surgical platform to avoid contact with the surgical area. After surgery, the animal was monitored every 30 min until recovery is noted.

Shaved skin at the surgical site was scrubbed with Betadine, followed by 70% ethanol; in accordance with IACUC guidelines for survival rodent surgery, this sequence was repeated three times and the skin finally painted with Betadine. The animal was then covered with an autoclaved drape fashioned from surgical garment cloth to expose the surgical site. Four to five animals underwent surgery during a single session; the surgical instruments were soaked in disinfectant (Amerse) between subjects, then rinsed with sterilized distilled water.

The anesthetized animal was mounted into a Stoelting stereotaxic apparatus. An anteroposterior incision of the skin covering the dorsum of the skull was made to expose *bregma*, and three dimensional coordinates from the Paxinos and Watson rat brain atlas was used to locate the target site (dentate gyrus of the hippocampus) for the stainless steel external cannula guide (Plastics One, Inc., Roanoke, VA). A small hole was drilled

through the skull at the marked site, and the cannula guide lowered to an appropriate depth. It was secured in place using metal screws and dental cement. When the cement was dry, the area was sprinkled with penicillin G powder, and the wound closed with autoclaved wound clips. A solid obturator with screw cap was inserted into the external guide to seal it and ensure patency. Dr. Briski's personal observations of animals treated as described above have consistently revealed no significant changes in behavior (feeding, drinking, elimination), posture, or mobility that would indicate persistent pain or discomfort.

Ten days after surgery, the infusion cannula was inserted into the cannula guide. Before implantation, the perfusate was loaded into clean microsyringes before these were attached to a microsyringe pump. The obturator was removed from each cannula guide, and the infusion cannula was inserted into the neural target site. Along with the infusion cannula, an optical fiber was inserted to monitor the delivery process in real-time. Optical spectra were recorded every 4 μL of infusion and normalized fluorescence intensity plotted as a function of time, allowing determination of delivery time profile. Following an equilibration period of approximately 15 mins, the suspension of nanosensors were delivered via the perfusate. After a delivery volume of 32 μL, the perfusion was stopped and the probe kept in place for an additional 10 min to prevent reflux of tissue fluid into the cannula guide. Animals were sacrificed 1 week later by transcardial perfusion with saline, followed by paraformaldehyde in phosphate buffer, and brain tissue collected for histological analysis of extent of diffusion of nanosensors from site of administration.

Each brain was postfixed overnight in fresh fixative, sunk in 25% sucrose, and cut

into 10 μm sections on a Tissue-Tek® Cyro₃® cryostat. Sections through the target site

were stained with methylene blue, mounted on gelatin-coated slide, dried, and then

dehydrate in graded alcohols, cleared, and coverslipped. The tissues were examined with

a Nikon brightfield photomicroscope to determine correctness of probe placement and

confinement of nanosensor delivery to the intended structure. Samples were analyzed to

confirm appropriate sensor localization at the targeted site, and local tissue damage will

be assessed to determine inflammation or other response to the introduction of a foreign

body.

4.3.6 Biocompatibility

Assessment of biocompatibility was performed using rat models and was carried

out using the protocol described in Section 4.3.5. The study consisted of 12 rats in which

particles with the following architecture were infused: $(PAH/PSS)_1$, $(PAH-FITC/PSS)_1$,

$(PAH-Ru(bpy)2(mcbpy)/PSS)_1$, and $(PAH-FITC/PSS)_1+(PAH-Ru(bpy)2(mcbpy)/PSS)_1 +$

$(PEI/GOx)_1$ Controls used to compare results, included no infusion, infusion of pH 7.6

0.2 M Tris buffer, and infusion of PS particles with no coatings. Infusions were carried

out using flow rates of 0.3 μL/min for 10 min. The rats were then sacrificed at weeks 1,

2, and 4. The procedures for sacrificing, brain tissue collection, tissue sectioning, and

analysis were described in Chapter 4.3.5.

4.3.7 Glucose Sensor Fabrication and Testing

A 200 μm diameter optical fiber was used as the template to fabricate a glucose sensor. This size fiber was chosen for future work, in which the fiber probe will be introduced to the targeted brain tissue via a 280 μm cannula guide. Films with the architecture {PAH/PSS}$_3$ + {PAH-488/PSS}$_{11}$ +Ru(dpp) + {GOx/PEI}$_5$ were dip-coated with PDMS and allowed to cure for 24 hours. The PDMS coating serves to reduce the diffusion of oxygen, although the diffusion of glucose is reduced as well. The thickness of the PDMS coating was approximately 100 μm, as estimated from observations made with optical microscope.

The testing of the glucose sensor was performed by placing the tip of the fiber probe in a cuvette, which was filled with solutions of different glucose concentrations. Fluorescence spectra were collected at intervals of 12 secs, in addition, time based scans of the intensities were collected for the source reflectance peak (470 nm), the Alexa Fluor 488® peak (520 nm), the Ru(dpp) peak (615 nm), and the peak ratio of the Ru(dpp) to Alexa Fluor 488®. The acquisition was paused during the exchange of fluid, with two rinse cycles of DI water in between solutions containing glucose. The glucose solutions were introduced to the cuvette in steps of 200 mg/mL.

Following the analysis of the glucose sensing experiment it was observed that there was drift in the peak ratio over 0 to 600 mg/dL glucose. When exposed to excitation light, fluorophores will photobleach, causing a linearly decrease in fluorescence emission with time of exposure. In examination of the data, it was

determined that the apparent photobleaching rate was changing from negative to positive during exposure to solutions of glucose. The enzymatic reaction of GOx in the films produces gluconic acid, possibly lowering the local pH. To study the possible effects of pH on the spectral behavior, a series of experiments were perform. The fiber probe, used in the glucose sensing experiment was placed in a cuvette containing DI water at pH levels, 3.5, 6.05 and 10.28. The spectrum of the sensor was monitored over time in each of the three cases.

4.3.8 Summary of Methods and Materials

In summary, three ruthenium compounds were investigated for use in the sensing films. Quartz slides were initially chosen to investigate the assembly of the fluorophores, including the direct assembly of $Ru(bpy)_3^{2+}$, the premixing of $Ru(bpy)_3^{2+}$ with PSS, as well as the conjugation of Ru(bpy)2(mcbpy) to PAH. The assembly process was then elaborated on optical fibers using the PAH- Ru(bpy)2(mcbpy). The oxygen sensing ability of the films on both quartz slides, optical fibers and nanoparticles were examined using fluorescence spectroscopy. An assembly method using Ru(dpp) compound was then developed for assembly on optical fibers and nanoparticles. In all case, the internal reference was deposited by conjugating either FITC or Alexa Fluor 488[®] to PAH.

The delivery of nanoparticles was developed using agarose gels as a brain phantom and the parameters such as infusion rate and particle concentration in the infusate were identified. An experimental setup was designed to allow the monitoring of the infusion process by fluorescence spectroscopy to allow the *in vitro* and *in vivo*

experiments to be compared to the infusion model. Using the functionality model as a guide, glucose fiber probe was fabricated with PDMS coating to reduce the diffusion of oxygen. The fiber probe placed in a cuvette and was tested by introducing glucose solutions to the cuvette. The results of the preceding methods are presented and discussed fully in the next chapter.

CHAPTER 5

RESULTS AND DISCUSSION

This chapter contains a description of results obtained over the past three and a half years detailing the development of a glucose sensor for neural monitoring. The chapter is divided into sections describing the results of investigations on the methods of assembly and testing of fluorescent ultrathin films deposited on planar, optical fibers and nanoparticles. In developing the glucose sensors, the oxygen sensing capabilities of the probes were characterized in terms of the Stern-Volmer equation and related to the model in Chapter 3 describing the predicted enzymatic function of the enzyme films.

The results of the delivery methods of the nanoparticle sensors is described for both *in vitro* and *in vivo* cases, which include monitoring of the fluorescent spectrum of the sensors during the infusion, as well as verification of delivery in the *in vivo* case by fluorescence confocal microscopy. The results of the biocompatibility of the sensor components are presented in terms of histological analysis from optical microscopy of stained tissue samples of brain sections. The infusion experiments are also compared and related to the infusion model developed in Chapter 3.

Lastly, the results of testing a glucose-sensitive fiber probe are presented to demonstrate a response to glucose that matches the theoretical predictions. The results are related specifically to the models developed in Chapter 3, which were used in the sensor design. Examination of sensor performance led to an experiment designed to examines the effect of pH on the response of the sensor, specifically the apparent change in photobleaching rate due to changes in pH.

5.1 Dye/Polyion Assembly to Produce Oxygen Sensors

Direct LbL assembly of both absorbing and fluorescent dyes, alternated with polyions or polypeptides, has been shown previously[16,20-22]. Therefore, the first method assessed for incorporating fluorophores in thin films was that of direct LbL assembly, monitored by QCM. In this method, $Ru(bpy)_3^{2+}$ was alternated with PSS during the assembly process. As seen in Figure 29, after ten layers, the directly-assembled $Ru(bpy)_3^{2+}$ showed a frequency change of 206 Hz, approximately 1500 Hz less than the other assembly methods, indicating that no significant adsorption occurred. Previous work with dye-polyion films have shown multilayer assembly may be achieved, but with significant desorption of the dye, as much 60%, following polyion adsorption.[136] Dye desorption was shown to increase linearly with the number of bilayers.[137] The QCM values show no multilayer formation, indicating that, if the $Ru(bpy)_3^{2+}$ is adsorbing to the surface, it is too weakly charged to reverse the surface charge and is subsequently extracted from the surface with the following PSS layer. QCM frequency measurement is stable for 1 to 2 hours, and the error in the measurement is only 2 or 3 Hz.
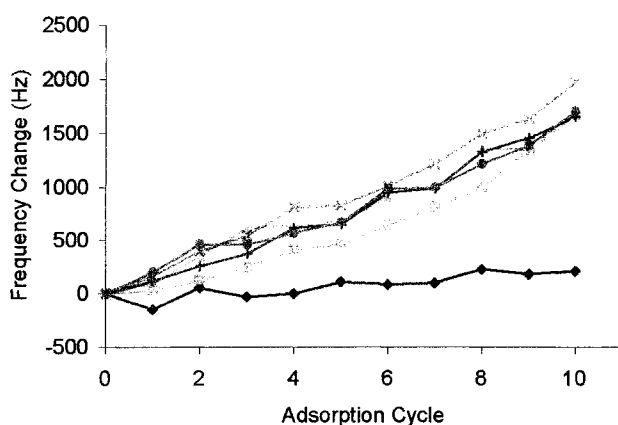
Figure 29. QCM measurements vs. adsorption cycle during the assembly of $Ru(bpy)_3^{2+}$ directly (diamonds), by $Ru(bpy)_3^{2+}$:PSS premixing (0.29 mg/mL, triangles; 0.57 mg/mL, x's; 1.14 mg/mL, +'s), and conjugation Ru(bpy)2(mcbpy) to PAH (solid circles) compared to PAH/PSS (squares.)

Thus, with frequency changes in steps of ~150 Hz for each assembly method

except direct assembly, the error is less than 3%. Absorbance measurements (Figure 29)

also show no observable increases in absorbance at 460 nm following direct assembly,

further supporting the hypothesis that no multilayer formation has occurred.

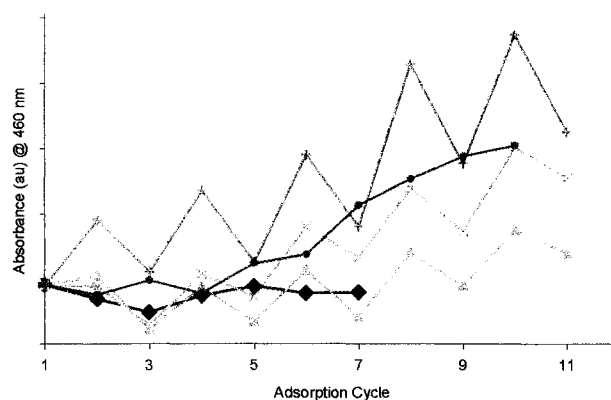Figure 30. UV-Vis absorbance measurements at 460 nm vs. adsorption cycle on quartz slide during the assembly of $Ru(bpy)_3^{2+}$ directly (diamonds), by $Ru(bpy)_3^{2+}$polyion premixing (0.29 mg/mL, triangles; 0.57 mg/mL, x's; 1.14 mg/mL, +'s), and conjugation of Ru(bpy)2(mcbpy) to PAH (solid circles).

Difficulties in assembling small MW charged dyes using LbL techniques have led to the development of a premixing method,[138,139] in which a dye and oppositely-charged polyion are mixed together in solution prior to assembly. Using this approach, $Ru(bpy)_3^{2+}$, was premixed with PSS ($Ru(bpy)_3^{2+}$:PSS) and alternated with PAH for assembly on both QCM resonators and quartz slides. QCM measurements, as given in Figure 29, show that the step of growth and overall multilayer thickness were similar for each of three different $Ru(bpy)_3^{2+}$ concentrations. A control experiment using only the polyions ($\{PAH/PSS\}_5$), also shown in Figure 29 yielded similar growth properties. This demonstrates that multilayer formation is dominated by adsorption of PAH and PSS, and the effect of small MW, weakly-charged $Ru(bpy)_3^{2+}$ is not evident in measurements of mass change.

Absorbance measurements (Figure 30) reveal that the $Ru(bpy)_3^{2+}$ was, in fact, incorporated into the films, showing regular increases in absorbance at 460 nm. As the concentration of the $Ru(bpy)_3^{2+}$ was increased in the premixed solution (2X and 4X), the observed maximum absorbance increased by factors of 3.40 and 4.85, indicating that increasing the amount of $Ru(bpy)_3^{2+}$ in solution will increase the amount of dye absorbed per layer. The figure also shows an oscillating pattern for each of the slides prepared with ($Ru(bpy)_3^{2+}$:PSS), clearly showing the process of desorption upon exposure to PAH. The amount of desorption increases by factors of 1.31 and 3.09 between adsorption cycle 9 and 10, respectively, with increasing concentration of $Ru(bpy)_3^{2+}$ in the premixed solution. This trend presents a problem for fluorescence sensor development: in order to fabricate a brighter sensor, either more layers or a higher concentration of fluorophores in

the dye:polyion premix are needed, both leading to increased desorption as additional layers are deposited.

To develop more stable fluorescent films, with little desorption of dye, covalent linkage of fluorophores to PAH was considered. Ru(bpy)2(mcbpy) was chosen to label PAH, and then the assembly was elaborated on QCM. The step of growth and overall layer thickness for 5 bilayers is similar to {PAH/PSS}$_5$, as seen in Figure 30, with a change of frequency of 1703 Hz for {PAH- Ru(bpy)2(mcbpy)/PSS}$_5$ and 1683 Hz for {PAH/PSS}$_5$. This obseravation indicates that the labeling procedure does not adversely affect the LbL assembly. Absorbance measurements were also collected to evaluate the amount of dye incorporated into the films using labeled PAH (Figure 30). The data show increases in absorbance at 460 nm, with no apparent desorption of the dye with the subsequent PSS adsorption. Since these data compare two different ruthenium compounds, the values were corrected for extinction coefficients in order to directly compare the absorbance measurements.

The data presented in Figure 29 and Figure 30 show the results of three fabrication techniques for depositing fluorophores in LbL films: direct assembly, premixing, and conjugation. In summary of the above statements, direct assembly with Ru(bpy)$_3{}^{2+}$ does not result in multilayer formation. Furthermore, while multilayer formation occurs with Ru(bpy)$_3{}^{2+}$:PSS premixing, the amount of dye desorption increases with increasing number of bilayers, which would eventually result in total removal of adsorbed dye and inability to form multilayers. In comparison, films comprising PAH-Ru(bpy)2(mcbpy) exhibit similar properties to PAH films.

LbL assembly provides the ability to control the number of molecules of multiple fluorophores contained in the films; therefore, one is able to control the optical properties during fabrication, by "building" the films in a process of successive deposition. This allows one to obtain a desired spectrum using a single excitation and allows tuning of the resulting emission spectra as well as the sensitivity and dynamic range of the films. The fluorescence spectra given in Figure 31 demonstrate that, when normalized to the fluorescence peak of the initial PAH-FITC, additional layers of PAH-Ru(bpy)2(mcbpy) increase with the number of layers deposited. The inset in Figure 31 shows fluorescence intensity and absorbance of PAH-Ru(bpy)2(mcbpy) films as a function of adsorption cycle. The step of growth was fairly constant for both absorbance and fluorescence, and additional layers do not cause a decrease in step of growth of the fluorescence, suggesting significant self-quenching is not occurring.
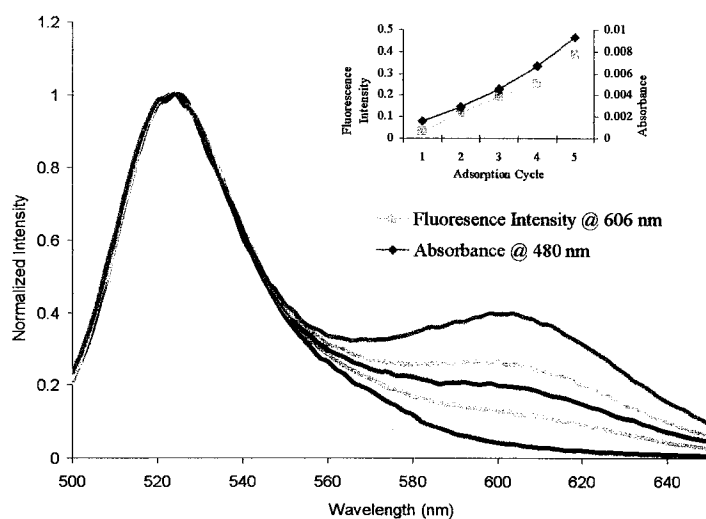
Figure 31. Fluorescence spectra of quartz slide with the following architecture: {PAH-FITC/PSS}2+(PAH-Ru(bpy)2(mcbpy)/PSS}4. A spectrum was collected after each Ru(bpy)2(mcbpy)/PSS}4 bilayer and were normalized to the FITC (520 nm) peak.

The assembly procedure was repeated to deposit the O_2-sensitive film on the

end of an optical fiber. A fluorescence spectrum was collected after deposition of each

bilayer during the LBL assembly of the fiber probe. As shown in Figure 32, the regular

growth demonstrates the ability to construct and tailor a spectrum with the desired

relative size of multiple fluorescence peaks. Encouragingly, the relative magnitude of the

Ru(bpy)2(mcbpy) and FITC peaks was identical for spectra collected from the optical

fiber and slides when the same number of layers of each material was deposited. This is

an important detail, as it supports the concept of rapidly prototyping sensors using

inexpensive substrates, then porting the same sensing film architecture to another

template.
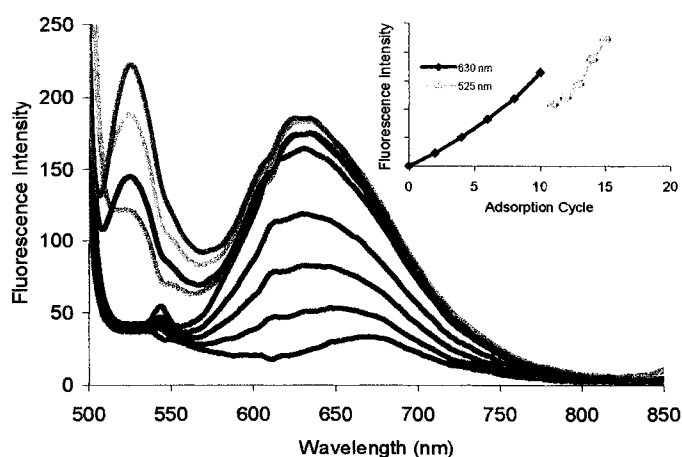
Figure 32. Growth of PAH-Ru(bpy)2(mcbpy) and PAH-FITC on a optical fiber with fluorescence spectra collected after the every other bilayer for the first 10 bilayers and after each bilayer for the remaining 5 bilayers.

After completion of the assembly on macro-templates, including both slides and

optical fibers, the same architecture was applied to microparticles, a more suitably sized

substrate for use in microscopy or as *in vivo* biochemical sensors. Zeta potential measurements (Figure 33) were made following three rinse cycles after adsorption of desired molecules to determine the surface charge of particles. It is clear from the figure that there was complete reversal of surface charge with each adsorption cycle, which corroborates the QCM assembly observations for the same films. Particles with outer surfaces of PAH-FITC and PAH-Ru(bpy)2(mcbpy) were measured to have different magnitude of positive surface charge. This result is due to different degrees of labeling, which would cause more or fewer charged sites to be occupied by fluorophores in each case. In both cases, however, the charge was sufficient to attract sufficient PSS to produce a negative charge approximately the same as that on the native polystyrene particle. It was also observed that fluorescence increases with the addition of each layer, as seen on both macro-templates. This observation suggests that each particle has, on average and for a given number of layers, the same relative amount of fluorophores deposited onto its surface. Thus, the LbL process allows fabrication of sensors that have a uniform average film composition and, thus, a uniform response. In addition, the fluorescence spectra showed relative peak sizes for Ru(bpy)2(mcbpy) and FITC emission that were the same as those observed from spectra collected from slides and optical fiber. Hence, the design and characterization of fluorescence sensors such as these can be carried out on macro-templates, which can be rapidly prototyped, then ported directly to micro/nanotemplates.
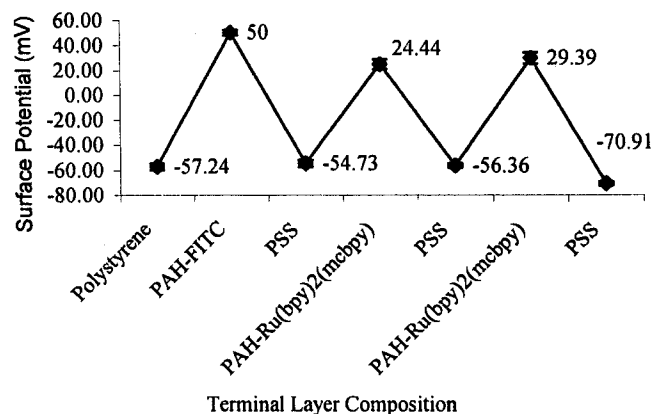
Figure 33. Zeta potential measurements on PS particles following the assembly of each layer.

5.2 Testing of Oxygen Sensors

Once successful controlled assembly of the fluorophores was demonstrated, it was

then necessary to show the immobilized dye retains analyte sensitivity. A quartz slide

was placed in a cuvette holder where fluorescence intensities at 605 nm and 525 nm were

monitored over time while a stream of oxygen was applied at approximately 0.5, 1, and 2

min. It is seen in Figure 34 that the ratio of fluorescence peak intensities, 605 nm

intensity divided by 525 nm intensity, decreases during the application of oxygen. This

trend demonstrates that the Ru(bpy)2(mcbpy) conjugated to PAH, can still function as a

oxygen indicator as expected, due to the dimensions of the films, by allowing small

molecules to easily diffuse through the films.
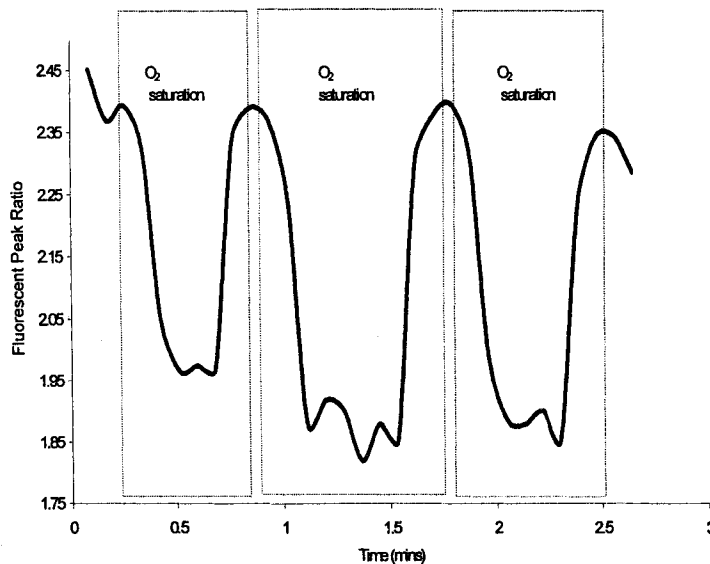
Figure 34. Oxygen response vs. time for a quartz slide. Approximately at time periods 0.5, 1, and 2 min the slide was saturated with oxygen, each time causing the fluorescence intensity ratio, 605 nm/525 nm to decrease.

The importance of demonstrating oxygen sensitivity on the optical fiber was to show the portability of the fabrication technique to produce sensors on alternate substrates. The optical fiber tip modified with {PAH-Ru(bpy)2(mcbpy)/PSS}$_{10}$ + {PAH-FITC/PSS}$_5$ architecture was tested for oxygen sensitivity by placing the tip of the fiber in a cuvette. The tip of a micro-oxygen electrode was placed next to the fiber probe. Time-based monitoring of the intensities at 524 nm and 630 nm was performed, while simultaneously recording actual oxygen content values.

Figure 35 shows the changes in oxygen measured with the oxygen electrode with the corresponding changes in the fluorescence peak ratio (630 nm/524 nm). The fluorescence peak ratio changes followed the changes in measured oxygen level, further demonstrating the quenching effect of oxygen on the PAH-Ru(bpy)2(mcbpy). The peak

ratio data were corrected for the photobleaching of FITC by collecting three minutes

of data, fitting a linear trendline to the decreasing intensities over time and using the

calculated slope to correct the data collected during the oxygen experiment. The

corrected data show excellent agreement with the microelectrode measurements.

Furthermore, these results, when compared with the observations from slide experiments,

show the ability to deposit the same sensors on optical fibers or waveguides. Light

guides provide a direct yet flexible connection to a measurement system, increasing the

number of applications where these thin-film sensors may be employed.
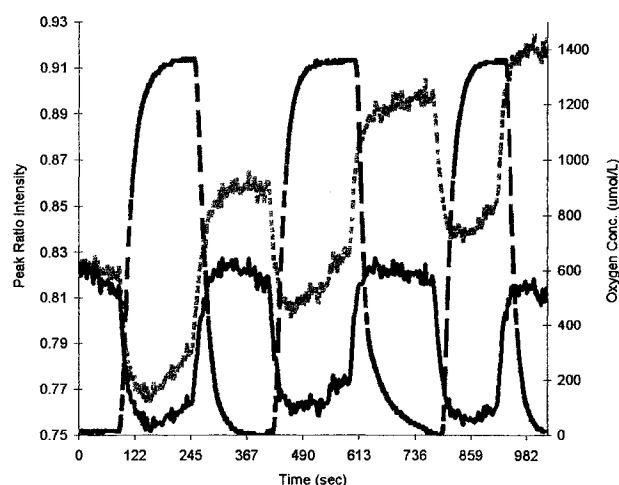
Figure 35. Time-based monitoring of oxygen concentration collected from a micro-oxygen electrode (broken line), along with fluorescence peak ratio collected from an optical fiber layered with the following architecture, {PAH-Ru(bpy)2(mcbpy)/PSS}$_{10}$ + (PAH-FITC/PSS)$_5$ (solid line.) The second peak ratio intensity data was corrected for FITC photobleaching (dots.)

The particles were suspended in a buffered solution and the fluorescence

intensities at 617 and 516 nm were monitored continuously while oxygen levels were

changed. The ratio of the 617 nm intensity to 516 nm intensity is plotted in Figure 36,

which shows a response due to the presence of N_2 and O_2. The response appears

noisy due to the fact that the particles were moving rapidly about in the cuvette during

bubbling of the gases. The key point in these results is the ability to build micro/nanosize

materials with functional properties similar to those demonstrated on larger structures,

using an identical deposition process.
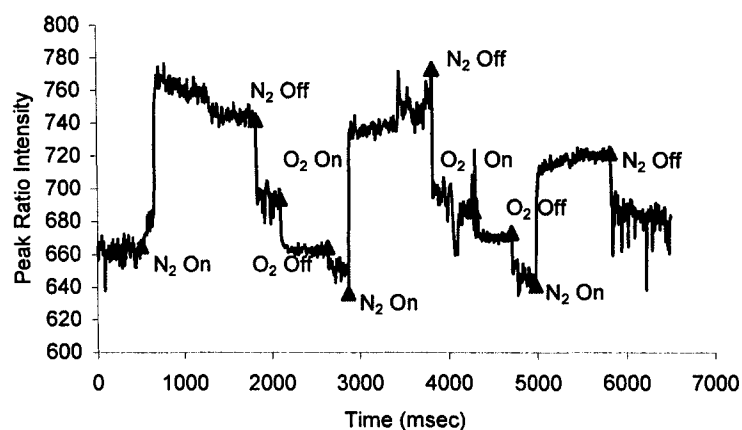
Figure 36. Ratiometric, time-based monitoring of PS particles layered with {PAH-FITC/PSS}$_1$+{PAH-Ru(bpy)2(mcbpy)/PSS}$_2$ suspended in a buffered solution, while bubbling O_2 or N_2.

The fabrication oxygen sensing films using Ru(dpp) on an optical fiber was

carried out using the method described in Chapter 4. The Ru(dpp) has a large Stern-

Volmer constant, thus is more sensitive to changes in oxygen. The optical fiber tip

modified with {PAH-488/PSS}$_{11}$ + Ru(dpp) architecture was tested for oxygen

sensitivity by placing the tip of the fiber in a custom built chamber with tubing supplying

oxygen and nitrogen. The tip of a micro-oxygen electrode was placed next to the fiber

probe. Random concentrations of N_2 and O_2 were bubbled into the chamber until a

steady O_2 concentration was reached and five spectra were then collected. The

oxygen concentration were varied from 0 to 100%. Figure 37 shows that the fiber probe

responds linearly with oxygen concentrations over the dissolved oxygen range 0 to 24

mg/L. The approximate error is 2% of the total change in peak ratio. A linear regression

was performed on the data and the r value was found to be 0.984. The characterization of

the response to changes in oxygen, by making multiple measurements at random oxygen

concentrations, allows the sensitivity and range to be determined. The error of the

multiple measurements for each concentration provides the approximate resolution of the

sensor.
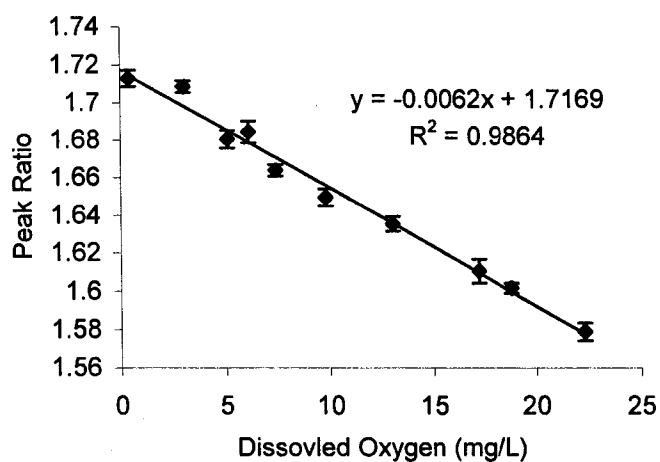
Figure 37. Oxygen sensitivity experiment with a oxygen fiber probe, that has the
architecture $(PAH-488/PSS)_{11} + Ru(dpp)$.

5.3 Nanoparticle Delivery

5.3.1 *In vitro*

Particles were then infused at a flow rate of 0.3 μL/min, pausing every 4 μL times to collect spectra. Three spectra were collected at each infused volume, to provide a statistical average. Figure 38 shows the spectra collected during the infusion process, clearly demonstrating that fluorescence intensity is a function of volume of particles infused. The peak ratio remains nearly constant, the variation representing less than 10% of the total change in peak expected for the oxygen sensing. The intensity of the two peaks increased linearly up to about 16 μL infused volume, after which the intensity began to level out. The leveling out of the two peak intensities can be explained from the optical properties of the tissue-light interaction described in Chapter 3. After the initial 16 μL, further infusion of particles will no longer be efficiently excited because the bolus of particles is larger that the full acceptance angle of the fiber and the bolus thickness is greater than the penetration depth for light through the nanoparticles.
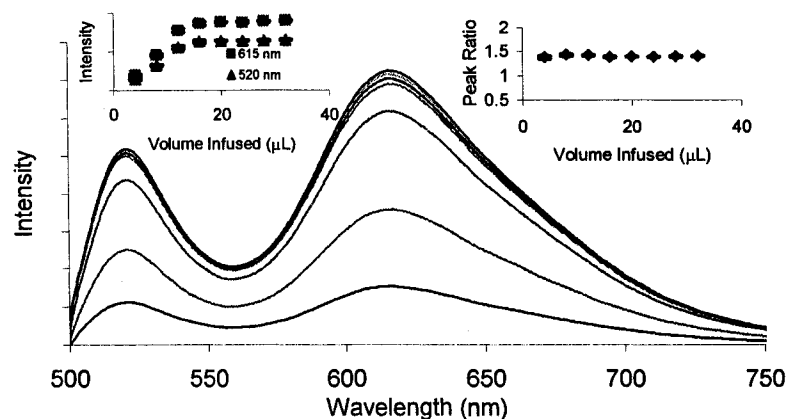
Figure 38. Fluorescence spectra collected during infusion of sensors into the brain phantom. The inset shows the intensity of the Ru(dpp) peak (615 nm) and the PAH-488 peak (520 nm) as a function of volume infused.

5.3.2 *In vivo*

Using the same experimental setup as the *in vitro* infusion experiment, an infusion experiment was carried via a cannula guide prevously implanted in the dentate gyrus of the hypocampus of a male rat. The rat was anesthetized during infusion, and spectra were collected after every 4 μL. Figure 39 is an image taken during the experiment. The laptop computer in the picture displays a spectrum of particles during the infusion.
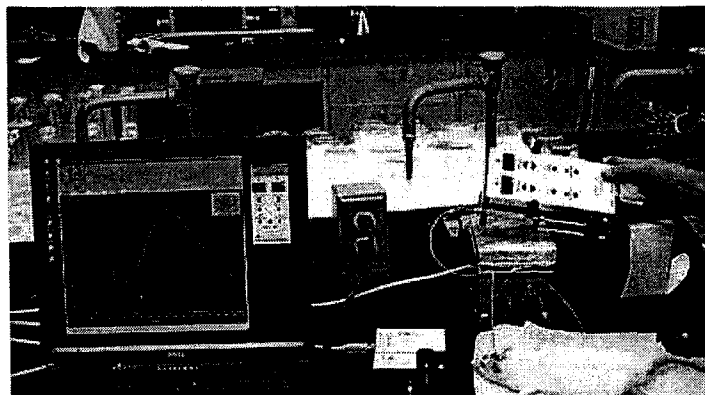
Figure 39. Image of the experimental setup used during the *in vivo* infusion experiment (note the spectrum displayed on the computer.)

The spectra presented in Figure 40 are similar to both the infusion model data and *in vitro* infusion experiment, though it is obvious that the signal levels are lower and the spectra are noisier than the in vitro experiment. The reasons for the increased noise are the non-optimal placement of the probe in relation to the infused particles and the absorption and scattering of the tissue and blood.

Encouragingly, following sacrifice and sectioning of the tissue, fluorescence confocal images (Figure 41) taken of the section tissue suggested successful delivery of the particles.

The top left image was taken in Nomarski transmission mode. The top right image was taken with 488 nm excitation and 515 nm emission, while the bottom left image was taken using 460 nm excitation and 610 nm emission. Last, the bottom right image is a combination of the three previous images, demonstrating that the particles are in the tissue.
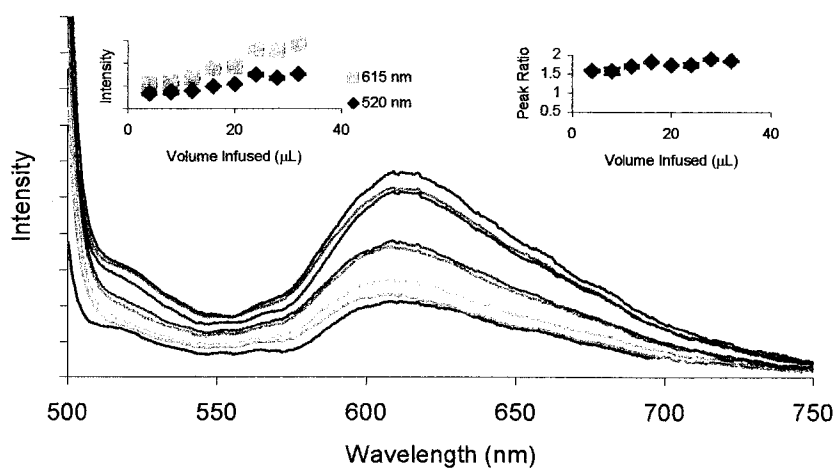
Figure 40. Spectra collected during the *in vivo* infusion experiment. The insets show the peak intensities and peak ratio with increasing infusion volume.
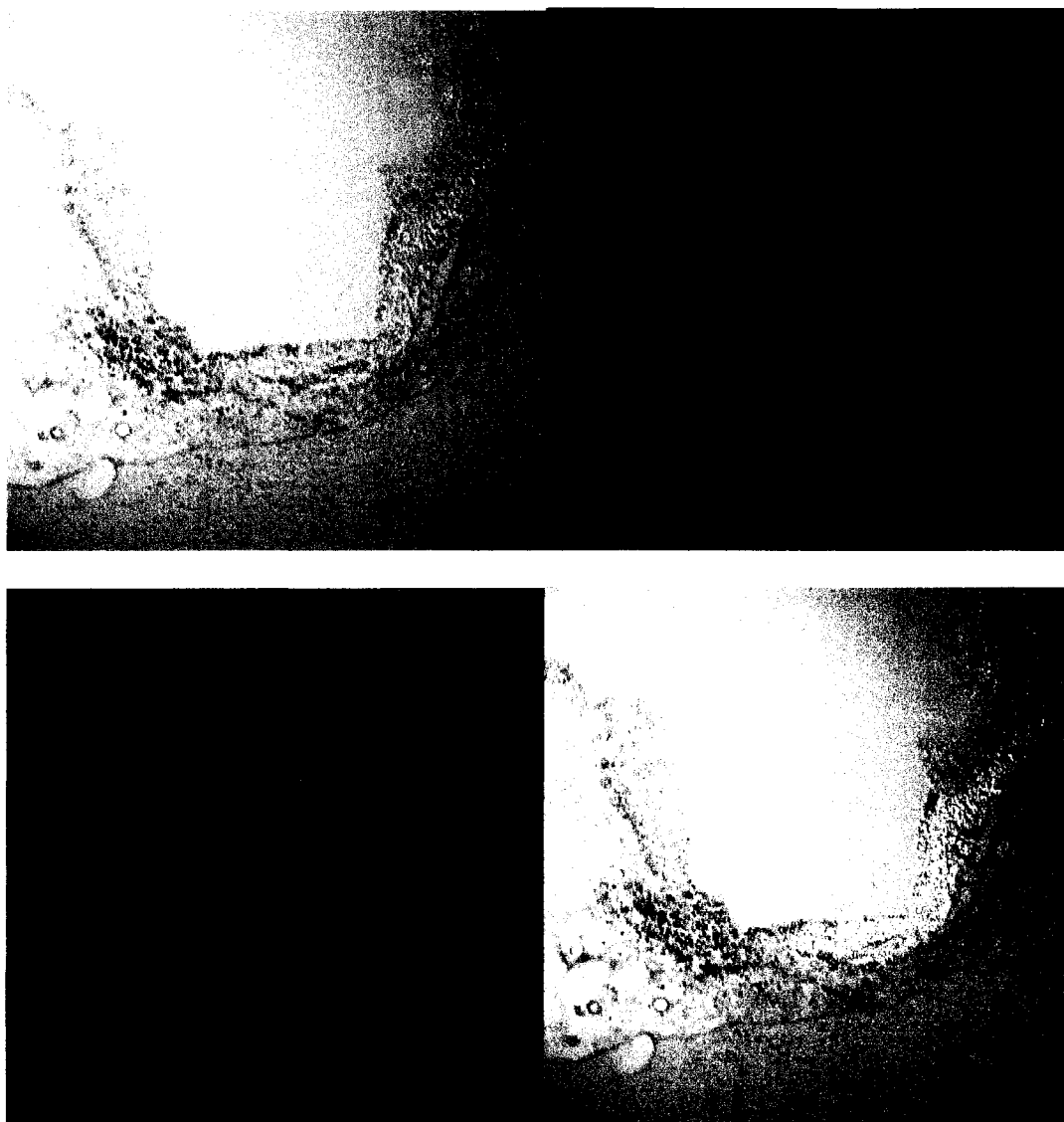
Figure 41. Phase and fluorescence confocal images of the sectioned tissue from the *in vivo* infusion experiment.

5.4 Biocompatibility

The results of the initial biocompatibility study were analyzed to determine if there was significant tissue response and migration of the infused particles. The histology did not suggest any abnormal tissue response in the brain of the rats sacrificed at 1, 2, and 4 weeks. The tissue sections were imaged using a fluorescence microscope in order to assess location and migration of the particles with fluorescent films. The only sample that yielded a fluorescent signal was from the brain of a rat infused with particles with the film architecture $(PAH-FITC/PSS)_1$, as seen in Figure 42.
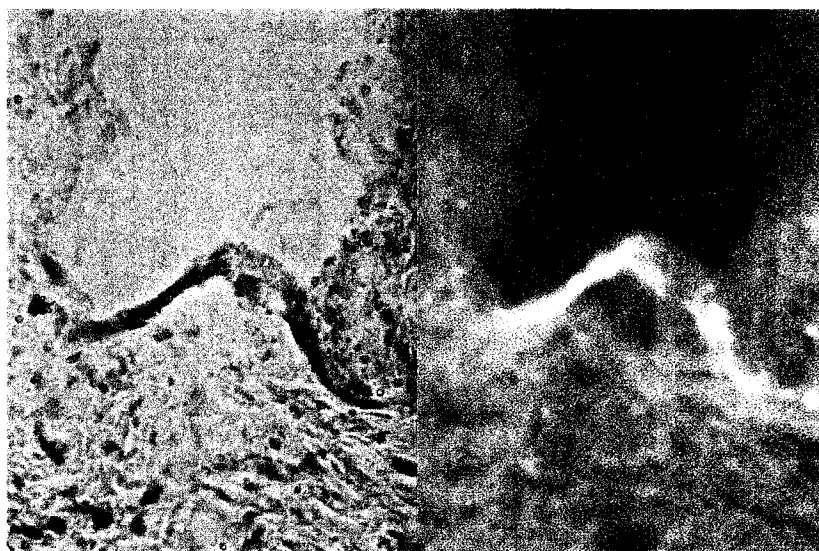
Figure 42. Light and fluorescent microscope images of the dentate gyrus of the hippacampus, taken with a 40x objective.

The tissue section was stained with methylene blue, which stains nuclear material, and it is seen in the light microscope image that significant tissue response has occurred, by lack of nuclear dust. The fluorescence image of the same location appears to contain green fluorescence at the site of the cannula guide termination. The results of this study

were not conclusive because the infusion of the particles was done prior to developing a protocol for sensor delivery. Therefore, the lack of tissue response may either be from the biocompatibility of the film components or that the particles were not efficiently delivered to the targeted brain tissue.

5.5 Glucose Probe Testing

The response to glucose of the fiber probe was tested by immersing the tip in a cuvette. Solutions of glucose increasing in steps of 200 mg/dL were pumped into the cuvette. Allowing the tip to be in contact with the glucose solution for 2 min, after which one hundred fluorescence spectra were collected for each glucose concentration. Time-based measurements of the peak ratio were collected and the results are shown in Figure 43. The peak ratio increases with increasing glucose concentration from 0 to 600 mg/dL, while there was no increase in the peak ratio from 600 to 800 mg/dL. This suggested that the maximum change in the peak ratio occurred at 600 mg/dL, which indicates that either the fluorophore was maximally quenched or there was no further reduction of oxygen in the sensing region of the films. The data for each concentration were plotted, as well as the standard deviation, as seen in Figure 44.
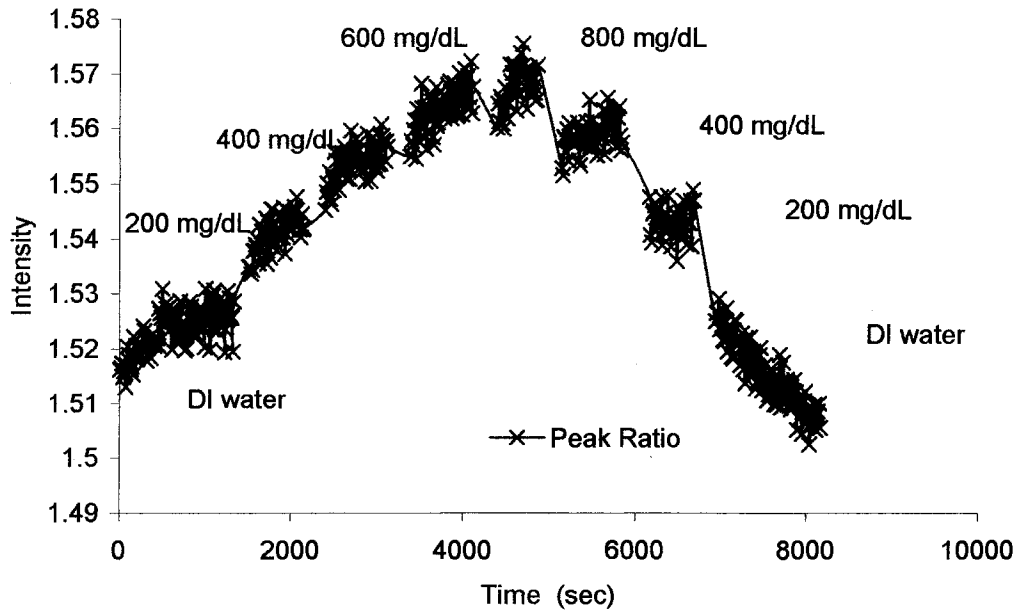
Figure 43. Glucose sensitivity experiment using a glucose fiber probe and prepared solutions of glucose.
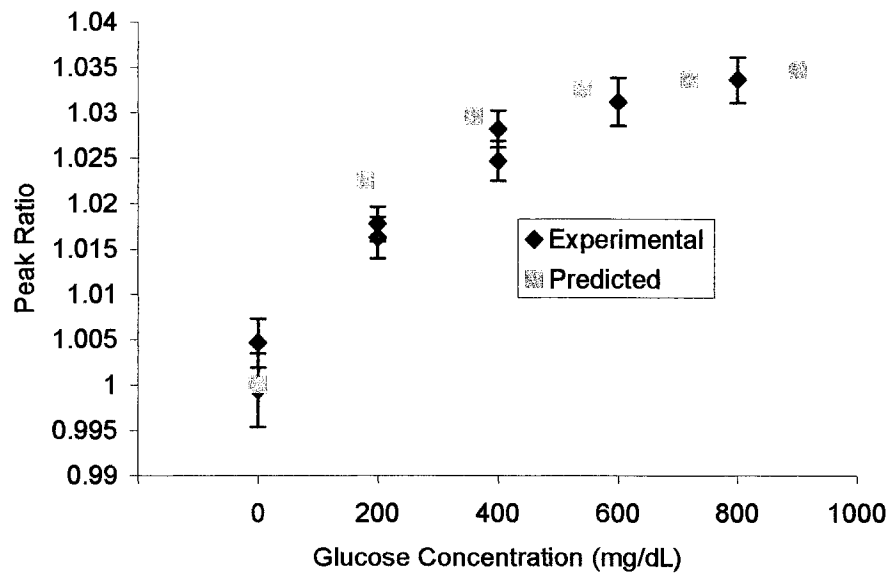
Figure 44. Glucose probe sensitivity.

It is evident in Figure 44 that there was a slight drift in the signal returning

from 600 mg/dL to DI water. The cause of this drift was examined by studying the trend

in the emission peak intensities at pH levels 3.5, 6.05, and 10.28. This experiment was

performed because the reaction of GOx with glucose produces acid, so it was suspected

that local pH levels were changing. The results for the Alexa Fluor 488[®] and Ru(dpp)

emission peaks are shown in Figure 45 and Figure 46. It was clearly seen that the

intensity decreases over time for both fluorophores in the cases neutral and high pH. This

trend is in contrast to the increase in intensity over time for both fluorophores at pH 3.5.
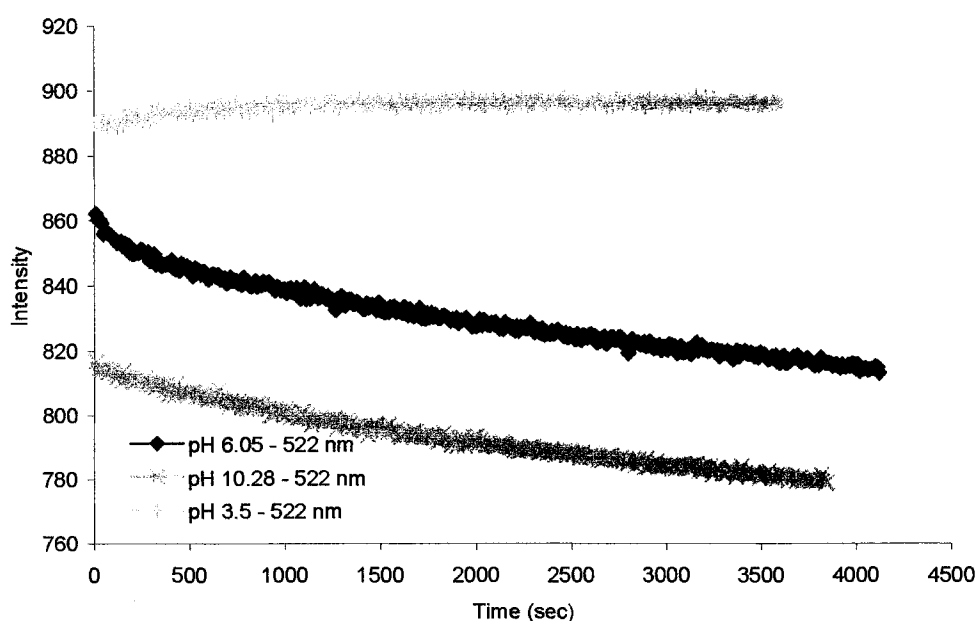
Figure 45. Time-based scans of the Alexa Fluor[®] 488 emission peak for a glucose probe
immersed in DI water at pH 3.5, 6.05 and 10.28.
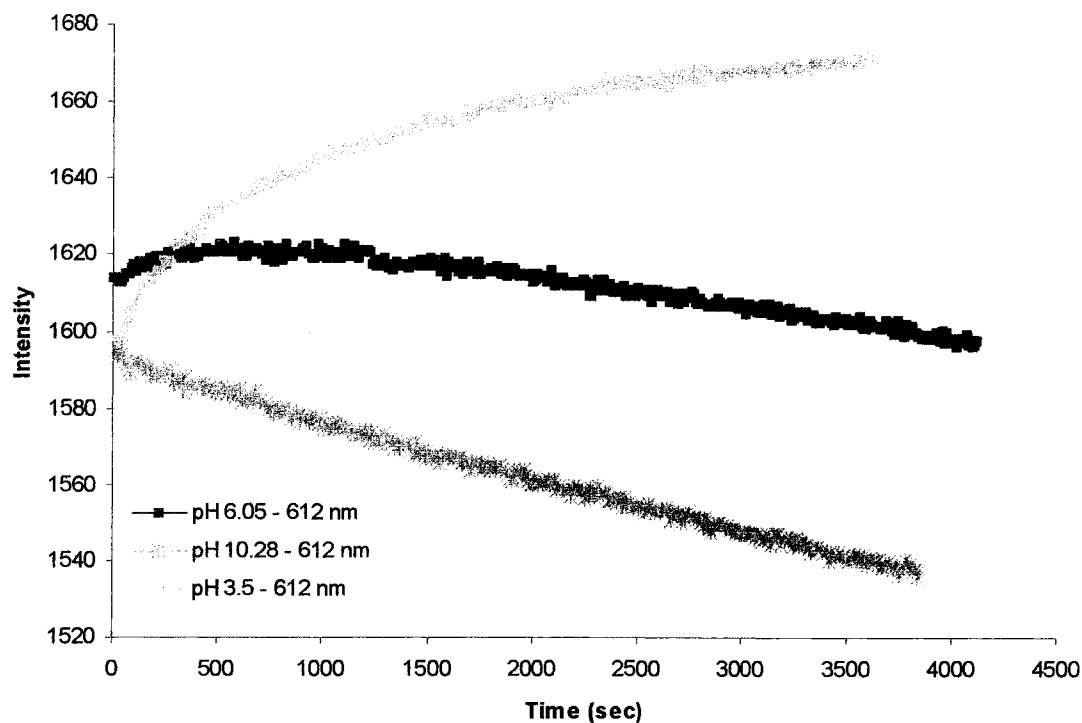
Figure 46. Time-based scans of the Ru(dpp) emission peak for a glucose probe immersed in DI water at pH 3.5, 6.05 and 10.28.

The factors that may influence this process are pH, ionic strength, molecular weight of the polyions, temperature, time of exposure to the polyion ion solution, rinsing procedure, drying procedure, substrate preparation, contamination of substrate surface during assembly, and contamination of the polyion solution. Among these factors, the two most important are pH and ionic strength. These two factors are going to affect the charged sites on the polyion, either by ions pairing with oppositely charged sites on the polyion, causing charge screen or the pH controlling the degree of ionization of the molecules.

Shiratori and Rubner demonstrate that when assembling two weak polyelec-trolytes, PAA and PAH, at different pH combinations there is not a linear trend in bilayer thickness as a function of pH.[140] The pH ranges from 6 to 8. These results do not necessarily reflect what is occurring with PAH and PSS, but it is an indication that the degree of ionization is extremely important to assembly, when using a weak polyelectrolyte.

Mendelsohn et al show that when films of PAA and PAH, both weak polyelectrolytes, are assembled at pH 3.5/7.5, respectively, and the introduced to a bath of pH 2.5 buffer, the films form pores.[141] In these conditions the PAA is weakly ionized and the PAH is almost fully ionized. Unlike when the same two polyelctrolytes are assembled at fully charge state, pH 6.5/6.5 respectively, the low pH bath does not affect the films. When changing the pH of the bath from pH 5 to pH 2.5, the 3.5/7.5 films showed a 90% increase in swelling and returned to within 10% upon raising the pH back to 5. This result is evidence that supports the dependent nature of LbL films on pH.

The effects of ionic strength reported by Dubas and Schlenoff (Langmuir 2001) state that increasing NaCl concentration causes increased layer thickness and vice versa, a decrease in layer thickness at low NaCl concentrations.[142] This change is attributed to the drawing out of water molecules unassociated with specific pairs of ion under an increasing external osmotic pressure. Fery et al demonstrated that for PAA/PAH films, those assembled from salt-free solutions retained a surface roughness of about 1 nm, regardless of how many layers were deposited,[143] which was opposite of what occurred when assembling films with salt in the polyelectrolyte solutions. In the salt case, the

surface roughness increased remarkably. It appears that salt causes changes in surface roughness, which could be understood as an increase in layer thickness. However, salt does not seem to stop assembly.

It is a possibility that the ionization of the polyelectrolyte will determine if the polyions assembly more so than the ionic strength of the polyelectrolytes, based on the idea that the ions are removable through rinsing or the presence of an oppositely charge polyion, thus allowing the film to reconfigure to assume a more energy efficient formation yet still forming a layer, as opposed to the pH conditions where the polyion is weakly ionized and does not have the ability to electrostatically attract to the oppositely charge surface. In any case, further experiments particular to PAH and PSS would need to be performed to determine which, if either, is the more controlling factor.

Despite the non-optimal performance of the sensors, the results presented above clearly show that sensing films deposited on planar and fiber-optic templates can be ported to micro/nano-templates. This dissertation supports the concept of LbL as a platform for development of micro/nanodevices to be used in many situations of biomedical interest. Further development of sensors on the above-mentioned substrates will require investigation of the performance in biologically active media, such as cell culture media, blood, etc., to further evaluate the potential for use in biomedical sensing applications. Further assessment of biocompatibility must also be completed to determine if further layers of biocompatible molecules should be employed in the outermost LbL films.

CHAPTER 6

CONCLUSIONS

This dissertation describes progress toward development of LbL as a method for fabrication of fluorescent sensors based on nanocomposite multilayer ultrathin films. In this context, methods for immobilizing indicators using LbL were assessed, and the versatility of these methods for application to templates of specific interest for optical sensing was studied. The ability to precisely deposit thin films containing fluorescent indicators onto glass slides, fiber-optics, and polymer microspheres was demonstrated. In each case, the ability to customize spectral properties was shown. For the same number of layers of labeled polyion deposited on the various templates, the resulting emission spectra were identical in shape. These films, containing Ru(bpy)2(mcbpy) conjugated to PAH as a model indicator, were shown to retain oxygen sensitivity and did not exhibit significant self quenching. When compared to direct assembly and premixing, the conjugated polyion films appear advantageous due to their linear growth and resistance to desorption during the assembly process. The ability to deposit sensing films using LbL self-assembly on such a wide variety of substrates and the availability of diverse range of fluorescent indicators makes this process an attractive method as a platform for optical sensors. The ease and mildness of fabrication would be very well suited for applications

107

ranging from tissue culture substrates with optical surface sensing films, fiber-optic

probes designed for measurements in both research and clinical settings, and fabrication

of micro/nanoparticle based sensors for implantation for chronic measurements. A model

for fabrication was developed to predict the fluorescence spectrum for a given film

architecture. A model for the coupled reaction-diffusion was developed to predict the

oxygen concentration in the sensing region of the films as a function of glucose

concentration. A model was developed to predict the resulting fluorescence spectrum for

the infusion of nanoparticles of a given film architecture. Oxygen sensors were

fabricated on quartz slides, optical fibers and nanoparticles. A protocol *in vitro* and *in

vivo* sensor delivery was developed and the delivery are nanoparticle sensors to the

dentate gyrus of the hippocampus was confirmed by real-time fluorescence monitoring of

the infusion and fluorescence confocal imaging of sectioned rat brain tissue. The

accuracy of the fiber probes was shown to be 0.5% for 0 to 100% oxygen. The fiber

probes were further developed in to a glucose probe with the addition of GOx films and a

coating of 100 μm PDMS coating, which served as a transport barrier to oxygen. The

accuracy of the glucose probe was approximately 21% for 0 to 60 mg/dL glucose.

APPENDIX A

Matlab Code For Fabrication Model

```
% modeling of sensor response to glucose changes

load spectral_data.mat
clear emission_spectrum N_emission_spectrum

% set normalization wavelength
N_lamda=525; %wavelength for spectral normalization
wl=N_fiber(:,1);
N_exceed=find(wl>=N_lamda);
N_index=N_exceed(1);


% labeling ratio
PAH_AF_LR=0.4;
PAH_Ru_LR=0.7;

% number of layers for PAH layers
NL_AF=5;
NL_Ru=3;

% integration time (msec)
int=600;
s=sprintf('%d',int);
s2=['Predicted Signal @ ' s 'msec integration'];

for i=0:NL_Ru
    NL_PAH_Ru=i;
    NL_PAH_AF=5;
    spec_AF=NL_PAH_AF/3*em_AF_int(:,2)*int;
    spec_Ru=NL_PAH_Ru/30*em_Ru_int(:,2)*int;
%   spec_fiber=fiber_int(:,2)*int;
    emission_spectrum(:,(i+1))=spec_AF+spec_Ru;
```

```
N_emission_spectrum(:,(i+1))=emission_spectrum(:,(i+1))/max(emission_spectrum(N_i
ndex,(i+1)));
end

figure(1)
subplot(2,1,1)
plot(wl(1:906),emission_spectrum(1:906,:))
xlabel('Wavelength (nm)')
ylabel(s2)

figure(2)
plot(wl(1:906),N_emission_spectrum(1:906,:))
xlabel('Wavelength (nm)')
ylabel('Predicted Relative Intensity')
```

APPENDIX B

MathCad CODE FOR INFUSION MODEL

$\mu m := 1 \cdot 10^{-6} m$

$nm := 1 \cdot 10^{-9} m$ **Unit definitions**

$\mu mol := 1 \cdot 10^{-6} mol$

$dL := 1 \cdot 10^{-1} L$

$\mu L := 1 \cdot 10^{-6} L$

$\mu g := 1 \cdot 10^{-6} gm$

$ng := 1 \cdot 10^{-9} gm$

$cm\_Hg := \dfrac{in\_Hg}{2.54}$

$ms := 1 \cdot 10^{-3} s$

$ns := 1 \cdot 10^{-9} s$

Percent Solids

$\%solids_{w\_v} := .10 \dfrac{g}{mL}$ **% solids given as W/V, using density of PS, converted to V/V.**

$\rho_{PS} := 1.05 \dfrac{g}{cm^3}$

$\%solids_{v\_v} := \dfrac{\%solids_{w\_v}}{\rho_{PS}}$

$\%solids_{v\_v} = 0.095$

Radius of Particles

$radius := \dfrac{30 1nm}{2}$ **Determine the Vol of 1 particle**

$volume_{particle} := \dfrac{4}{3} \cdot \pi \cdot radius^3$

Volume of Particle Solution

$volume_{solution} := 100 \mu L$

$total_{particles} := \dfrac{volume_{solution} \cdot \%solids_{v\_v}}{volume_{particle}}$ **Knowing the total Vol of particles and the vol of 1 particle, the total number of particles is determined**

$total_{particles} = 6.67 \times 10^{11}$

After 8% loss for 11 bilayers

$$total_{particles} := 2.67 \cdot 10^{11}$$

$$Conc_{particles} := \frac{total_{particles}}{1.5mL}$$

Split sample into 2 samples

$$total_{particles} := \frac{total_{particles}}{2}$$

$$Conc_{particles} := \frac{Conc_{particles}}{2}$$

$$Conc_{particles} = 8.9 \times 10^{10} \frac{1}{mL}$$

UV-Vis absorbance measurements used to determine the labeling ratio of 488 to PAH

$$A_{494} := 0.097472032$$

$$\varepsilon_{488} := 78000 \frac{L}{mol \cdot cm}$$

$$MW_{488} := 643.41 \frac{gm}{mol}$$

$$MW_{PAH} := 15000 \frac{gm}{mol}$$

$$vol := 2.2mL$$

$$l := 1cm$$

$$vol_{PAH488} := 0.2mL$$

$$A := 6.02 \cdot 10^{23} \cdot \frac{1}{mol}$$

$$A_{494} = \varepsilon_{488} l \cdot c$$

$$c_{488} := \frac{A_{494}}{\varepsilon_{488} l}$$

$$c_{488} = 1.25 \times 10^{-9} \frac{mol}{mL}$$

Expecting 8% loss of particles due to the rinsing procedures (calculating performed in excel - particle loss.xls)

The concentration of the particles was then deteremined by the total number of particles divided by the vol of buffer they are suspended in

Molecular properties of AlexaFluor 488 and PAH.

DI water vol = 2 mL

PAH-488 vol = 0.2 mL   **Experimental conditions**

Total vol = 2.2 mL

x interval = 2 nm
Integration time = 4 sec

Avogadro's number

Using Beer-Lambert law

Molar concentration

$$C_{488} := c_{488} \cdot MW_{488}$$

$$C_{488} = 0.804 \frac{\mu g}{mL}$$ **Mass Concentration**

$$N_{488} := c_{488} \cdot vol \cdot A$$ **Number of molecules of 488**

Assume PAH conc. is 2 mg/mL

$$C_{PAH} := 2 \frac{mg}{mL}$$

$$c_{PAH} := \frac{C_{PAH}}{MW_{PAH}}$$

$$c_{PAH} = 1.333 \times 10^{-7} \frac{mol}{mL}$$

$$mass_{PAH} := C_{PAH} \cdot vol_{PAH488}$$

$$moles_{PAH} := \frac{mass_{PAH}}{MW_{PAH}}$$

$$N_{PAH} := moles_{PAH} \cdot A$$ **Number of molecules of PAH**

$$N_{PAH} = 1.605 \times 10^{16}$$

$$Labeling_{ratio} := \frac{N_{488}}{N_{PAH}}$$ **Labeling Ratio**

$$Labeling_{ratio} = 0.103$$

Determine the mass of 488 in the films

$$Stepgrowth_{PAH488} := 1.82 nm$$ **Determined from experiments**

$$StepMASS_{PAH488} := 7.86 ng$$ **Step mass growth on QCM**

$$r_{QCM} := \frac{0.6mm}{2}$$

$$SA_{QCM} := 2 \cdot \pi \cdot r_{QCM}^2$$

$$Coverage_{PAH488} := \frac{StepMASS_{PAH488}}{SA_{QCM}}$$

$$Coverage_{PAH488} = 13.9 \frac{mg}{m^2}$$

$\text{Layers}_{PAH488} := 10$

$\text{Thickness} := \text{Layers}_{PAH488} \cdot \text{Stepgrowth}_{PAH488}$

$SA_{particle} := \pi \cdot \text{radius}^2$

$SA_{particle} = 0.071 \mu m^2$

$\text{Mass}_{PAH488} := SA_{particle} \cdot \text{Coverage}_{PAH488} \cdot \text{Layers}_{PAH488}$

$\text{Mass}_{PAH488} = 9.891 \times 10^{-6} ng$

$N_{PAH488} := \dfrac{\text{Mass}_{PAH488}}{MW_{PAH}} \cdot A$

$N_{PAH488} = 3.969 \times 10^5$

$N_{488} := N_{PAH488} \cdot \text{Labeling}_{ratio}$

$N_{488} = 4.092 \times 10^4$ **Number of molecules per particle**

Determine the mass and concentration of Rudpp in the films

Loading Solution

$MW_{rudpp} := 1169.17 \dfrac{gm}{mol}$ **Molecular properties of Rudpp**

$\varepsilon_{rudpp} := 29000 \dfrac{L}{mol \cdot cm}$

$A_{initial} := 0.052699884$ **Determine the conc of the Rudpp loading solution.**

$\text{Conc}_{verify} := \dfrac{A_{initial}}{\varepsilon_{rudpp} \cdot l} \cdot MW_{rudpp}$

$\text{Conc}_{verify} = 2.125 \times 10^{-3} \dfrac{mg}{mL}$

$\text{Mass}_{initial} := \text{Conc}_{verify} \cdot 2.04mL$

$\text{Conc}_{initial} := \dfrac{\text{Mass}_{initial}}{40 \mu L}$

$\text{Conc}_{initial} = 0.108 \dfrac{mg}{mL}$ **Concentration of loading solution**

$\text{Mass}_{\text{load}} := \text{Conc}_{\text{initial}} \cdot 1\text{mL}$

$\text{Mass}_{\text{load}} = 0.108\text{mg}$

$A_{\text{super}} := 0.175070127$ **Determine the conc of the Rudpp after loading**

$$\text{Conc}_{\text{super}} := \frac{A_{\text{super}}}{\varepsilon_{\text{rudpp}} \cdot 1} \cdot \text{MW}_{\text{rudpp}}$$

$$\text{Conc}_{\text{super}} = 7.058 \times 10^{-3} \frac{\text{mg}}{\text{mL}}$$

$\text{Mass}_{\text{super}} := \text{Conc}_{\text{super}} \cdot 1.5\text{mL}$

$\text{Mass}_{\text{super}} = 10.587\mu\text{g}$

$$\frac{\text{Conc}_{\text{initial}} - \text{Conc}_{\text{super}}}{\text{Conc}_{\text{initial}}} \cdot 100 = 93.486$$ **Percentage of Rudpp loaded into the films**

The particles were suspended in PSS overnight to ensure they had a negative outer surface charge. Consequently, some Rudpp was removed from the particles. An absorbance measurment of the PSS+Rudpp supernatant was performed to determine the concentration of Rudpp removed from the films.

$A_{\text{afterpss}} := 0.099134127$

$$\text{Conc}_{\text{afterpss}} := \frac{A_{\text{afterpss}}}{\varepsilon_{\text{rudpp}} \cdot 1} \cdot \text{MW}_{\text{rudpp}}$$

$$\text{Conc}_{\text{afterpss}} = 3.997 \times 10^{-3} \frac{\text{mg}}{\text{mL}}$$

$\text{Mass}_{\text{afterpss}} := \text{Conc}_{\text{afterpss}} \cdot 2.5\text{mL}$

$$\text{Conc}_{\text{desorbed}} := \frac{\text{Mass}_{\text{afterpss}}}{0.5\text{mL}}$$

$$\text{Conc}_{\text{desorbed}} = 0.02\frac{\text{mg}}{\text{mL}}$$

$\text{Mass}_{\text{desorbed}} := \text{Conc}_{\text{desorbed}} \cdot 1\text{mL}$

$\text{Mass}_{\text{desorbed}} = 19.984\mu\text{g}$

$$\text{Conc}_{\text{initial}} - \text{Conc}_{\text{super}} = 0.101 \frac{\text{mg}}{\text{mL}}$$

Concentration loaded into the films

$$\text{Conc}_{\text{desorbed}} = 0.02 \frac{\text{mg}}{\text{mL}}$$

After soaking in PSS overnight, the conc (1 mL) desorbed:

$$\text{Conc}_{\text{final}} := \text{Conc}_{\text{initial}} - \text{Conc}_{\text{super}} - \text{Conc}_{\text{desorbed}}$$

$$\text{Conc}_{\text{final}} = 0.081 \frac{\text{mg}}{\text{mL}}$$

The conc of Ru(dpp) left in the layers

$$\text{Conc}_{\text{removed}} := \text{Conc}_{\text{super}} + \text{Conc}_{\text{desorbed}}$$

$$\text{Conc}_{\text{removed}} = 0.027 \frac{\text{mg}}{\text{mL}}$$

The conc of Ru(dpp) removed from the layers

$$\frac{\text{Conc}_{\text{initial}} - \text{Conc}_{\text{removed}}}{\text{Conc}_{\text{initial}}} \cdot 100 = 75.044$$

Percentage loaded into films

$$\text{Mass}_{\text{total\_rudpp}} := \text{Mass}_{\text{load}} - \text{Mass}_{\text{super}} - \text{Mass}_{\text{desorbed}}$$ **Mass of Rudpp total**

$$\text{Mass}_{\text{total\_rudpp}} = 0.078 \text{mg}$$

$$\text{Mass}_{\text{rudpp}} := \frac{\text{Mass}_{\text{total\_rudpp}}}{\text{total}_{\text{particles}}}$$

$$\text{Mass}_{\text{rudpp}} = 5.827 \times 10^{-7} \text{ng}$$

Mass of Rudpp per particle

$$N_{\text{rudpp}} := \frac{\text{Mass}_{\text{rudpp}}}{\text{MW}_{\text{rudpp}}} \cdot A$$

$$N_{\text{rudpp}} = 3.0002 \times 10^{5}$$

Molecules of Rudpp per particle

The number of partilces can be determined

$$N_{particles} = \int_0^{t_f} conc \cdot \left(\frac{d}{dt}vol\right) dt$$

$$flow_{rate} := 0.3\frac{\mu L}{min}$$

Volume $:= 32\mu L$

$$conc := Conc_{particles}$$

$$t_f := \frac{Volume}{flow_{rate}}$$

$$t_f = 6.4 \times 10^3 \, s$$

$$t_f = 6.4 \times 10^3 \, s$$

$$N_{particles} := \int_0^{t_f} conc \cdot \left(flow_{rate}\right) dt$$

$$N_{particles} = 2.848 \times 10^9$$

Once the number of particles in known, the concentration of each fluorophore can be estimated

$$N_{rudpp\_total} := N_{rudpp} \cdot N_{particles}$$

$$N_{rudpp\_total} = 8.544 \times 10^{14}$$

$$N_{488\_total} := N_{488} \cdot N_{particles}$$

$$N_{488\_total} = 1.165 \times 10^{14}$$

$$Q_{rudpp} := 0.38$$

Extinction Coefficients for Rudpp and 488

$$Q_{488} := 0.90$$

$$F_{rudpp}\left(I_{rudpp}\right) := I_{rudpp} \cdot Q_{rudpp} \cdot \varepsilon_{rudpp} \cdot l \cdot N_{rudpp\_total} \cdot \frac{mol}{mL}$$

Fluorescence as a function of number of particles

$$F_{488}\left(I_{488}\right) := I_{488} \cdot Q_{488} \cdot \varepsilon_{488} \cdot l \cdot N_{488\_total} \cdot \frac{mol}{mL}$$

$\text{Scalar} := 1 \cdot 10^5$

$F_{\text{fiber}}\left(I_{\text{fiber}}\right) := I_{\text{fiber}} \cdot \text{Scalar}$

$I_{\text{rudpp}} :=$

	0
0	0.04

$I_{\text{fiber}} :=$

	0
0	1

$I_{488} :=$

	0
0	0.34

$X :=$

	0
0	500.26

$F := F_{\text{rudpp}}\left(I_{\text{rudpp}}\right) + F_{488}\left(I_{488}\right) + F_{\text{fiber}}\left(I_{\text{fiber}}\right)$

$F =$

	0
0	$3.12 \cdot 10^{21}$
1	$3.184 \cdot 10^{21}$
2	$3.257 \cdot 10^{21}$
3	$3.33 \cdot 10^{21}$
4	$3.412 \cdot 10^{21}$
5	$3.499 \cdot 10^{21}$
6	$3.598 \cdot 10^{21}$
7	$3.694 \cdot 10^{21}$
8	$3.799 \cdot 10^{21}$
9	$3.9 \cdot 10^{21}$
10	$4.012 \cdot 10^{21}$
11	$4.124 \cdot 10^{21}$
12	$4.249 \cdot 10^{21}$
13	$4.365 \cdot 10^{21}$
14	$4.49 \cdot 10^{21}$
15	$4.616 \cdot 10^{21}$

APPENDIX C

MATLAB CODE FOR REACTION-DIFFUSION MODEL

```
function pdex4

close all
clear all
clc

tPDMS=[0 0 0 0 0];
%tPDMS=[1 5 10 50 100]*1e-6;
glures=10; % glucose concentration step size
glumax=51; % max glucose concentration (mM)

global k3 Kmg Et r1 r2 r3 r4 R n;
k1 = 1e5 ; % in 1/(M sec)
kminus1 = 3e3 ;% in 1/sec
k2= 300; % in 1/sec
Kmg = 33e-3 ;% in M
k3 = 1e6 ; % in 1/(M sec)
kminus3 = 150 ; % in 1/sec
k4 = 50 ; % in 1/sec
KmO = 0.20e-3; % in M for oxygen

n1 = 11; %no of layers in PAH-488/PSS
n2 = 5; %no of layers in GOx/PEI

tt1 = 8e-9; % thickness of one PAH-488/PSS bilayer
r1 = 100e-6; % radius of the optical fiber
r2 = r1 + (n1*tt1); % final radius after the 488 layers
tt2 = 12e-9; % thickness of one GOx/PEI bilayer
r3 = r2 + n2*tt2; % final radius after the GOx/PEI layers

m = 1; % cylindrical coordinates
% x = [r1:10e-9:r4]; % radial distance
t = [0:1:20];   %time mesh
```

```matlab
Et = 5e-3; % total enzyme concentration

xres1=tt1; % spatial resolution for PAH-488 + Ru
xres2=tt2; % spatial resolution for GOx/PEI


for n4 = 1:length(tPDMS)

  for n=1:glures:glumax;

    r4 = r3 + tPDMS(n4); % final radius after the PDMS layer
    xres3=tPDMS(n4)/20; % spatial resolution for PDMS layer
    x = [r1:xres1:r2 (r2+xres2):xres2:r3 (r3+xres3):xres3:r4];
    % size(x')
    % pause

    %x = [r1:xres1:r2 (r2+xres2):xres2:r3];

    % radial distance

%     Et = 50e-3;
    %     n = nn/2;
    sol = pdepe(m,@pdex4pde,@pdex4ic,@pdex4bc,x,t);%call of other functions that
define PDE,IC and BC.
    % u1(n,:) = sol(end,:,1); % glucose concentration
%figure(1)
%     surf(x,t,sol(:,:,2))
%     drawnow
%     pause

    u2 = sol(end,:,2); % oxygen concentration for last time point, at all positions
    u2;

    ru = 1:n1;
    uru(n,ru)= u2(ru)
    n
    avgru(n,n4) = mean(uru(n,:));

  end




figure(1)
plot((x(ru)-r1)*1e9,uru*1e3)
axis auto
```

```
title('Oxygen Concentration Profile')
xlabel (' Radial Distance (nm)')
ylabel (' Oxygen Concentration (mM)')
drawnow
legend('1 mM','11 mM','21 mM','31 mM','41 mM','51 mM',-1)

end

glu=1:glures:glumax;
figure(2)
plot(glu,avgru(glu,:)*1e3)
title('Average Oxygen Concentration in PAH-488/PSS + Ru(dpp) Layers')
xlabel('Bulk Glucose Concentration (mM)')
ylabel('Average Oxygen Concentration (mM)')
%legend ('1 \mum PDMS','5 \mum PDMS','10 \mum PDMS', '50 \mum PDMS', '100
\mum PDMS' ,-1)

% figure(4)
% plot(glu,avgref)
% title('Average Oxygen Concentration in 488')
% xlabel('Glucose Concentration  (M)')
% ylabel('Average Oxygen Concentration (M)')
% legend ('1 Bl','6 Bl','11 Bl','16 Bl','21 Bl','26 Bl','31 Bl','36 Bl','41 Bl','46 Bl',-1)

% average_in_films_mM = avgf*1e3
% average_in_Ru_mM = avgru*1e3
% avergae_in_488_mM = avgref*1e3




% figure(3)
% plot(x,u2)
% axis auto
% title('oxygen concentration profile')
% xlabel (' radial distance in m')
% ylabel (' concentration in mol/l')
% legend('0.5mM','1mM','1.5mM','2mM','2.5mM','3mM','3.5mM','4mM','4.5mM','5mM',-
1)
% figure(4)
% plot(x,u1)
% axis auto
% title('glucose concentration profile')
% xlabel (' radial distance in m')
% zlabel (' concentration in mol/l')


% % ----------------------------------------------------------------
```

```matlab
function [c,f,s] = pdex4pde(x,t,u,DuDx)
global k3 Kmg Et k1 k2 k4 kminus1 kminus3 r1 r2 r3 r4 R;

 k1 = 1e5 ; % in 1/(M sec)
kminus1 = 3e3 ;% in 1/sec
k2= 300; % in 1/sec
Kmg = 33e-3 ;% in M
k3 = 1e6 ; % in 1/(M sec)
kminus3 = 150 ; % in 1/sec
k4 = 50 ; % in 1/sec
KmO = 0.20e-3; % in M for oxygen


% n1 = 10; %no of layers in 488
% n2 = 10; %no of layers in Ru
% n3 = 10; %no of layers in GOx
% n4 = 10; %no of layers in PDMS
% tt = 8e-9;% thickness of one bilayer
% r1 = 150e-9;% radius of the polystyrene nanoparticle
% r2 = r1 + (n1*tt);% final radius after the 488 layer
% r3 = r2 + (n2*tt);% final radius after the Ru layer
% R = r1 + ((n3+n1+n2)*tt);% final radius after the GOx layer
% r4 = R + (n4*tt); % final radius after the PDMS layer



c = [1; 1];
if ( x > r3)
    f = [0.045*2.2e-9; 2.2e-9] .* DuDx;
    s = [0; 0];
else
    if ( x > r2)
        %f = [9.87e-14; 1.15e-9] .* DuDx;
        f = [9.87e-16; 1.15e-9] .* DuDx;
        F =
(k1*k2*u(1)*Et*(kminus3+k4))/(k3*k4*u(2)*(kminus1+k2+k1*u(1))+k1*k2*u(1)*(kmi
nus3+k4+k3*u(2)));
        X2  = (k3*u(2).*F)/(kminus3 + k4);
        X1 = (k1*u(1)*((kminus3 + k4)*(Et - F) - k3*u(2)*F))/((k1*u(1) + kminus1
```

```
+k2)*(kminus3+k4));
    F1 = k1*u(1)*(Et-F-X1-X2) - kminus1*X1;
    F2 = k3*u(2)*F - kminus3*X2;

    s =[-F1; -F2];
  else
    %f = [9.87e-14; 1.15e-9] .* DuDx;
    f = [9.87e-16; 1.15e-9] .* DuDx;
    s = [0; 0];
  end
end


% ------------------------------------------------------------
function u0 = pdex4ic(x);
global n
u0 = [n*1e-3; 2e-3 ];


% ------------------------------------------------------------
function [pl,ql,pr,qr] = pdex4bc(xl,ul,xr,ur,t)
global n
pr = [ur(1)-n*1e-3; ur(2)-2e-3];
qr = [0; 0];
pl = [0; 0];
ql = [1; 1];
```

BIBLIOGRAPHY

[1] F. Navarro-Villoslada, G. Orellana, M.C. Moreno-Bondi, T. Vick, M. Driver, G. Hildebrand, K. Liefeith, "Fiber-Optic Luminescent Sensors with Composite Oxygen-Sensitive Layers and Anti-Biofouling Coatings," *Anal. Chem.*, 2001, 73, 5150-5156.

[2] R. N. Pattison, J. Swamy, B. Mendenhall, C. Hwang, B.T. Frohich, "Measurement and Control of Dissolved Carbon Dioxide in Mammalian Cell Culture Processes Using an in Situ Fiber Optic Chemical Sensor," *Biotechnol. Prog.*, 2000, 16, 769-774.

[3] M. Janowiak, H. Huang, S. Chang, L.H. Garcia-Rubio, "Development of a Fiber Optic pH Sensor for On-Line Control," *ACS Symp. Ser.*, 2001, No. 795, 195-210.

[4] O.S. Wolfbeis , I. Oehme, N. Papkovskaya, I. Klimant. "Sol-Gel Based Glucose Biosensors Employing Optical Oxygen Transducers, and a Method for Compensating for Variable Oxygen Background," *Biosens. Bioelectron.* 2000, 366, 807-810.

[5] E. S. Jin., B.J. Norris, P. Pantano, "An Electrogenerated Chemiluminescence Imaging Fiber Electrode Chemical Sensor for NADH," *Electroanalysis,* 2002, 136, 17430.

[6] R. Russell, M. Pishko, C. Gefrides, M. McShane, and G. Coté, "A Fluoresence-based Glucose Biosensor Using Concavalin A and Dextran Encapsulated in a poly(ethylene glycol) Hydrogel," *Anal. Chem.*, 1999, 71, 3126-3132.

[7] H. A. Clark, S. L. R. Barker, M. Brasuel, M. T. Miller, E. Monson, S. Parus, Z. Y. Shi, A. Song, B. Thorsrud, R. Kopelman, A. Ade, W. Meixner, B. Athey, M. Hoyer, D. Hill, R. Lightle, and M. Philbert, "Subcellular optochemical nanobiosensors: probes encapsulated by biologically localised embedding (PEBBLEs)," *Sensors and Actuators B-Chemical,* 1998, 51, 12-16

[8] H. A. Clark, M. Hoyer, M. A. Philbert, and R. Kopelman, "Optical nanosensors for chemical analysis inside single living cells. 1. Fabrication, characterization, and methods for intracellular delivery of PEBBLE sensors," *Anal. Chem.*, 1999, 71, 4831-4836.

[9] H. A. Clark, R. Kopelman, R. Tjalkens, and M.A. Philbert, "Optical nanosensors for chemical analysis inside single living cells. 2. Sensors for pH and calcium and the intracellular application of PEBBLE sensors," *Anal. Chem.* 1999, 71, 4837-4843.

[11] H. Xu, JW. Aylott, R. Kopelman, TJ Miller, MA Philbert, "A real-time ratiometric method for the determination of molecular oxygen inside living cells using sol-gel-based spherical optical nanosensors with applications to rat C6 glioma," *Anal.Chem.*, 2001, 73 (17): 4124-4133

[12] R. Ballerstadt and J.S. Schultz,"A Fluorescence Affinity Hollow Fiber Sensor for Continuous Transdermal Glucose Monitoring. 2000, *Anal. Chem.*, 72, 4185-4192.

[13] G. Decher, J.-D. Hong, "Buildup of ultrathin multilayer films by a self assembly process: II. Consecutive adsorption of anionic and cationic bipolar amphiphiles polyelectrolytes on charged surfaces." *Ber Bunsenges. Phys. Chem.*, 1991, 210/211, 831-835.

[14] Handbook of Surfaces and Interfaces of Materials, Chapter 4, Yuri M. Lvov, Academic Press, 2001, Vol. 3, Nanostructured Materials, Micelles and Colloids.

[15] G.B. Sukhorukov, E. Donath, S. Davis, H. Lichtenfield, F. Caruso, V.I. Popov, and H. Mohwald. 1998 "Stepwise Polyelectrolyte Assembly on Particle Surfaces: a Novel Approach to Colloid Design," *Poly. Adv. Tech.*, 9, 759-767.

[16] S. Lee, J. Kumar, and S. Tripathy, "Thin-Film Optical Sensors Employing Polyelectrolyte Assembly," *Langmuir,* 2000 16(26): 10482-10489.

[17] T.S. Lee, C. Yang, W.H. Park, "Synthesis and electrostatic multilayer assembly of an acridine-containing polymer with properties of an optical sensor," Macromol. *Rapid Commun.* 2001, 21 951-955.

[18] P. Grant, Y. Lvov, M. McShane, "Nanostructured Fluorescent Particles for Glucose Sensing," *Proc SPIE*, 2002, 24, 4624.

[19] M. Fang, P.S. Grant, M.J. McShane, G.S. Sukhorukov, V. Golub, Y.M. Lvov, "Magnetic Bio/Nanoreactor with Multilayer Shells of Glucose Oxidase and Inorganic Nanoparticles," *Langmuir*, 2002, 18, 6338-6344.

[20] T. Cooper, A. Campbell, and R. Crane, "Formation of Polypeptide-Dye Multilayers be an Electrostatic Self-Assembly Technique," *Langmuir,* 1995, 11, 2713-2718.

[21] D. Yoo, J. Lee, and M. Rubner, "Investigations of New Self-Assembled Mulitlayer Thin Films Based on Alternately Adsorbed Layers of Polyelectrolytes and Functional Dye Molecules," *Mat. Res. Soc. Symp. Proc.*, 1996, 413, 395-400.

[22] K. Ariga, M. Onda, Y. Lvov, and T. Kunitake, "Alternate Layer-by-Layer Assembly of Organic Dyes and Proteins is Facilitated by Premixing with Linear Polyions," *Chem. Lett.,* 1997, 25-26.

[23] J. Kerimo, D. Adams, and Paul Barbara, "NSMO Investigatons of the Spectroscopy and Morphology of Self-Assembly Multilayerd Thin Films," *J. Phys. Chem. B*, 1998, 102, 9451-9460.

[24] D. Haines, ed. Fundamental of Neuroscience. New York: Churchill Livingstone, 1997.

[25] A. Guyton, J. Hall, Textbook of Medical Physiology ninth ed. Philadelphia: W.B. Saunders Company, 1996.

[26] R Forsyth, A Fray, M Boutelle, M Fillenz, C Middleditch, A Burchell, "A role for astrocytes in glucose delivery to neurons?," *Dev Neurosci,* 1996, 18, 360-370.

[27] LK Fellows, MG Boutelle, "Rapid changes in extracellular glucose levels and blood flow in the striatum of the freely moving rat," *Brain Res,* , 1993, 604, 225-231.

[28] Y Hu, GS Wilson, "Rapid changes in local extracellular rat brain glucose observed with an in vivo glucose sensor," *J Neurochemistry,* 1997, 68, 1745-1752.

[29] MG Boutelle, LK Fellows, C Cook, "Enzyme packed bed system for the on-line measurement of glucose, glutamate, and lactate in brain microdialysate," *Anal Chem,* 1992, 64, 1790-1794.

[30] H. Wesinger, "Metabolic Pathways for Glucose in Astrocytes." *GLIA*, 1997, 21:22-34.

[31] R. Forsyth, "A Role for Astrocytes in Glucose Delivery to Neurons?" *Developmental-neuroscience,* 1996; 18(5-6): 360-70.

[32] Silver, IA. And Erecinska-M., "Extracellular Glucose Concentration in Mammalian Brain: Continuous Monitoring of Changes during Increased Neuronal Activity and upon Limitation in Oxygen Supply in Normo-, Hypo, and Hyperglycemic Animals." Journal of Neurosciences, 1994, 14(8) 5068-76.

[33] Gjedde, A., "High and low-affinity transport of D-glucose from blood to brain," *J.Neurochem.,* 1981, 36, 1463-1471.

[34] Weglinski, Margaret R., and Lanier, William L., "The Effects of Transient Hyperglycemia on Brain Glucose in Rats Anesthetized with Halothane." Anesthesiology, 1990, 73: 291-296.

[35] Cataldo, A., Broadwell, R., "Cytochemical identification of cerebral glycogen and glucose-6-phosphatase activity under normal and experimental conditions: Neurons and glia," *J. Elect. Micro Tech.,* 1986, 3, 413-437.

[36] Cataldo, A., Broadwell, R., "Cytochemical identification of cerebral glycogen and glucose-6-phosphatase activity under normal and experimental conditions: Choriod plexus and ependymal epithelia and pericytes," *J. Neurol.,* 1986, 15, 511-524.

[37] Swanson, R., "Physiologic coupling of glial metabolism to neuronal activity in brain," *J. Physiol. Pharmacol.,* 1992, 70, S138-S144.

[38] Swanson, R., and Choi, D., "Glial glycogen stores affect neuronal survival during glucose deprivation in vitro." *J. Cerebr. Blood Flow Metab.,* 1993, 13, 162-169.

[39] Silver, IA., Erecinska-M. "Glucose-Induced intracellular ion changes in sugar-sensitive hypothalamic neurons." Journal of Neurophysiology 1998 April, 79(4): 1733-45.

[40] Korf, Jakob., et al. "Monitoring of Glucose and Lactate Using Microdialysis: Applications in Neonates and Rat Brain." Developmental-neuroscience. 1993; 15(3-5): 240-6.

[41] Goodman, J. Clay., et al., "Extracellular lactate and glucose alterations in the brain after head injury measured by microdialysis." Critical Care Medicine 1999, vol. 27, No. 9: 1965-1973.

[42] U Ungerstedt, CH Pycock, "Functional correlates of dopamine transmission," *Bull. Schweiz.Akad. Med. Wiss.,* vol. 1278, pp. 1-13, 1974.

[43] Van der Kuil, J., Korf, J., "On-line monitoring of extracellular brain glucose using microdialysis and a NADPH-linked enzymatic assay," *J. Neurochem.,* 1991, 57, 648-654.

[44] Osborne, P., Niwa, O., Kato, T.,Yamamoto, K., "On-line, Real Time Measurement Of Extracellular Brain Glucose Using Microdialysis and Electrochemical Detection." *Current Seperations,* 1996, 15, 19-23.

[45] TP Obrenovitch, E Zilkha, J Urenjak, "Intracerebral microdialysis: electrophysiological evidence of a critical pitfall," *J Neurochem,* vol. 64, pp. 1884-1887, 1995.

[46] Lada, M.; Vickroy, T.; and Kennedy, R., "High Temporal Resolution Monitoring of Glutamate and Aspartate in vivo Using Microdialysis Online with Capillary Electrophoresis with Laser-Induced Fluorescence Detection," *Analytical Chemistry,* 1997, 69, 4560-4565.

[47] Xaing, F.; Lin, Y.; Wen, J.; Matson, D.; Smith, D., "An Integrated Microfabricated Device for Dual Microdialysis and On-lin ESI-Ion Trap Mass Spectrometry for Analysis of Complex Biological Samples," *Analytical Chemistry*, 1999, 71, 1485-1490.

[48] SJ Updike, GP Hicks, "The Enzyme Electrode," *Nature*, 214:986 (1967).

[49] Bott, A., "Electrochemical Methods for the Determination of Glucose," *Current Separations*, 1998, 17:1, 25-31.

[50] Yinon Degani, Adam Heller "Electrical communication between redox centers of glucose oxidase and electrodes via electrostatically and covalently bound redox polymers," *J. Am. Chem. Soc.*; 1989; *111*(6); 2357-2358.

[51] Huo, J., Wang, X., Sha, X., "Amperometric determination of glucose with a ferrocene-mediated glucose oxidase electrode," *Sensors and Actuators, B: Chemical*, v B12, n 1, Mar 15, 1993, p 33-36.

[52] McRipley, M., Linsenmeier, R., "Fabrication of a mediated glucose oxidase recessed microelectrode for the amperometric determination of glucose," *Journal of Electroanalytical Chemistry*, v 414, n 2, Oct 20, 1996, p 235-246.

[53] Tetsu Tatsuma, Kenichi Saito, Noboru Oyama, "Enzyme electrodes mediated by a thermoshrinking redox polymer," *Anal. Chem.*, 1994; *66*(7); 1002-1006.

[54] Chen, T., Binyamin, G., Schmidtke, D., Friedman, K., Heller, A., "In vivo Glucose Monitoring with Miniature "Wired" Glucose Oxidase Electrodes," *Analytical Sciences*, 2001, vol. 17, i297-i300.

[55] Yiting Wang, Jianzhong Zhu, Rongjin Zhu, Ziqiang Zhu, Zongsheng Lai, Zongyou Chen, "Chitosan/Prussian blue-based biosensors," Meas. Sci. Technol. 2003, 14 831-836.

[56] Lübber, D.W., and Opitz, N., "Die PCO_2 -/PO_2- Optode: Eine neue PCO_2 bzw-PO_2 Meβsonde zur Messung des PCO_2 oder PO_2 von Gasen in Flüssigkeiten," *Z. Naturforsch*, 1975, 30c, 532.

[57] Trettnak, W., Leiner, M., Wolfbeis, O., "Part 34 Fibre Optic Glucose Sensor With an Oxygen Optrode as the Transducer," *Analyst*, 1998, 113, 1519-1523.

[58] Trettnak, W., Leiner, M., Wolfbeis, O., "Fibre Optic Glucose Sensor With a pH Optrode as the Transducer," *Biosensors*, 1988, 4, 15-26.

[59] Moreno-Bondi, M. C., Wolfbeis, O., Leiner, M., Schaffar, P.H., "Oxygen Optrode for Use in a Fiber-Optic Glucose Biosensor," *Anal. Chem.*, 1990, 62, 2377-2380.

[60] Neubauer, A., Dietmar, P., Sleytr, U., Klimant, I., Wolfbeis, O., "Fibre-Optic glucose biosensor using enzyme membranes with 2-D crystalline structure," *Biosensors and Bioelectronics*, 1996, 11, 317-325.

[61] Tan, W., Shi, Z., Kopelman, R., " Miniaturized fiber-optic chemical sensors with fluorescent dye0doped polymers," *Sensors and Actuators B*, 1995, 28, 157-163.

[62] Trettnak, W, Wolfbeis, O., "Fully Reversible Fibre-Optic Glucose Biosensor Based on the Intrinisc Fluoresence of Glucose Oxidase," *Analytica Chimica Acta*, 1989, 221, 195-203.

[63] Uwira, N., Opitz, N., and Lübber, D.W., "Influence of Enzyme Concentration and Thickness of the Enzyme Layer on the Calibration Curve of the Continuously Measuring Glucose Optode," *Adav. Exp. Med. Biology*,1984, 169, 913-921.

[64] BPH Schaffar, OS Wolfbeis, "A fast responding fiber optic glucose biosensor based on an oxygen optrode," *Biosensors & Bioelectronics*, vol. 5, pp. 137-148, 1990.

[65] S Mansouri, JS Schultz, "A miniature optical glucose sensor based on affinity binding," *Bio-Technology*, vol. 2, pp. 885-890, 1984.

[66] JS Schultz, S Mansouri, IJ Goldstein, "Affinity sensor: A new technique for developing implantable sensors for glucose and other metabolites," *Diabetes Care*, vol. 5, pp. 245-253, 1982.

[67] D Meadows, JS Schultz, "Fiber-optic biosensors based on fluorescence energy-transfer," *Talanta*, vol. 35, pp. 145-150, 1988.

[68] JR Lakowicz, B Maliwal, "Optical sensing of glucose using phase-modulation fluorimetry," *Analytica Chimica Acta*, vol. 271, pp. 155-164, 1993.

[69] R Ballerstadt, JS Schultz, "Competitive-binding assay method based on fluorescence quenching of ligands held in close proximity by a multivalent receptor," *Analytica Chimica Acta*, vol. 345, pp. 203-212, 1997.

[70] DL Meadows, JS Schultz, "Design, manufacture, and characterization of an optical-fiber glucose affinity sensor based on an homogeneous fluorescence energy-transfer assay system," *Analytica Chimica Acta*, vol. 280, pp. 21-30, 1993.

[71] L Tolosa, H Szmacinski, G Rao, JR Lakowicz, "Lifetime-based sensing of glucose using energy transfer with a long lifetime donor," *Analytical Biochemistry*, vol. 250, pp. 102-108, 1997.

[72] L Li, DR Walt, "Dual-analyte fiberoptic sensor for the simultaneous and continuous measurement of glucose and oxygen," *Analytical Chemistry*, vol. 67, pp. 3746-3752, 1995.

[73] L Tolosa, H Malak, G Raob, JR Lakowicz, "Optical assay for glucose based on the luminescence decay time of the long wavelength dye Cy5TM," *Sensors and Actuators B-Chemical*, vol. 45, pp. 93-99, 1997.

[74] A Sharma, NSM Quantrill, "Measurement of glucose using fluorescence quenching," *Spectrochimica Acta Part A-Molecular and Biomolecular Spectroscopy*, vol. 50, pp. 1179-1193, 1994.

[75] K Kataoka, I Hisamitsu, N Sayama, T Okano, and Y Sakurai, "Novel sensing system for glucose based on the complex formation between phenylborate and fluorescent diol compounds," *Journal of Biochemistry*, vol. 117, pp. 1145-1147, 1995.

[76] Z Rosenzweig, R Kopelman, "Analytical properties and sensor size effects of a micrometersized optical fiber glucose biosensor," *Analytical Chemistry*, vol. 68, pp. 1408-1413, 1996.

[77] Brown, J.Q., McShane, M.J., "Nanoengineered Polyelectrolyte Micro- and Nano-Capsules as Fluorescent Potassium Ion Sensors," *IEEE-EMBS Magazine* vol. 22, pp. 118-123, 2003.

[78] Xu, H., Aylott, J., and Kopelman, R., "Fluorescent nano-PEBBLE sensors designed for intracellular glucose imaging," *The Analyst*, 2002, 127, 1471-1477.

[79] Brasuel M, Kopelman R, Kasman I, Miller TJ, and Philbert MA (2002), "Ion Concentrations in Live Cells from Highly Selective Ion Correlation Fluorescent Nano-Sensors for Sodium," *Proceedings of IEEE 1*, 288-292

[80] Sumner JP, Aylott JW, Monson E, and Kopelman R., "A fluorescent PEBBLE nanosensor for intracellular free zinc," *The Analyst*, 2002, 127, 11-16.

[81] J.S. Schultz, S. Mansorouri, G. G. Goldstein, "Affinity sensor: A new technique for developing implantable sensors for glucose and other metabolites," *Diabetes Care*, 1982, 5(3), 245-253.

[82] S. Mansorouri, J.S. Schultz, "A miniature optical glucose sensor based on affinity binding," *Biotechnology,* 1984, 885-890.

[83] Ballerstadt R. Schultz JS. Kinetics of dissolution of concanavalin A/Dextran sols in response to glucose measured by surface plasmon resonance. Sensors and Actuators, B 46:50-55, 1998

[84] D'Auria, S., Herman, P., Rossi, M., Lakowicz, J., "The Fluorescence Emission of Apo-glucose Oxidase from *Aspergillus niger* as Probe to Estimate Glucose Concentrations," *Biochem. and Biophys. Research Comm.,* 1999, 263, 550-553.

[85] Marcos, S., Galindo, J., Sierra, J., Galban, J., Castillom J., "An optical glucose biosensor based on derived glucose oxidase immobilized onto a sol-gel matrix," *Sensors and Actuators B,* 1999, 227-232.

[86] Tatsu, Y., Yamamura, S., "Fluorescence measurement of glucose by pyrene –modified oxidase," *Journal of Molecular Catalysis B: Enzymatic,* 2002, 203-206.

[87] R Iler, "Multilayers of colloidal particles," *J. Colloid & Interface Sci.* 21: 569 (1966).

[88] Y Lvov, G Decher and H Möhwald, "Assembly, structural characterization and thermal behavior of layer-by-layer deposited ultrathin films of polyvinylsulfonate and polyallylamine," *Langmuir* 9: 481 (1993).

[89] Y Lvov, G Decher and G Sukhorukov, "Assembly of thin films by means of successive deposition of alternate layers of DNA and poly(allylamine)," *Macromolecules* 26: 5396 (1993).

[90] Y Lvov, H Haas, G Decher, H Möhwald and A Mikhailov, "Successive deposition of alternate layers of polyelectrolytes and charged virus," *Langmuir* 10: 4232 (1994).

[91] G Decher, Y Lvov, J Schmitt, "New nanocomposite films for biosensors: layer-by-layer adsorbed film of polyelectrolytes, proteins or DNA," *Biosens & Bioelect* 9: 677 (1994).

[92] M Sano, Y Lvov and T Kunitake, "Formation of ultrathin polymer layers by means of polymerization-induced epitaxy and alternate adsorption," *Ann. Rev. Material Science* 26: 153 (1996).

[93] K Ariga, Y Lvov and T Kunitake, "Assembling alternate dye-polyion molecular films by electrostatic layer-by-layer adsorption," *J. Am. Chem. Soc.* 119: 2224 (1997).

[94] Y Lvov, "Electrostatic layer-by-layer assembly of proteins and polyions," In *Protein Architecture:Interfacial Molecular Assembly and Immobilization Biotechnology*, Ed: Y. Lvov and H. Möhwald, 1999, M. Dekker Publ., NY, p.125-167.

[95] Y Lvov, K Ariga, I Ichinose and T Kunitake, "Assembly of multicomponent protein films by means of electrostatic layer-by-layer adsorption," *J. Am. Chem. Soc.* 117: 6117 (1995).

[96] S Keller, H-N Kim and T Mallouk, "Layer-by-Layer Assembly of Intercalation Compounds and Superlattices on Surfaces: Towards Molecular 'Beaker' epitaxy," *J. Am. Chem. Soc.* 116: 8817 (1994).

[97] N Kotov, I Dekany and J Fendler, "Layer-by-layer self-assembly of polyelectrolyte semiconductor nanoparticle composite," *J. Phys. Chem.* 99: 13065 (1995).

[98] M Onda, Y Lvov, K Ariga and T Kunitake, "Sequential reactions by glucose oxidase/peroxidase molecular films assembled by layer-by-layer alternate adsorption," *J. Ferment.Bioengin.* 82: 502 (1996).

[99] Y. Lvov, Z. Lu, X. Zu, J. Schenkman and J. Rusling, "Direct electrochemistry of myoglobin and cytochrome P450cam in alternate layer-by-layer films with DNA and other polyions," *J. Am. Chem. Soc.* 120: 4073 (1998).

[100] J. Kong, Y. Lvov, H. Frank and J. Rusling, "Direct electrochemistry of cofactor redox sites in Bacterial Photosynthetic Reaction Center protein," *J. Am. Chem. Soc.* 120: 7371 (1998).

[101] F Caruso, C Schuler and D Kurth, "Core-shell particles and hollow shells containing metallosupramolecular components," *Chem. Mater.* 11: 3394 (1999).

[102] Y Lvov, R Price, S Alok, J Selinger and J Schnur, , "Nanoparticle patterning on biologically derived microstructures," *Langmuir* 17: 5932-5936 (2000).

[103] Lvov, Y.; Antipov, A. A.; Mamedov, A.; Mohwald, H.; Sukhorukov, G. B.,"Urease Encapsulation in Nanoorganized Microshells" *Nano Lett.,* (Communication); 2001; *1*(3); 125-128.

[104] McShane, M.J., Brown, J.Q, Guice, K.B., Lvov , Y.M., "Polyelectrolyte Microshells as Carriers for Fluorescent Sensors: Loading and Sensing Properties of a Ruthenium-Based Oxygen Indicator," *Journal of Nanoscience and Nanotechnology* , vol. 2, pp. 411-416, 2002.

[105] S. Moya, G. B. Sukhorukov, M. Auch, E. Donath and H. Möhwald, "Microencapsulation of Organic Solvents in Polyelectrolyte Multilayer Micrometer-Sized Shells," *Journal of Colloid and Interface Science*, 216, 2 297-302.

[106] Lvov, Y.; Antipov, A. A.; Mamedov, A.; Mohwald, H.; Sukhorukov, G. B.; "Urease Encapsulation in Nanoorganized Microshells," *Nano Lett*; 2001; *1*(3); 125-128.

[107] G. B. Sukhorukov, E. Donath, S. Davis, H. Lichtenfield, F. Caruso, V. I. Popov, and H. Mohwald, "Stepwise Polyelectrolyte Assembly on Particle Surfaces: a Novel Approach to Colloid Design." *Poly. Adv. Tech.*, vol. 9, pp. 759-767, 1998.

[108] M.J. McShane, J.Q. Brown, K.B. Guice, Y.M. Lvov. "Polyelectrolyte microshells as carriers for fluorescent sensors: Loading and sensing properties of a Ruthenium-based oxygen sensor," *Journal of Nanoscience and Nanotechnology*, vol. 2, no. 2, pp. 1-6, 2002.

[109] Duchesne, T.A., J.Q. Brown, K.B. Guice, Y.M. Lvov, and M.J. McShane, "Nanoengineered Fluorescent Sensors Based on Encapsulation of Indicators in Polyelectrolyte Capsules," *Sensors and Materials*, vol. 14, pp. 295-308, 2002

[110] C. Schuler and F. Caruso, "Preparation of enzyme multilayers on colloids for biocatatlysis," *Macromol. Rapid Comm.*, 21, 750-753.

[111] Stein, E.W., McShane, M.J., " Multilayer Lactate Oxidase Shells on Colloidal Carriers as Engines for Nanosensors," *IEEE Transactions on Nanobioscience* , vol. 3, pp. 133-137, 2003.

[112] Anzai, J., Kobayahi, Y., Suzuki, Y., Takeshita, H., Chen, Q., Osa, T., Hoshi, T., Du, X., "Enzyme sensors prepared by layer-by-layer deposition of enzymes on platinum electrode through avidin-biotin interaction," *Sensors and Actuators B*, 52, 1998, 3-9.

[113] Sirkar, K.; Revzin, A.; Pishko, M. V.; "Glucose and Lactate Biosensors Based on Redox Polymer/Oxidoreductase Nanocomposite Thin Films," *Anal. Chem.*, 2000; *72*(13); 2930-2936.

[114] Hoshi, T.; Saiki, H.; Kuwazawa, S.; Tsuchiya, C.; Chen, Q.; Anzai, J., "Selective Permeation of Hydrogen Peroxide through Polyelectrolyte Multilayer Films and Its Use for Amperometric Biosensors," *Anal. Chem.*, 2001, *73*(21); 5310-5315.

[115] Yuri Lvov, Katsuhiko Ariga, Izumi Ichinose, Toyoki Kunitake; "Assembly of Multicomponent Protein Films by Means of Electrostatic Layer-by-Layer Adsorption," *J. Am. Chem. Soc.*; 1995; *117*(22); 6117-6123.

[116]M. Onda, K. Ariga, and T. Kunitake, "Activity and stability of glucose oxidase in molecular films assembled alternately with polyions", *Journal of Bioscience and Bioengineering*, 1997,*87, 69-75.*

[117] Grant, P.S., McShane, M.J., "Development of Multilayer Fluorescent Thin Film Chemical Sensors Using Electrostatic Self Assembly," *IEEE Sensors Journal* , vol. 3, pp. 139-146, 2003.

[118] Duchesne, T.A., Brown, J.Q., Guice, K.B., Lvov , Y.M., McShane, M.J., "Encapsulation and Stability Properties of Nanoengineered Polyelectrolyte Capsules for use as Fluorescent Sensors," *Sensors and Materials,* vol. 14, 293-308, 2002.

[119] F.J. Arregui, Y. Liu, I.R. Matias, and R.O. Claus, "Optical Fiber Humidity Sensor Using a Nano Fabry-Perot Cavity Formed by the Ionic Self-Assembly Method," *Sensors and Actuators B, Chemical*, 59 [1] 54-59 (1999).

[120] Chen, Z., Broaddus, W., Viswanathan, R., Raghaven, R. and Gillies G., "Intraparenchymal drug delivery via positive-pressure infusion: experimental and modeling studies of poroelasticity in brain phantom gels," *IEEE Trans., Biomed. Eng.*, 2002, 49, 85-96.

[121] Nicholson, C., "Diffusion and related transport mechanisms in brain tissue," *Rep. Prog. Phys.,* 2001, 64, 815-884.

[122] Gillies, G., Allison, S., Tissue, B., " Positive pressure infusion of fluorescent nanoparticles as a probe of the structure of brain phantom gelatins," *Nanotechnology*, 2002, 13, 484-486.

[123] Tromberg BJ, Coquoz O, Fishkin JB, Butler J, Svaasand LO; "Noninvasive Characterization of Tissue Optical Properties Using Frequency Domain Photon Migration," *Wyss P, Tadir Y, Tromberg BJ, Haller U (eds): Photomedicine in Gynecology and Reproduction.Basel, Karger, 2000, pp 116-132.*

[124] Kriechbaum, M., Heilmann, H., Wientjes, F., Hahn, M., Jany, K., Gassen, H., Sharif, F., Alaeddinoglu, G., "Cloning DNA sequence analysis of the glucose oxidase gene from *Aspergillus niger* NRRL-3," *FEBS Lett*. 1989, 255, 63-66.

[125] Pasur, J., Kleppe, K., "The oxidation of glucose and related compounds by the glucose oxidase from *Aspergillis niger*," *Biochemistry*, 1964, 3, 578-583.

[126] Hecht, H., Kalisz, H., Hendle, J., Schmid , R., Schomburg D., "Crystal structure of glucose oxidase from *Aspergillis niger.* Refined at 2.3 Å resolution," *J. Mol. Biol.*, 1993, 229, 153-172.

[127] Haouz, A., Twist, C., Zentz, C., Tauc, P., Alpert, B., "Dynamic and structural properties of glucose oxidase enzyme," *Eur. Biophys.* 1998, 27, 19-25.

[128] J. R. Lakowicz. *Principles of Fluorescence Spectroscopy, Second Ed.*, Kluwer Academic/Plenum Publishers: New York, 1999.

[129] G. Zauerbrey, Z. Phys., 155 (1959) 206.

[130] Richard P. Haughland. Handbook of Fluorescent Probes and Research Products: Ninth Edition," Molecular Probes, Inc. 2002.

[131] Chopra, Suruchi " Design and Testing of Nanastructured Enzyme based Fluorescent NanoBiosensors." Thesis. Louisiana Tech University, 2004.

[132] N. Sakamoto, " Effect of Enzyme Concentration on the Dynamic Behavior of a Membrane-Bound Enzyme System", *J Membrane Sci*, vol. 70, pp. 237-247, 1992.

[133] Polyakova, A., Liu, R., Schiraldi, D., Hiltner, A., Baer, E., "Oxygen –Barrier Properties of Copolymers Based on Ethylene Terphthalate," *J. Polymer Sci.*, 2001, 39, 1889-1899.

[134] McShane, M.J., Russell, R.J., Pishko, M.V., and Coté, G.L., "Towards Minimally-Invasive Glucose Monitoring Using Implanted Fluorescent Microspheres," *IEEE-EMBS Magazine* , 19, pp. 36-45, 2000.

[135] Guice and McShane. Loading and Oxygen Quenching Behavior of Ruthenium-tris(4,7-diphenyl-1,10-phenanthroline) dichloride in Multilayer Polyelectrolyte Films on Fluorescent Nanoscale Carriers. Submitted

[136] M. Linford, M. Auch, H. Möhwald, "Nonmonotonic Effect of Ionic Strength on Surface Dye Extraction during Dye-Polyelectrolyte Multilayer Formation," *J. Am. Chem. Soc.*, 1998, *120, 178-182.*

[137] C. Tedeschi, F.Caruso, H. Möhwald, and A. Kirstein, "Adsorption and Desorption Behavior of an Anionic Pyrene Chromophore in Sequentially Deposited Polyelectrolyte-Dye Thin Films," *J. Am. Chem. Soc.,* 2000, 122, 5841-5848.

[138] K. Ariga, M. Onda, Y. Lvov, and T. Kunitake, "Alternate Layer-by-Layer Assembly of Organic Dyes and Proteins is Facilitated by Premixing with Linear Polyions," *Chem. Lett.,* 1997, 25-26.

[139] D. Chang-Yen, Y. Lvov, M. McShane, B. Gale, "Electrostatic Self-Assembly of a Ruthenium-Based Oxygen Sensitive Dye Using Polyion-Dye Interpolyelectrolyte Formation," *Sens. & Act B.* 2002, 87, 336-345.

[140] Shiratori, S. S.; Rubner, M. F.; "pH-Dependent Thickness Behavior of Sequentially Adsorbed Layers of Weak Polyelectrolytes," *Macromolecules*; 2000; *33*(11); 4213-4219.

[141] Mendelsohn, J. D.; Barrett, C. J.; Chan, V. V.; Pal, A. J.; Mayes, A. M.; Rubner, M. F.; "Fabrication of Microporous Thin Films from Polyelectrolyte Multilayers," *Langmuir*; 2000; *16*(11); 5017-5023.

[142] Dubas, S. T.; Schlenoff, J. B.; "Swelling and Smoothing of Polyelectrolyte Multilayers by Salt,"*Langmuir;* 2001; *17*(25); 7725-7727

[143] Fery, A.; Scholer, B.; Cassagneau, T.; Caruso, F.; "Nanoporous Thin Films Formed by Salt-Induced Structural Changes in Multilayers of Poly(acrylic acid) and Poly(allylamine)," *Langmuir;* 2001; *17*(13); 3779-3783